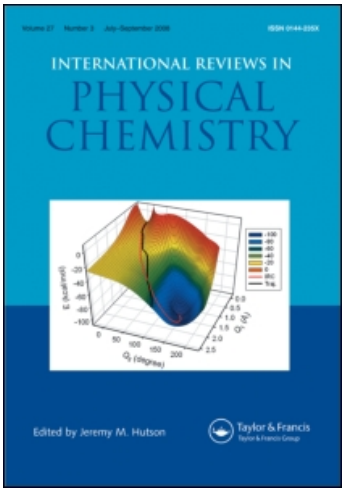

International Reviews in Physical Chemistry
Publication details, including instructions for authors and subscription information:
http://www.informaworld.com/smpp/title~content=t713724383

Spectroscopic and theoretical studies of CH^+_3-Rg_n clusters (Rg=He, Ne, Ar): From weak intermolecular forces to chemical reaction mechanisms

Otto Dopfer[a]
[a] Institute of Physical Chemistry, University of Würzburg, Würzburg, Germany

Online publication date: 26 November 2010

To cite this Article Dopfer, Otto(2003) 'Spectroscopic and theoretical studies of CH^+_3-Rg_n clusters (Rg=He, Ne, Ar): From weak intermolecular forces to chemical reaction mechanisms', International Reviews in Physical Chemistry, 22: 3, 437 — 495
To link to this Article: DOI: 10.1080/0144235031000112878
URL: http://dx.doi.org/10.1080/0144235031000112878

INT. REVIEWS IN PHYSICAL CHEMISTRY, 2003
VOL. 22, NO. 3, 437–495

Taylor & Francis
Taylor & Francis Group

Spectroscopic and theoretical studies of CH_3^+–Rg_n clusters (Rg = He, Ne, Ar): from weak intermolecular forces to chemical reaction mechanisms

OTTO DOPFER†
Institute of Physical Chemistry, University of Würzburg, Am Hubland, D-97074 Würzburg, Germany

This review summarizes the recent combined experimental and theoretical effort of high-resolution spectroscopy, mass spectrometry and quantum chemical calculations to characterize isolated CH_3^+–Rg_n clusters (Rg = He, Ne, Ar; $n \leq 8$). These complexes serve as a model system for the solvation of a fundamental reactive carbocation by non-polar ligands. The results provide unprecedented and detailed information about important properties of the interaction potential as a function of the interaction strength and the degree of microsolvation of the methyl cation. These include the geometries and binding energies of minima and transition states, the structure of solvation (sub)shells, the competition between various types of intermolecular bonding (p bonds versus H bonds), the change in the origin of the interaction as a function of the size of the Rg atom and the degree of solvation (induction versus charge transfer), the importance of monomer relaxation, the large angular–radial coupling and zero-point effects of the potential of these prototype disk-and-ball dimers, and the significance of non-cooperative three-body effects. The studies of CH_3^+–Rg and related dimers demonstrate that the inert Rg ligands can be used as a sensitive probe of the chemical reactivity of specific orbitals in molecular ions. In addition, the Rg–CH_3^+–Rg trimers represent simple prototype intermediates in degenerate cationic nucleophilic substitution (S_N2) reactions, and the results for Ar–CH_3^+–Ar provide the first spectroscopic evidence that such reactions proceed via a double minimum potential in the gas phase. The CH_3^+–Rg_n results show that the fruitful combination of modern state-of-the-art spectroscopic and theoretical approaches provides a powerful route to the understanding of the physical and chemical properties of ion–solvent interactions at the molecular level.

Contents

† E-mail: dopfer@phys-chemie.uni-wuerzburg.de

International Reviews in Physical Chemistry ISSN 0144–235X print/ISSN 1366–591X online © 2003 Taylor & Francis Ltd
http://www.tandf.co.uk/journals
DOI: 10.1080/0144235031000112878

1. Introduction

1.1. *Ion–ligand complexes*

Over the past two decades, high-resolution spectroscopy of ionic complexes of the type $A^{\pm q}$–L_n has grown into a very active field with relevance to important phenomena in physical, chemical and biological disciplines [1]. Ionic complexes are ideal model systems to investigate the interaction between an ion ($A^{\pm q}$) and a well-defined number (n) of solvent molecules (L) from the microscopic point of view. In general, ion–neutral interactions bridge the gap between weak van der Waals and hydrogen bonds (H bonds) in neutral aggregates and strong chemical bonds present in stable molecules. The interaction in charged clusters is usually significantly stronger than that of their neutral counterparts, because of additional electrostatic and inductive forces, charge transfer and covalent contributions to the interaction [1].

The motivations for investigating ion–neutral interactions are manifold. First, by systematically characterizing the properties of $A^{\pm q}$–L_n clusters as a function of cluster size, the microsolvation process of an ion by neutral solvent molecules can be monitored in a stepwise fashion, and microscopic molecular properties ($n = 0$) can be related to macroscopic attributes of the bulk limit ($n \rightarrow \infty$). Important ion solvation processes occur, for example, in biological systems [2–4], electrolytic media (salt solutions, oceans) [5–7] or industrial processes [8]. Furthermore, ionic complexes are frequently intermediates of fundamental ion–molecule reaction mechanisms, such as proton transfer or electrophilic and nucleophilic substitution reactions [1, 9–12]. Hence, their characterization improves our understanding of these reaction mechanisms and their dependence on solvation [12, 13]. Moreover, ion–molecule reactions dominate the chemistry of low-density media (e.g. low-temperature plasmas, ionosphere, interstellar media), because of the large strength and long range of the interaction. For example, charged complexes dominate the ion chemistry in the upper terrestrial atmosphere [14]. Ion–neutral interactions are also essential for a variety of important biophysical phenomena (e.g. molecular recognition and enzymatic processes) [2–4].

The detailed understanding of ion–solvent interactions from the microscopic point of view requires accurate knowledge of the intermolecular potential energy surface (PES). It is well established that mass spectrometric and high-resolution spectroscopic techniques on the experimental side, combined with high-level quantum chemical calculations on the theoretical side, provide the most direct access to the details of the PES [1]. Excellent and comprehensive reviews both describing the spectroscopy of charged complexes and discussing the formation, energetics and reactivity of ionic complexes are given in a recent overview [1]. The spectroscopic characterization of ion complexes has often been preceded by mass spectrometric studies. Of particular importance has been the application of high-pressure mass spectrometry, collision-induced dissociation, the analysis of metastable decay fractions and fragment kinetic energy releases, and the observation of magic numbers in mass spectra to determine association enthalpies and entropies and the structure of solvation (sub)shells [13, 15–20]. However, although these mass spectrometric studies have often provided information on energetic properties of ion complexes, details of their structure and other relevant attributes remained obscure. On the other hand, spectroscopic techniques, in particular in the microwave (MW) and infrared (IR) spectral ranges, are a very sensitive probe of the structure and dynamics of neutral and charged clusters [21]. In comparison with neutral clusters, however, ion–ligand complexes are spectroscopically far less well characterized, because of the difficulties encountered in the production of high number densities [1]. Recent developments of highly sensitive spectroscopic approaches were able to overcome this obstacle [1]. The present review summarizes results obtained by IR photodissociation (IRPD) spectroscopy, a technique described in some detail in section 2.1.

Small ionic complexes are also very interesting from the theoretical viewpoint because, although dispersion is similar to neutral complexes, the dominant binding forces arise from electrostatic, induction and charge transfer interactions [1]. The intermolecular PESs in ionic complexes are thus often more anisotropic than those of their neutral counterparts and internal motions, which are valuable sources of information about the PES of neutral clusters, are more effectively quenched in ionic complexes. Moreover, as spectroscopic measurements of ionic complexes are

frequently performed in molecular beams, where only the lowest rovibrational levels have significant population, these experiments probe only limited regions of the PES. Therefore, complementary quantum chemical studies are required to probe the hidden parts of the PES in ionic complexes. An additional reason for performing quantum chemical studies for weakly bound complexes with shallow potential minima arises from the fact that the transformation of the limited available spectroscopic information into parameters of the PES is not unambiguous. For strongly bound semirigid molecules standard approaches, such as the anharmonic oscillator and semirigid rotor models, have successfully been applied to extract PES parameters from spectroscopic data. On the other hand, for flexible non-rigid complexes, the vibrational wavefunctions are often largely delocalized even in the ground vibrational state and, as a result of the large-amplitude motions, the interpretation of the spectral data can depend significantly on the Hamiltonian employed for the analysis [22, 23]. Furthermore, fitting a limited amount of spectral data to empirical analytic potential functions yields only effective potential parameters. Although these may reproduce the limited experimental data set well, they may not properly represent the true interaction potential [23]. In such cases, high-level *ab initio* calculations are required to construct physically realistic potentials providing at least a semiquantitative impression of the true PES [22, 23]. Another interesting aspect of the interaction in larger charged complexes is the often significant contribution of three-body potential terms, mainly arising from non-additive induction forces [1, 24].

1.2. *Properties of CH_3^+*

Similarly to the methyl radical, the methyl cation (methylium) belongs to the group of the most important reactive intermediates in organic chemistry [25–33]. CH_3^+ is a fundamental carbocation and occurs as a fragment ion in the mass spectra of many hydrocarbon molecules [34, 35]. The importance of short-lived carbocations in solution chemistry is indicated by the Nobel Prize in Chemistry awarded to George Olah in 1994 for his outstanding contributions to carbocation chemistry [36]. Similarly to other carbocations, CH_3^+ is an extremely electrophilic agent, which explains its chemical and biological activity [32, 37]. As a consequence, CH_3^+ and its derivatives play a central role in many processes in hydrocarbon chemistry, for example as intermediates in acid-catalysed electrophilic reactions [25–29]. In addition, CH_3^+ is discussed as a central species in the models describing the ion–molecule reaction chemistry of combustion processes [38, 39], planetary atmospheres [40–43] and interstellar media [44–51]. Both CH_3^+ and CH_3 are ubiquitous components in hydrocarbon plasmas and discharges [34, 52, 53].

The present work describes the spectroscopic characterization of complexes between CH_3^+ and surrounding rare gas (Rg) atoms. As the CH_3^+ ion serves as the IR chromophore in CH_3^+–Rg_n, the interpretation of their spectra is largely supported by comparison with the known properties of the monomer ion. Hence, the available structural and vibrational properties of CH_3^+ will be briefly reviewed. CH_3^+ is a planar closed-shell ion with D_{3h} symmetry in its $^1A_1'$ ground electronic state (figure 1(*a*)). This electronic state is described by the orbital configuration $(1a_1')^2(2a_1')^2(1e')^4$. The lowest unoccupied molecular orbital has a_2'' symmetry and corresponds closely to the atomic out-of-plane $2p_z$ orbital of C (figure 2). The four vibrational modes of CH_3^+ are the symmetric and doubly degenerate asymmetric C–H stretch (figure 2), $\nu_1(a_1')$ and $\nu_3(e')$, the doubly degenerate asymmetric

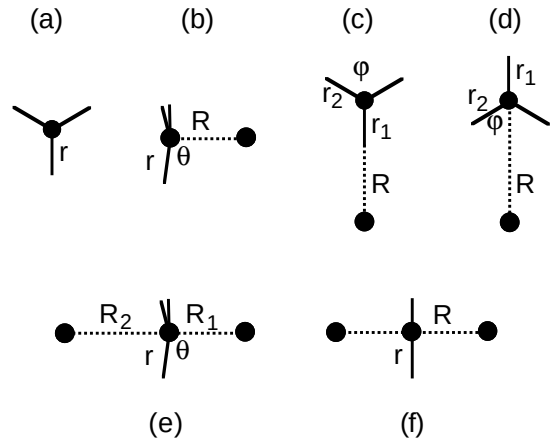

Figure 1. Structures of CH_3^+–Rg_n ($n = 0$–2) calculated at the MP2/aug-cc-pVTZ# level [54–56]: (*a*) CH_3^+ (D_{3h}); (*b*) p-bound CH_3^+–Rg (C_{3v}, global minimum); (*c*) H-bound CH_3^+–Rg (C_{2v}, local minimum); (*d*) side-bound CH_3^+–Rg (C_{2v}, transition state); (*e*) p-bound CH_3^+–Rg_2 (C_{3v}, global minimum for Rg = Ar); (*f*) p-bound CH_3^+–Rg_2 (D_{3h}, global minimum for Rg = He and Ne). Geometrical and energetic parameters are listed in tables 3 and 4.

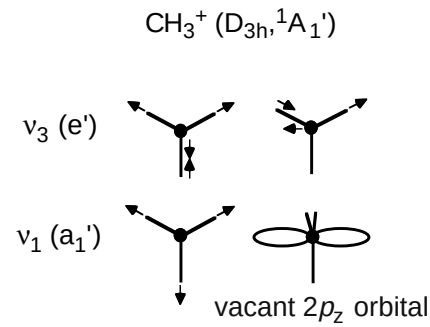

Figure 2. C–H stretch normal modes of CH_3^+: doubly degenerate asymmetric C–H stretch, $\nu_3(e')$, and symmetric C–H stretch, $\nu_1(a_1')$. The vacant $2p_z$ orbital of C perpendicular to the molecular plane is very electrophilic.

C–H bend, $\nu_4(e')$ and the out-of-plane umbrella inversion, $\nu_2(a_2'')$. Experimental information about the structure, rotational constants and vibrational frequencies in the electronic ground state of CH_3^+ (and several isotopomers) in the gas phase is available from photoelectron spectra of CH_3 [57–60], IR absorption spectra of CH_3^+ [52, 61–64] and recent ultraviolet (UV) photodissociation ion-pair imaging of CH_3Cl [65, 66]. On the theoretical side, multidimensional rovibrational calculations on sophisticated *ab initio* potentials provide detailed information about the structure and rotation–vibration parameters [67–73]. The experimental and theoretical CH_3^+ frequencies relevant for the present work are collected in table 1 and compared with those of the corresponding CH_3 radical. The $^2A_2''$ ground state of planar CH_3 (also of D_{3h} symmetry) is obtained from CH_3^+ by adding an electron to the $2p_z$ orbital of C. One effect of this unpaired electron is to strengthen and shorten the C–H bonds ($r_e = 1.076$ versus 1.087 Å for CH_3 versus CH_3^+ [52, 80]), leading to higher C–H stretching frequencies (table 1). On the other hand, the inversion potential for the

Table 1. Experimental and theoretical vibrational frequencies (cm^{-1}) of CH_3 and CH_3^+ compared with corresponding data of CH_3^+–Ar_n ($n=1,2$). Theoretical frequencies are derived from variational calculations (var) or a local mode-coupled Morse oscillators model (LM).

Vibration	CH_3 (experiment)[a]	CH_3^+ (experiment)[b]	CH_3^+–Ar (experiment)[c]	CH_3^+–Ar_2 (experiment)[c]	CH_3^+ (var)[d]	CH_3^+–Ar (LM)[c]	CH_3^+–Ar_2 (LM)[c]	CH_3 (LM)[e]
ν_1	3004.436(12)			2981(3)	2942.3	2979	2986	3005
ν_2	606.4531(6)	1359(7)			1377.8			
ν_3	3160.82118(6)	3108.3770(57)	3145(30)	3151.6(5)	3108.3	3132	3148	3171
ν_4	1396(1)[f]	1370(7)			1387.0			
$2\nu_1$	5959.7(2.1)		5911.936(11)		5874.2	5915	5932	5964
$\nu_1+\nu_3$			6027.70(17)[g]	6054(1)	5991.5	6020	6048	6078
$2\nu_3$ ($\ell=0$)			6191.058(11)	6224(4)	6145.5	6204	6238	6277
$2\nu_3$ ($\ell=2$)			6242.566(15)[g]	6284(2)	6195.5	6241	6274	6318

[a] References [74–78].
[b] References [52, 65].
[c] Reference [54].
[d] Variational calculations on a PES calculated at the extrapolated full coupled cluster level at the basis set limit [73].
[e] Reference [79].
[f] Measured in an Ne matrix.
[g] Neglecting effects of Coriolis coupling.

umbrella motion is much softer for CH_3, as can be seen from the significantly lower ν_2 wavenumber (606 versus 1359 cm^{-1}). Apparently, adding electron density to the $2p_z$ orbital of CH_3^+ reduces drastically the force constant for the inversion motion.

1.3. *Properties of CH_3^+–L_n complexes*

Previous mass spectrometric and theoretical studies have shown that reactions of CH_3^+ with neutral molecules L may proceed via reactive intermediates, in which the ionic reactant and the neutral substrate are stabilized in a CH_3^+–L Lewis acid–base pair [16, 51, 81–105]. These studies demonstrate that CH_3^+ acts as an efficient Lewis acid (electron acceptor) even with respect to inert Rg atoms (e.g. Ar, Kr, Xe) [96–105]. The interaction between the electron donor (L) and CH_3^+ is optimal when the electrophilic $2p_z$ oribital of C is directed toward the ligand L (figure 1(*b*), p bond), as the electron transfer from L to CH_3^+ is maximal at this orientation. (Here, the expression p bonding describes cluster structures in which L is attached to a p orbital of the molecular ion [1].) Similarly to H^+ [106], CH_3^+ forms rather strong covalent bonds to simple stable diatomic and polyatomic closed-shell molecules L (e.g. L = H_2, N_2, CO, O_2, HF, CO_2, H_2O, NH_3, CH_4, HCN, CH_3OH, C_6H_6) [16, 51, 81–103]. Although the Rg atoms Kr and Xe have also high methyl cation affinities [96–105], the interaction of the smaller Rg atoms with CH_3^+ appears to be weaker than expected from their corresponding proton affinities because of less efficient charge transfer [102, 104, 105].

Previous thermochemical and theoretical studies of CH_3^+–L_2 trimers suggest that the $2p_z$ orbital of CH_3^+ may accept electron density from ligands located on both sides of the CH_3^+ ion [91, 102, 104, 105]. In the case of identical ligands, the L–CH_3^+–L structure may be either symmetric or asymmetric (figure 1(*e*, *f*)), depending on the strength of the CH_3^+–L dimer interaction. The asymmetric structure, with two non-equivalent ligands L, corresponds to the stabilized intermediate of the gas-phase cationic degenerate nucleophilic substitution (S_N2) reaction [81, 101]:

$$L + CH_3^+ - L \leftrightarrow [L - CH_3 - L]^+ \leftrightarrow L - CH_3^+ + L. \quad (1)$$

On the other hand, the symmetric structure is the transition state of the reaction. This prototype reaction is a standard textbook example for fundamental organic reaction mechanisms [9, 10]. Because of the usually strong ion–solvent interactions, the energetics and kinetics of ion–molecule reactions, such as the cationic (and also anionic) S_N2 reaction, strongly depend on the type of solvent and the degree of solvation [9, 10, 81, 101, 107–117].

1.4. *Scope of this review*

This review focuses mainly on the recent results of a combined experimental and theoretical effort using high-resolution IR spectroscopy [54–56], mass spectrometry [54–56, 102] and high-level quantum chemical calculations [54–56, 118–120] to characterize both the physical and the chemical properties of isolated CH_3^+–Rg_n clusters (Rg = He, Ne, Ar; $n \leq 8$). These complexes are simple model systems for investigating the stepwise solvation of a fundamental reactive carbocation by non-polar, spherical and structureless ligands. The primary goal of these studies is the detailed characterization of the interaction potential as a function of both the interaction strength and the degree of solvation, leading to an improved understanding of the physical and chemical properties of these elementary complexes at the molecular level.

Important properties of the relevant PESs include the structures and binding energies of minima and transition states, along with their force constants and frequencies for inter- and intramolecular vibrations. For example, CH_3^+ offers several competing binding sites for neutral ligands, including the p-bound global and H-bound local minima (figure 1). Moreover, the dominant contribution to the intermolecular CH_3^+–Rg attraction (dispersion, induction, charge transfer) depends largely on the size of the Rg atom, the region of the PES and the degree of solvation. Analysis of the IRPD process offers information on the predissociation dynamics and the coupling strength between intra- and intermolecular degrees of freedom. The CH_3^+–Rg dimers are prototypes for so called disk-and-ball complexes, with a potential that features deep p-bound global minima and strong coupling between the angular and radial coordinates in the vicinity of the equilibrium structure. In particular for the weakly bound dimers involving the smaller Rg atoms He and Ne, the large-amplitude zero-point motions are sensitively affected by the substantial angular–radial coupling of the disk-and-ball PES [55, 56]. As a result, multi-dimensional calculations on a high-level *ab initio* PES are required for a correct, physically meaningful and semiquantitative interpretation of the measured spectroscopic constants [118]. These three-dimensional (3D) rovibrational calculations represent the first attempt at such calculations for a p-bound $XH_3^{(+)}$–Rg disk-and-ball dimer including all intermolecular degrees of freedom [118]. The significant charge transfer in the more strongly bound CH_3^+–Rg dimers involving Ar or larger Rg atoms induces a substantial structural deformation of the CH_3^+ ion on complexation [119]. Hence, the concept of rigid monomers (that is, neglecting the relaxation of the monomer coordinates on complex formation), frequently applied in the calculation of interaction potentials in neutral complexes, does not provide a realistic approximation to the true ion–ligand PES. Instead, the relaxation of all internal coordinates is required for a physically correct description of the PES of these cation dimers [119]. The data for larger CH_3^+–Rg_n clusters ($n \geq 2$) provide detailed insight into the microsolvation process, such as the structure of solvation (sub)shells and the significance of non-cooperative three-body effects [54, 56, 102, 120].

In addition to physical aspects of the ion–ligand PES, the CH_3^+–Rg_n data provide also valuable information on the chemical properties of both the isolated and the solvated CH_3^+ ion. For example, comparison between available spectroscopic and theoretical results for the XH_3^+–Ar dimers with X = C [54], N [121, 122], and O [121, 123] allows one to monitor the electrophilic character of the $2p_z$ orbital of the central X atom (which is occupied by zero, one or two electrons respectively) as a function of its electron density. This concept uses the inert Rg ligand as a direct and sensitive probe of the chemical reactivity of this particular molecular orbital in these fundamental polyatomic ions. In addition, the Rg–CH_3^+–Rg trimers represent simple prototype intermediates in cationic degenerate S_N2 reactions (1) [81, 101]. The Rg–CH_3^+–Rg data (Rg = He, Ne, Ar) provide detailed information on how the properties of the PES of this fundamental reaction type depend on the strength of the CH_3^+–Rg interaction [54–56]. Significantly, the results for Ar–CH_3^+–Ar [54] represent the first spectroscopic evidence that these reactions are described in all relevant cases by the double minimum potential predicted theoretically [9, 10, 108–114, 116, 117]. Many properties of the CH_3^+–Ar_n clusters in the size range investigated ($n = 1$–8) are intermediate between those of CH_3^+ and CH_3 [54], because of the substantial transfer of electron density from the first Ar solvation shell to the central CH_3^+ core.

The CH_3^+–Ar_n data establish how the reactivity of CH_3^+ is reduced on stepwise solvation with an inert solvent.

Although previous mass spectrometric studies of CH_3^+–Ar_n ($n \leq 8$) [96, 102, 103] and CH_3^+–Kr/Xe [96–101, 103] offer some limited information about the interaction strength in these clusters, detailed experimental information on the structure and dynamics of CH_3^+–Rg_n complexes was completely lacking prior to the recent IR spectroscopic studies [54–56]. Hence, another aim of this review is to illustrate that it is the fruitful combination of modern state-of-the-art spectroscopic and theoretical approaches which provides a powerful route to the detailed understanding of the physical and chemical properties of ion–solvent interactions [1]. Significantly, the IR spectra of CH_3^+–Rg_n ($n \leq 3$) are fully or at least partly rotationally resolved and the derived spectroscopic rotational constants offer invaluable structural and dynamical information [54–56]. The spectra are obtained by IRPD spectroscopy (section 2.1), and the high sensitivity of this technique is perhaps appreciated by recognizing that the CH_3^+–Ar spectra represent the first rotationally resolved overtone spectra of an ionic complex [54], and the CH_3^+–Ar_2 [54] and CH_3^+–Ne_2 [56] spectra correspond to the first fully rotationally resolved spectra recorded for charged trimers. The CH_3^+–Rg_n results discussed in the present work complement similar studies of related AH_k^+–L_n complexes ($L = Rg$, H_2, O_2, N_2, CO_2; $k \leq 4$; $n \leq 14$) investigated with the same spectroscopic and theoretical approaches, including $AH_k^+ = HCO^+$ [22, 124–128], HN_2^+ [128–131], $SiOH^+$ [128, 132, 133], ClH_2^+ [134], CO_2H^+ [135], O_2H^+ [136], OH^+ [137, 138], H_2O^+ [139–142], H_3O^+ [121, 123], NH_2^+ [143–145], NH_3^+ [121, 122], NH_4^+ [23, 146–150], CH_3CNH^+ [151] and $C_3H_3^+$ [152–154]. This extensive data set allows one to establish systematic trends observed for the solvation of a variety of small elementary closed-shell and open-shell cations by inert non-polar ligands.

2. Experimental and theoretical techniques

2.1. *Experimental approach*

In general, the spectroscopic characterization of ion–ligand complexes in the gas phase is a challenging task, because the inherently low concentrations of charged clusters produced in available ion sources often prevent the application of conventional spectroscopic techniques [1]. Hence, most modern spectroscopic methods utilize mass spectrometric techniques in order to improve both sensitivity and selectivity. In recent years, resonance-enhanced photodissociation (PD) spectroscopy of mass-selected complexes in the MW, IR, and UV–visible parts of the electromagnetic spectrum has developed into the probably most powerful tool for the spectroscopic investigation of weakly bound charged aggregates (table 2) [1, 155–167].

Figure 3 details the principle of the IR variant of PD spectroscopy with application to a weakly bound AH^+–L dimer using a tandem mass spectrometer. Cold AH^+–L complexes are produced in a cluster ion source, which combines low-temperature plasma techniques for ionization (induced by a discharge, electron impact or a laser pulse) with the well-described advantages of a molecular beam expansion [168]. The low effective temperatures achieved in such a supersonic plasma expansion enable the efficient production of weakly bound isolated ionic aggregates under controlled condensation conditions and reduce spectral congestion. The generated AH^+–L dimers are selected by a first mass filter and vibrationally excited by a tunable IR laser pulse, for example from the ground vibrational state ($v = 0$) to

Table 2. Number of ionic complexes for which spectra at the level of rotational (or higher) resolution have been obtained between 1987 and 1999, along with the type of spectroscopy and the ion source [1].

Ionic complexes		Spectroscopy		Ion source	
Cation	45	Photodissociation	31 (IR)	Molecular beam	31 electron impact
Anion	6		8 (UV–visible)		8 discharge
		Direct absorption	7 (IR)		12 laser
			2 (MW)	Discharge cell	4
		Rydberg	3 (UV–visible)		
		Zero electron kinetic energy	2 (UV–visible)		

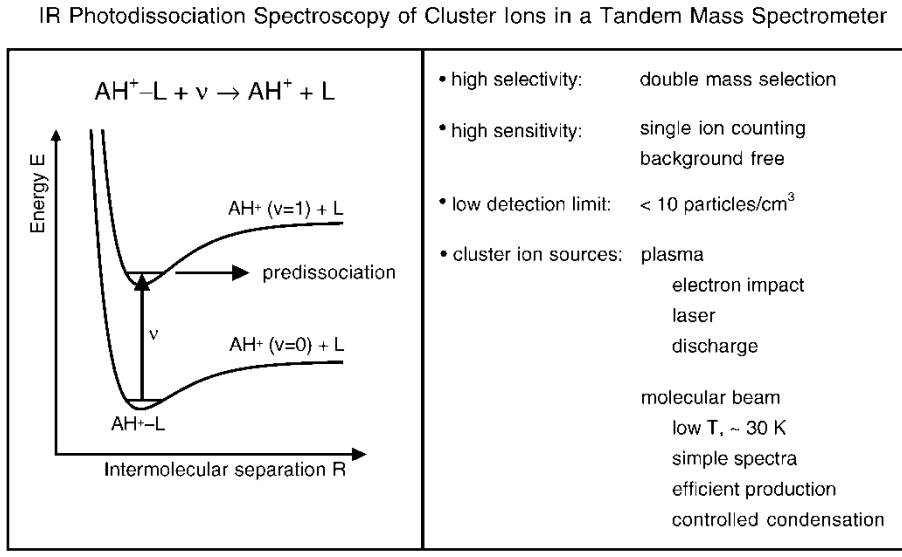

Figure 3. Principle of IRPD spectroscopy of cluster ions in a tandem mass spectrometer illustrated for A–H stretch excitation of AH^+–L dimers. AH^+–L complexes are generated in a cluster ion source and mass selected by an initial mass spectrometer. Absorption of an IR photon (ν) leads to resonant vibrational excitation of the intramolecular A–H stretch fundamental ($v=1$) from the ground vibrational state ($v=0$). As the $v=1$ level of AH^+–L lies above the lowest dissociation limit, predissociation cleaves the intermolecular bond. The produced AH^+ fragment ions are mass selected by a second mass spectrometer and monitored as a function of ν to obtain the IR action spectrum of AH^+–L.

the high-frequency intramolecular A–H stretch fundamental ($v=1$) of the AH^+ moiety. The deposited vibrational energy is transferred into the intermolecular degrees of freedom, leading eventually to the cleavage of the weak intermolecular bond. While for larger aggregates this vibrational predissociation (VP) process may be preceded by intracomplex vibrational energy redistribution (IVR), direct VP is likely to be the dominant relaxation mechanism for smaller clusters [1, 169–171]. The AH^+ fragment ions created by resonant IR absorption are selected by a second mass filter and monitored as a function of the photon frequency (ν) to obtain the IRPD spectrum of AH^+–L. Hence, the absorption of AH^+–L is signalled by the

appearance of AH^+. This type of action spectroscopy combines the high selectivity of mass spectrometry (mass selection of both parent and daughter ions) with the high sensitivity of (nearly) background-free ion detection, which can routinely be performed with nearly 100% efficiency at the single-particle level. Thus, this approach reaches detection limits of < 10 ions cm^{-3} [1], which are several orders of magnitude lower than those required for the most sensitive direct absorption techniques available to date (e.g. cavity ring-down spectroscopy [172]). The success and popularity of IRPD spectroscopy (first applied in 1985 by Lee and co-workers [173]), combined with an electron impact supersonic plasma ion source, is illustrated in table 2, which summarizes all techniques used for recording spectra of ionic complexes at the level of rotational (or higher) resolution between 1987 and 1999 [1]. Figure 4 employs the same statistics [1] to illustrate that high-resolution spectroscopy of charged complexes has been an active and rapidly growing field ever since the first such spectrum was reported in 1987 for H_3^+–Ar [174].

Figure 5 reproduces our realization of the IRPD experiment using a tandem mass spectrometer coupled to an ion source and an octopole ion trap. Details of the cluster ion source are illustrated in figure 6 [175]. A suitable gas mixture is expanded from high pressure (typically 1–30 bar) into a vacuum chamber ($p \sim 10^{-6}$–10^{-4} mbar under operating conditions) through a water-cooled pulsed valve operating at 40 Hz. Chemical ionization of the expanding gas mixture close to the nozzle orifice (diameter ~ 1 mm) is accomplished by two electron beams ($E \sim 50$–200 eV) emitted from twin filaments. Electron impact and/or Penning ionization followed by ion–molecule and subsequent three-body association reactions in the high-pressure region of the expansion produce weakly bound cluster ions with low internal temperatures. Analysis of the rotational line intensities confirms that the rotational temperature is typically of the order of $T_{rot} \sim 10$–50 K [54–56, 140]. Ions are extracted by a soft drift potential ($\Delta U \leq 10$ V) through a skimmer (diameter ~ 1–2 mm) into the first quadrupole mass spectrometer (QMS I), which is tuned to the mass of the parent cluster ion (e.g. AH^+–L). The mass-selected beam is then deflected by 90° and injected into a home-built octopole ion trap. In the octopole, the ion beam is overlapped in space and time with a tunable IR laser pulse. The length of the octopole (~ 0.5 m) is chosen to be similar to that of the ion beam in order to facilitate nearly complete overlap between the ion and laser beams. Moreover, the flight time of the ions through the octopole (up to 1 ms) is substantially longer than typical VP lifetimes of ion clusters [1, 176], so that quantitative dissociation can be observed. The fragment ions (e.g. AH^+) generated

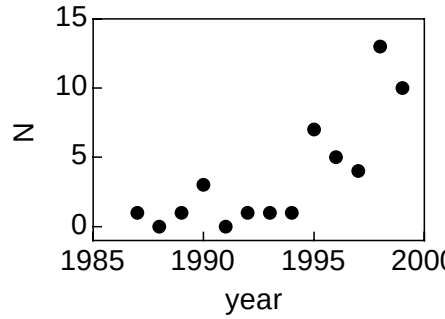

Figure 4. Number of cluster ions (N) for which spectra at the level of rotational (or higher) resolution have been recorded between 1987 and 1999 [1].

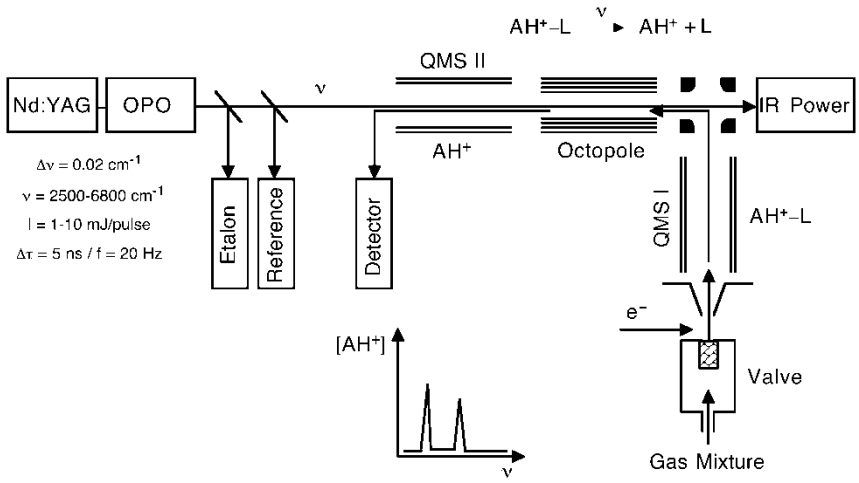

Figure 5. Experimental set-up for the realization of IRPD spectroscopy of cluster cations in a tandem mass spectrometer illustrated for AH^+–L dimers (see also figure 3). AH^+–L complexes are produced in a cluster ion source (figure 6), which combines electron impact ionization with a pulsed and skimmed supersonic expansion. The AH^+–L dimers are selected by the first quadrupole mass spectrometer (QMS I), deflected by 90° with a quadrupole bender and injected in an octopole ion guide where the IRPD process occurs. Generated AH^+ fragment ions are filtered by the second quadrupole mass spectrometer (QMS II) and monitored by a Daly ion detector as a function of ν to obtain the IR action spectrum of AH^+–L. IR radiation with the listed specifications (bandwidth $\Delta\nu$, tuning range ν, pulse energy I, pulse duration $\Delta\tau$ and repetition frequency f) is created by an optical parametric oscillator (OPO) laser system pumped by a Nd:YAG (YAG, yttrium aluminium garnet) laser. Calibration of the IR frequency is accomplished by monitoring etalon fringes of the OPO oscillator and optoacoustic reference spectra using the signal and idler outputs of the OPO. The IR laser intensity measured with an InSb detector is used for normalizing the AH^+ current for laser intensity variations.

in the octopole trap (in most cases only used as an ion guide) are selected with a second quadrupole mass spectrometer (QMS II) and detected by a Daly scintillation detector [177] using boxcar integration. Adjustable potentials at the electrostatic einzel lenses connecting the ion source, QMS I, octopole, QMS II and the ion detector allow one to optimize the ion currents. To separate the contribution of fragment ions generated by laser-induced dissociation (LID) from those produced by metastable decay (MD) or collision-induced dissociation (CID) with residual gas in the octopole region, the ion source is triggered at twice the laser frequency (20 Hz) and the signals from alternating triggers are subtracted. In general, the pressure in the regions of the quadrupoles, the octopole and the ion detector is kept below 10^{-7} mbar to minimize the background signal arising from CID processes. Pulsed and tunable IR laser radiation is created by a single-mode OPO laser system (Continuum Mirage 3000), which is pumped by a seeded Nd:YAG laser (Continuum PL8020). The relevant specifications of this laser system are given in figure 5. Calibration of the IR laser wavenumber accurate to better than $0.01\,cm^{-1}$ is accomplished by simultaneously recording optoacoustic spectra of reference gases [178] using the signal or idler output of the OPO, and interpolation between calibration lines is facilitated by monitoring transmission elaton markers (free spectral range $\sim$4 GHz) of the OPO oscillator. Calibrated line positions are

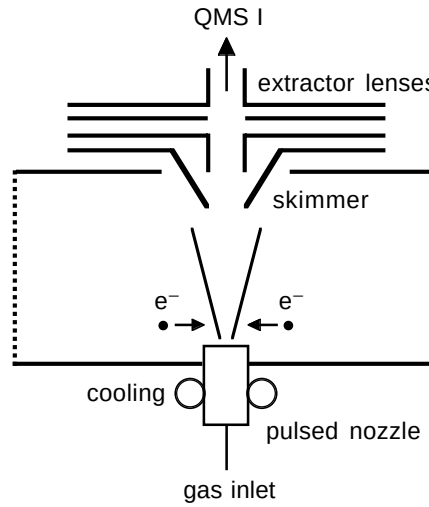

Figure 6. Scheme of the electron impact cluster ion source. A suitable gas mixture is expanded through a water-cooled pulsed valve (nozzle diameter ~ 1 mm) from high pressure ($p = 1$–30 bar) into vacuum. Electron impact ionization of the adiabatic expansion is accomplished by pulsed electron beams ($E \sim 50$–200 eV) emitted from two heated tungsten filaments close to the nozzle orifice. Cold cluster ions are formed by ion–molecule and clustering reactions in the high-pressure region of the plasma expansion. Generated ions are skimmed (diameter ~ 1–2 mm) and extracted into the first quadrupole mass spectrometer (QMS I).

corrected for the Doppler shift arising from the kinetic energy (several eV) of the ions in the octopole. The Doppler width arising from the spread of the kinetic energy (± 0.5 eV) is usually below the laser bandwidth (0.02 cm^{-1}). The fragment ion yield can be linearly normalized for laser intensity variations measured with an InSb IR detector.

The CH_3^+–Rg_n (Rg = He, Ne, Ar; $n \leq 8$) complexes were produced by expanding gas mixtures containing CH_4, He and Rg in the approximate ratio of $1:10^2:10^3$ at 5–8 bar backing pressure [54–56]. In some cases, the addition of H_2 appeared to be advantageous. The concentration of CH_4 had to be kept below 1% in order to avoid extensive polymerization leading to the predominant formation of larger $C_jH_k^+$ ions with $j \geq 2$. As expected, the production of clusters with larger n was enhanced for higher backing pressure and larger Rg concentration. The dependence of the partial cross-sections of electron impact ionization of CH_4 on the electron kinetic energy is well documented [53]. In addition, the ion–molecule reaction chemistry of CH_4–H_2–He plasmas has been discussed in detail [52]. Figure 7 reproduces a mass spectrum of the ion source recorded for the conditions used for CH_3^+–Ar_n production [54]. The spectrum is dominated by CH_n^+, $C_2H_n^+$, Ar^+ and CH_n^+–Ar. The IRPD spectra of CH_3^+–Rg_n were recorded by monitoring the following laser-induced reaction:

$$CH_3^+ - Rg_n + \nu \rightarrow CH_3^+ - Rg_m + (n - m)Rg. \quad (2)$$

Only the rupture of intermolecular bonds is observed on IR excitation. For the larger clusters ($n \geq 2$), more than one fragment channel may be observed. For example, figure 8 reproduces the mass spectrum obtained for resonant ν_3 excitation of CH_3^+–Ar_5 (mass selected with QMS I) and scanning QMS II to monitor both MD and LID [54]. CH_3^+–Ar_m fragments with $m = 1$ and 2 are produced by laser action,

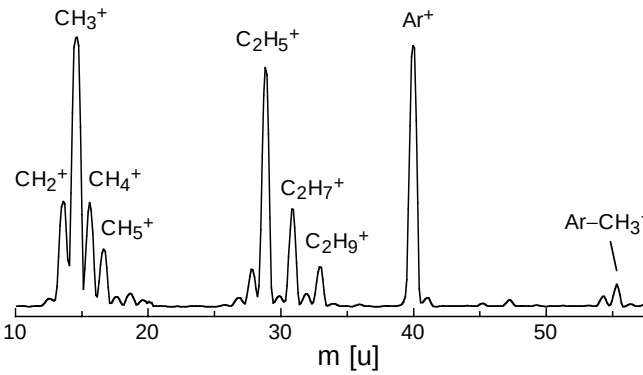

Figure 7. Mass spectrum of the ion source for the generation of CH_3^+–Ar by expanding a mixture of CH_4, He and Ar in the ratio 1:100:500 at 5 bar stagnation pressure [54]. The spectrum is dominated by CH_n^+, $C_2H_n^+$, Ar^+ and CH_n^+–Ar clusters. Signals of the intense peaks are saturated.

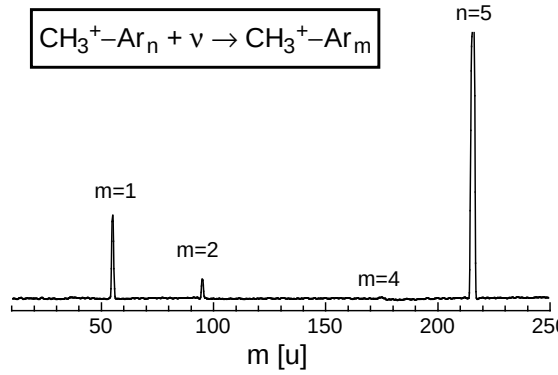

Figure 8. Mass spectrum obtained for resonant ν_3 excitation of CH_3^+–Ar_5 (mass selected with QMS I) and scanning QMS II to monitor both MD and LID [54]. CH_3^+–Ar_m fragments with $m=1$ and 2 are produced by laser action, whereas those with $m=4$ arise from metastable decay.

whereas those with $m=4$ arise from MD. In general, the IR spectra recorded in different fragment channels are similar. However, similar to studies on related systems [122, 126, 128, 131, 132, 140, 147, 154, 179–182], the range of fragment channels (m) observed for a given parent cluster (n) is rather narrow and this information can be used to estimate ligand binding energies (section 5.3).

2.2. *Theoretical approach*

As outlined in section 1, quantum chemical calculations are required to obtain a detailed and complete description of the intermolecular PES of ionic complexes, as well as the effect of monomer deformation on complexation. The calculations not only serve as a basis for comparison with available experimental data but also provide information of the properties of the PES not probed experimentally. These include dissociation energies, frequencies and intensities of so far unobserved inter- and intramolecular vibrations, attributes of less stable isomeric structures, isomerization and internal rotation barriers, properties of transition states and the nature

of the interaction as a function of the orientation (contribution of dispersion, induction, electrostatic and charge transfer forces). In the case of CH_3^+–Rg_n (Rg = He, Ne, Ar; $n \leq 2$), *ab initio* calculations have been carried out at the MP2(full) level using a basis set of aug-cc-pVTZ quality (tables 3 and 4) [54–56, 118, 119]. The actual basis, denoted by aug-cc-pVTZ$^{\#}$, is composed of Ahlrichs VTZ basis functions for the core electrons augmented with diffuse and polarization functions taken from the aug-cc-pVTZ basis. Test calculations for CH_3^+–He at higher theoretical levels and larger basis sets (MP4/aug-cc-pVTZ$^{\#}$, MP2/aug-cc-pVQZ) confirm that the MP2/aug-cc-pVTZ$^{\#}$ level provides a satisfactory approximation to the true interaction energy. In addition, MP2/aug-cc-pVTZ$^{\#}$ calculations for similar AH^+–Rg_n complexes yield structural, energetic and vibrational data in semiquantitative agreement with spectroscopic data [23, 121, 128, 132, 139, 143]. In contrast, calculations at the HF level largely underestimate the interaction strength and do not provide reliable PES parameters [54]. On the other hand, density functional calculations are not reliable for complexes with He and Ne as well as for complexes displaying charge transfer [121, 139]. In general, all coordinates are allowed to relax for the search of stationary points. Calculated interaction energies are fully counterpoise corrected for basis set superposition error (BSSE) [183]. The BSSE-corrected energies (E_1) are further corrected for the relaxation energy (E_2) caused by the complexation-induced deformation of the CH_3^+–Rg_{n-1} fragment, that is the well depth is obtained as $D_e = E_2 - E_1$ [184, 185]. In particular, for strongly bound ionic complexes, the deformation energy needs to be taken into account for obtaining semiquantitative agreement with experimental data [119]. Harmonic vibrational frequency analysis is performed to determine the nature of the stationary points obtained by gradient optimization. To account for the effects of anharmonicity, the harmonic frequencies are scaled by a factor of 0.9437 to bring the calculated ν_3 wavenumber of bare CH_3^+ into agreement with the experimental value, $\nu_3 = 3108.4\,cm^{-1}$ [52]. As the normal modes of CH_3^+ are only little affected on complexation, the nomenclature of the CH_3^+–Rg_n vibrations refer to the four intramolecular modes of CH_3^+ (ν_i, $i = 1$–4) and the intermolecular bending and stretching vibrations (ν_b, ν_s). The calculated planar equilibrium geometry of CH_3^+ in its $^1A_1'$ ground electronic state has D_{3h} symmetry, with a C–H bond length ($r_e = 1.0844$ Å) in good agreement with the experimental value ($r_e \sim 1.087$ Å [52]). Moreover, the scaled harmonic frequencies (other than ν_3) are also close to those determined from experiment (tables 1 and 4), confirming that the chosen theoretical level is sufficient for the description of the intramolecular coordinates in CH_3^+–Rg_n. Frequency calculations for larger CH_3^+–Ar_n clusters ($n \leq 4$) have been performed at the HF level [54]. Although this level underestimates the interaction, the results reliably predict experimental frequencies after the application of appropriate scaling procedures because the topologies of the HF and MP2 PESs are similar [54, 121, 139, 147]. Lower-level calculations of CH_3^+–Ar_n ($n \leq 3$) reported earlier [102] will not be discussed in detail because they do not reproduce the experimental observations [54]. Recent results of high-level calculations on CH_3^+–Ar_n ($n \leq 8$) [120] yield results similar to those obtained in the previous study of the smaller clusters ($n \leq 2$) [54] and will be described in more detail in section 5.1.

In addition to the characterization of stationary points of CH_3^+–Rg_n by gradient optimization, details of the 3D PESs of the CH_3^+–Rg dimers are investigated in more detail by calculating interaction energies for frozen intramolecular CH_3^+ coordinates (rigid monomer approximation, $r_e = 1.0844$ Å). Intermolecular interaction energies

Table 3. Structure (Å), rotational constants (cm^{-1}) and energies (cm^{-1}) of CH_3^+–Rg_n (figure 1) calculated at the MP2/aug-cc-pVTZ$^{\#}$ level [54–56].

Rg	n	Structure	r_e (r_{e1}, r_{e2})	R_e (R_{e1}, R_{e2})	θ_e/φ_e	A_e	B_e	C_e	E_1	E_2	D_e
—	0	D_{3h}	1.0844			9.482 899	9.482 899	4.741 450			
He	1	p-bound (C_{3v})	1.0829	1.8337	91.4°	4.757 86	1.352 609	1.352 609	761.6	54.5	707.1
He	1	H-bound (C_{2v})	1.0846, 1.0844	3.3650	119.9°	9.487 73	0.448 727	0.428 462	112.8	< 0.1	112.8
He	1	Side-bound (C_{2v})	1.0844, 1.0843	3.1269	119.9°	9.494 56	0.515 856	0.489 273	108.6	< 0.1	108.6
He	2	D_{3h}	1.0824	2.0000	90.0°	4.759 190	0.498 890	0.498 890	561.0	57.9	503.1
Ne	1	p-bound (C_{3v})	1.0825	2.1347	91.4°	4.761 059	0.410 634	0.410 634	1011.2	57.7	958.5
Ne	1	H-bound (C_{2v})	1.0848, 1.0844	3.3727	119.9°	9.494 459	0.169 669	0.166 690	210.6	0.1	210.5
Ne	1	Side-bound (C_{2v})	1.0843, 1.0842	3.1548	119.8°	9.504 586	0.193 456	0.189 597	199.3	0.2	199.1
Ne	2	D_{3h}	1.0810	2.2322	90.0°	4.770 954	0.083 866	0.083 866	799.5	54.1	745.4
Ar	1	p-bound (C_{3v})	1.0795	1.9543	99.6°	4.922 472	0.374 112	0.374 112	8912.3	2501.2	6411.1
Ar	1	H-bound (C_{2v})	1.0868, 1.0845	3.5147	119.6°	9.479 348	0.123 306	0.121 723	679.7	1.5	678.2
Ar	1	Side-bound (C_{2v})	1.0843, 1.0843	3.4096	119.4°	9.560 141	0.131 015	0.129 244	595.8	1.7	594.1
Ar	2[a]	C_{3v}	1.0778	2.0424, 2.8776	97.5°	4.883 237	0.034 589	0.034 589	14 934.5	14 166.9	767.6
Ar	2[a]	D_{3h}	1.0771	2.3692	90.0°	4.805 550	0.037 429	0.037 429	2165.1	1943.2	221.9

[a] In these calculations d functions on H and f functions on C and Ar have been removed from the aug-cc-pVTZ$^{\#}$ basis.

Table 4. Scaled harmonic vibrational frequencies (cm^{-1}), IR intensities (km mol^{-1}) and vibrational symmetry species of CH_3^+–Rg_n (figure 1) calculated at the MP2/aug-cc-pVTZ$^{\#}$ level [54–56].

Rg	n	Structure	ν_1	ν_2	ν_3	ν_4	ν_s	ν_b
—	0	D_{3h}	2917.9 (a_1'/0.0)	1360.2 (a_2''/7)	3108.4 (e′/148)	1365.3 (e′/34)		
He	1	p-bound (C_{3v})	2930.4 (a_1/0.4)	1337.4 (a_1/2)	3121.6 (e/140)	1361.2 (e/33)	193.2 (a_1/51)	569.6 (e/3)
He	1	H-bound (C_{2v})	2916.4 (a_1/0.4)	1361.2 (b_1/7)	3105.4 (a_1/87)	1367.3 (a_1/16)	84.6 (a_1/17)	68.5 (b_1/0.5)
					3108.4 (b_2/73)	1366.1 (b_2/16)		27.6 (b_2/1)
He	1	Side-bound (C_{2v})	2918.4 (a_1/0.0)	1360.1 (b_1/7)	3109.1 (a_1/74)	1363.2 (a_1/19)	73.7 (a_1/16)	47.9*i* (b_1/0.7)
					3109.4 (b_2/72)	1364.3 (b_2/18)		18.8 (b_2/2)
He	2	D_{3h}	2935.5 (a_1'/0)	1328.9 (a_2''/0)	3128.8 (e′/139)	1358.6 (e′/32)	194.6 (a_1'/0)	168.7 (e′/28)
							144.7 (a_2''73)	577.3 (e″/0)
Ne	1	p-bound (C_{3v})	2934.0 (a_1/0.5)	1335.8 (a_1/1)	3125.0 (e/136)	1363.4 (e/32)	161.7 (a_1/73)	467.8 (e/3)
Ne	1	H-bound (C_{2v})	2915.3 (a_1/2)	1364.1 (b_1/6)	3102.0 (a_1/102)	1367.3 (a_1/16)	76.0 (a_1/43)	97.4 (b_1/0.4)
					3108.7 (b_2/72)	1366.1 (b_2/16)		21.7 (b_2/1)
Ne	1	Side-bound (C_{2v})	2919.2 (a_1/0.0)	1360.8 (b_1/7)	3110.1 (a_1/73)	1362.0 (a_1/21)	66.0 (a_1/41)	65.7*i* (b_1/1)
					3110.4 (b_2/70)	1363.9 (b_2/18)		14.6 (b_2/2)
Ne	2	D_{3h}	2946.3 (a_1'/0)	1318.1 (a_2''/0)	3139.0 (e′/131)	1358.8 (e′/30)	109.1 (a_1'/0)	104.0 (e′/70)
							155.7 (a_2''/111)	541.7 (e″/0)
Ar	1	p-bound (C_{3v})	2957.0 (a_1/5)	1309.1 (a_1/15)	3126.1 (e/76)	1379.1 (e/32)	386.6 (a_1/140)	953.5 (e/0)
Ar	1	H-bound (C_{2v})	2899.4 (a_1/29)	1373.0 (b_1/5)	3078.0 (a_1/172)	1363.2 (a_1/10)	107.5 (a_1/66)	126.3 (b_1/0.0)
					3108.6 (b_2/67)	1373.0 (b_2/9)		87.6 (b_2/0.3)
Ar	1	Side-bound (C_{2v})	2919.4 (a_1/0.0)	1363.4 (b_1/6)	3110.5 (a_1/71)	1356.9 (a_1/32)	89.7 (a_1/57)	125.4*i* (b_1/0.7)
					3111.2 (b_2/61)	1360.5 (b_2/22)		23.9*i* (b_2/2)
Ar	2[a]	C_{3v}	2964 (a_1/2)	1303 (a_1/36)	3149 (e/77)	1389 (e/22)	75 (a_1/28)	89 (e/30)
							288 (a_1/240)	934 (e/0)
Ar	2[a]	D_{3h}	2965 (a_1'/0)	1269 (a_2''/75)	3168 (e′/94)	1380 (e′/19)	138 (a_1'/0)	150 (e′/37)
							159*i* (a_2''/426)	862 (e″/0)

[a] In these calculations d functions on H and f functions on C and Ar have been removed from the aug-cc-pVTZ$^{\#}$ basis. The scaling factor employed for this level is 0.942 35.

are calculated for a grid of intermolecular coordinates, R and γ. For each angle γ ($0°$, $\pm 5°$, $\pm 10°$, $\pm 20°$, $\pm 45°$, $\pm 67.5°$, $\pm 90°$), the energies of at least ten radial points in the vicinity of the minimum (spaced by 0.1 Å) are least-squares fitted to an analytic potential with terms accounting for Pauli exchange repulsion, $\exp(-\alpha R)$, and charge–induced dipole attraction, βR^{-4}. Minimum energies, $D_{\min}$, and corresponding intermolecular separations, $R_{\min}$, of these one-dimensional (1D) radial cuts through the 3D PES as a function of the bending angle γ provide a useful impression of the angular–radial coupling present in the CH_3^+–Rg dimers. To determine the effects of this coupling on the spectroscopic constants of CH_3^+–He and CH_3^+–Ne in a quantitative fashion, 1D–3D rovibrational calculations have been carried out on the rigid monomer PESs [118]. Details of the theoretical procedure and analytical representations of the PESs are available elsewhere [118].

3. CH_3^+–Rg dimers

3.1. *Potential energy surface*

3.1.1. *Stationary points*

In general, the relaxed PESs of all three investigated CH_3^+–Rg dimers (Rg = He, Ne, Ar) have similar topologies, with the main difference that the interaction strength increases in the order He < Ne < Ar [54–56]. The p-bound configuration with C_{3v} symmetry shown in figure 1(*b*) corresponds to the global minimum on all three potentials. Their structural, energetic and vibrational properties are summarized in tables 3 and 4. Figure 9 investigates the properties of the p-bound CH_3^+–Rg dimers as a function of the intermolecular separation (R) for the Rg atom approaching CH_3^+ along the C_3 symmetry axis. Although the dependences are qualitatively similar for all three dimers, they become more pronounced as the interaction strength increases (He < Ne < Ar). The open circles correspond to data of the equilibrium structures. In general, the dissociation energies increase with the size of the Rg atom ($D_e = 707$, 959, 6411 cm^{-1}), whereas the intermolecular separations are roughly constant ($R_e = 1.83$, 2.13, 1.95 Å). The latter effect is rationalized by the simultaneous increase in both the repulsive and the attractive terms in the potential. The intermolecular stretching wavenumbers amount to $\nu_s = 193$, 162 and 387 cm^{-1}. As expected, the degree of perturbation of CH_3^+ on complexation depends strongly on the strength of the interaction. They are modest for the weak interactions with He and Ne but drastic for the strong bond to Ar. The deformation energy amounts to $E_2 = 55$, 58 and 2501 cm^{-1} (corresponding to 8%, 6% and 39% of D_e). The main structural effect is that planar CH_3^+ ($\theta_e = 90°$) becomes pyramidal in CH_3^+–Rg ($\theta_e = 91.4°$, 91.4°, 99.6°). At the same time the C–H bond length decreases ($\Delta r_e = -0.0015$, -0.0019, -0.0049 Å). The shorter C–H bonds translate into larger frequencies for both the symmetric and asymmetric C–H fundamentals ($\Delta\nu_1 = 12.5$, 16.1, 39.1 cm^{-1}; $\Delta\nu_3 = 13.2$, 16.6, 17.7 cm^{-1}). The amount of charge transferred from Rg to the electrophilic CH_3^+ cation, ΔQ, is very small for He (0.03e) and Ne (0.008e) but substantial for Ar ($\sim 0.3e$). This result indicates a qualitative change in the bonding mechanism from mainly induction (He, Ne) to partial charge transfer (Ar) as the size of the Rg increases (section 3.5). Comparison between HF and MP2 calculations for CH_3^+–Ar demonstrates that the HF level is not adequate for a realistic description of the PES because it severely underestimates the intermolecular interaction and the resulting monomer deformation [54]: for example, the HF/aug-cc-pVTZ$^{\#}$ and MP2/aug-cc-pVTZ$^{\#}$ data for

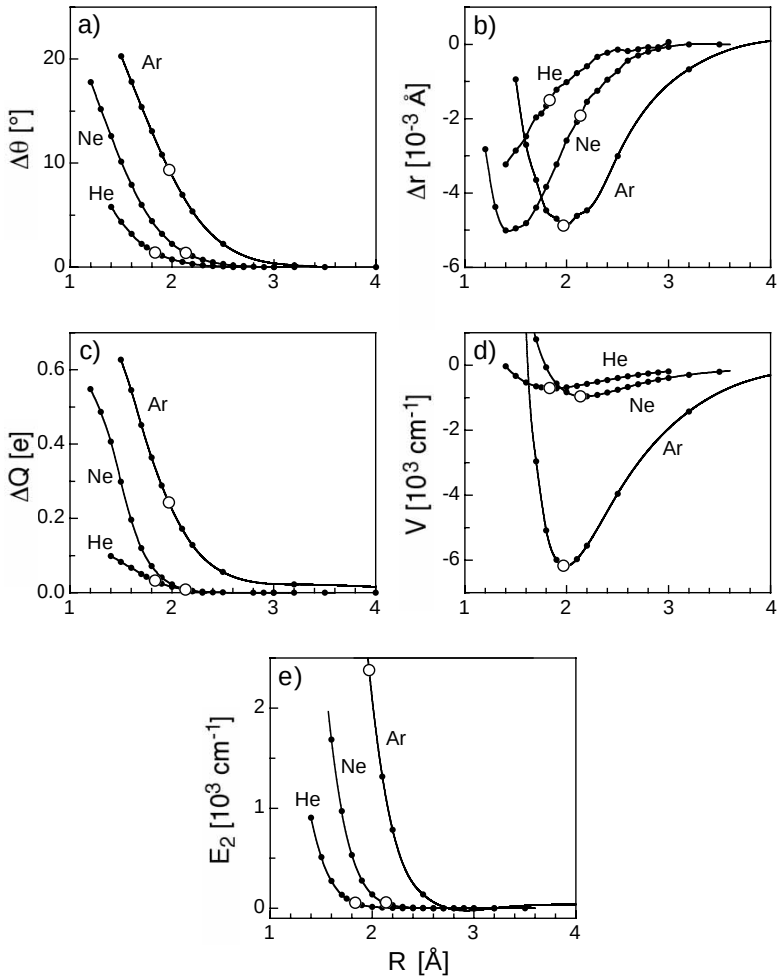

Figure 9. Properties of CH_3^+–Rg (Rg = He, Ne, Ar) as a function of the intermolecular separation (R) for the Rg atom approaching CH_3^+ along the C_3 symmetry axis (calculated at the MP2/aug-cc-pVTZ$^{\#}$ level) [54–56]: (*a*) $\Delta\theta = \theta_e - 90°$; (*b*) $\Delta r = r_e^{\text{dimer}} - r_e^{\text{monomer}}$; (*c*) negative charge transferred from Rg to CH_3^+ (ΔQ); (*d*) intermolecular potential (V); (*e*) relaxation energy (E_2). The open circles correspond to the values at the minima of the potentials. Although the dependences are qualitatively similar for all three dimers, they become more pronounced as the interaction strength increases (He < Ne < Ar).

p-bound CH_3^+–Ar are $D_e = 2023$ versus $6411\,cm^{-1}$, $R_e = 2.36$ versus $1.95\,Å$, $\Delta\theta_e = 3.2°$ versus $9.6°$, $\Delta r_e = -0.0043$ versus $-0.0049\,Å$, $E_2 = 310$ versus $2501\,cm^{-1}$, $\Delta Q \sim 0.15e$ versus $0.3e$. Similarly to the HF level, previous MP2 calculations using a smaller basis set (6-311G) perform poorly [102]. On the other hand, recent high-level MP2 [120] and density functional calculations [104] for CH_3^+–Ar are in accord with the MP2/aug-cc-pVTZ$^{\#}$ data [54].

In addition to the deep p-bound global minima, two further stationary points are located on the CH_3^+–Rg PES. Both the H-bound local minimum in figure 1(*c*) and the side-bound transition state in figure 1(*d*) are planar structures with C_{2v} symmetry (tables 3 and 4). In general, the interaction in the H-bound dimers ($D_e = 113$, 211,

678 cm^{-1}; $R_e = 3.37$, 3.37, 3.51 Å; $\nu_s = 85$, 76, 108 cm^{-1}) is comparable with that in the side-bound structures ($D_e = 109$, 199, 594 cm^{-1}; $R_e = 3.13$, 3.15, 3.41 Å; $\nu_s = 74$, 66, 90 cm^{-1}). As a consequence of the fairly isotropic PES (with respect to the azimuthal angle), the barriers for in-plane rotation of CH_3^+ around its c axis are rather low. In general, both planar structures have significantly weaker and longer intermolecular bonds than the corresponding p-bound global minima. Hence, the effects of complexation on the monomer properties are minor, leading to small values of E_2 ($< 2\,cm^{-1}$), Δr_e (≤ 0.0024 Å) and $\Delta\varphi_e$ ($\leq 0.6°$). Moreover, as charge transfer is small ($\Delta Q < 0.02e$ for Ar), induction forces dominate the attractive part of the potential for the planar configurations.

3.1.2. *Rigid monomer potential*

Figure 10 compares properties of the rigid monomer PESs of CH_3^+–Rg [55, 56, 119]. The PESs of CH_3^+–He and CH_3^+–Ne show deep global minima at $\gamma = 0°$ and steep rises in the minimum energy, D_{min}, toward both the H-bound ($\gamma = 90°$) and the side-bound ($\gamma = -90°$) structures, which leads to pronounced angular–radial coupling. Small deviations from the equilibrium structure cause a strong reduction in D_{min} and a large increase in the corresponding R_{min} value. The corresponding PES of CH_3^+–Ar shows similar trends to those of CH_3^+–He and CH_3^+–Ne, except the differences near $\gamma = 0°$ which arise from the severe effects of the neglect of monomer relaxation (section 3.1.3). The nearly symmetric behaviour of both D_{min} and R_{min} with respect to γ confirms that the PESs are nearly independent of the azimuthal angle (in the mid- and long-range part). The large difference in the binding energies of the planar and p-bound geometries results in deep global minima with high barriers for internal CH_3^+ rotation around its a and b axes ($V_b \sim 600$, 750, 6000 cm^{-1}).

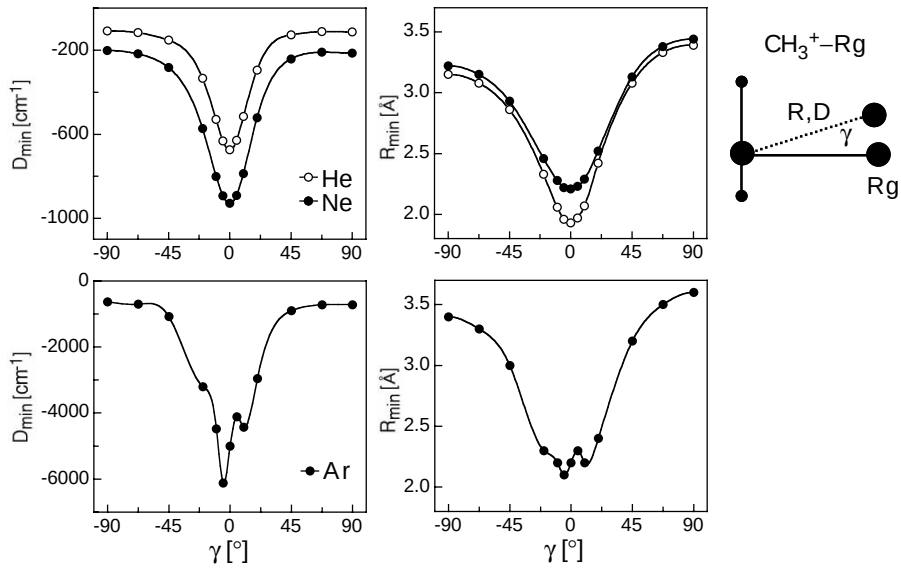

Figure 10. Properties of the rigid monomer PES of CH_3^+–Rg (Rg = He, Ne, Ar) calculated at the MP2/aug-cc-pVTZ# level [55, 56, 119]. The minimal separations (R_{min}) and potential energy depths (D_{min}) of 1D radial cuts through the 3D PES are plotted as a function of the bending angle (γ). $\gamma = -90°$ and 90° correspond to side-bound and H-bound structures respectively.

This large angular anisotropy confines the Rg atoms in the ground vibrational state more or less to the p-bound region near the $2p_z$ orbital of C and gives rise to high (scaled) harmonic intermolecular bending frequencies of the p-bound equilibrium structure ($\nu_b = 570,\ 468,\ 954\,cm^{-1}$) which significantly exceed the corresponding stretching frequencies ($\nu_s = 193,\ 162,\ 387\,cm^{-1}$). On the other hand, the similar energies of H-bound and side-bound structures imply a low barrier for internal CH_3^+ rotation around its c axis ($V_b \sim 4,\ 11,\ 84\,cm^{-1}$) and a nearly isotropic potential along the azimuthal angle. This view is supported by the low frequencies of the H-bound structures for the in-plane bending vibration ($\nu_b = 19,\ 22,\ 88\,cm^{-1}$). The effects of the strong angular–radial coupling on the interpretation of the spectroscopic constants will be discussed in detail in section 3.4.

3.1.3. *Effects of monomer relaxation*

The effects of monomer relaxation by complexation have been discussed in section 3.1.1 by considering figure 9, which describes selected parameters of CH_3^+–Rg as a function of the intermolecular separation, including structural deformation (Δr, $\Delta\theta$), its required energy (E_2) and the charge transfer from Rg to CH_3^+ (ΔQ). Because the deformation is mainly induced by charge transfer, which is most efficient for p-bound structures, the effects are most pronounced for geometries with (near) C_{3v} symmetry. As the relaxation depends on ΔQ, the deformation is largest for Ar and only modest for both Ne and He.

To illustrate the magnitude of the effect in the limit of weak interaction, the radial potentials of CH_3^+–He calculated for p-bound orientations ($\gamma = 0°$) without and with relaxing the CH_3^+ structure are compared in figure 11 [119]. As expected, the differences are small at long range and increase for decreasing R. The effects are significant at the equilibrium geometry ($D_e = 676$ versus $709\,cm^{-1}$, $R_e = 1.93$ versus $1.86\,Å$) and become very large at short range (e.g. $V = -230$ versus $-529\,cm^{-1}$ at $R = 1.6\,Å$), where relaxation leads to a substantial additional stabilization. The minimum on the relaxed PES occurs at slightly longer intermolecular separation than obtained by gradient optimization ($D_e = 707\,cm^{-1}$, $R_e = 1.83\,Å$), because the

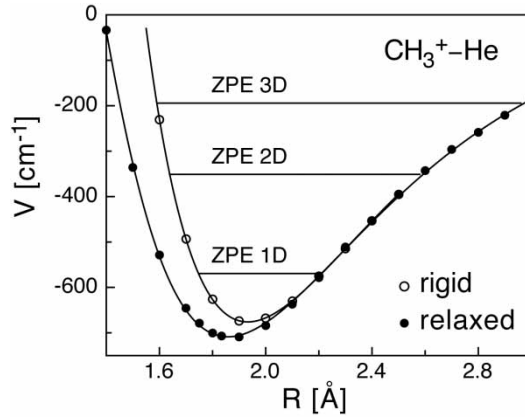

Figure 11. 1D radial cuts through the CH_3^+–He PES along the C_3 symmetry axis for rigid and relaxed CH_3^+ internal coordinates calculated at the MP2/aug-cc-pVTZ$^{\#}$ level [119]. The zero-point levels derived for 1D, 2D and 3D representations of the rigid monomer potential are indicated [118]. Monomer relaxation leads to a slightly stronger and shorter intermolecular bond.

former corresponds to the minimum obtained on the BSSE-corrected PES, whereas the latter is derived on the uncorrected PES [24, 184]. The preceding discussion illustrates that, although the rigid monomer approximation may provide a semi-quantitative picture of the PES in the weakly bound CH_3^+–He and CH_3^+–Ne dimers near the equilibrium structure, the monomer deformation cannot be ignored when an interaction potential with spectroscopic accuracy is required.

The CH_3^+–Ar dimer is an illustrative example for a strong intermolecular bond, which via significant partial charge transfer induces a large monomer deformation even at the equilibrium (figure 9). The deformation energy of 2501 cm^{-1} amounts to 39% of D_e. The importance of monomer relaxation is demonstrated by the 'misleading' rigid monomer PES of CH_3^+–Ar shown in figure 10. In contrast to the minimum obtained by gradient optimization, the minimum on the rigid monomer PES does not occur at $\gamma = 0^\circ$ (i.e. for a structure with C_{3v} symmetry) but near $\gamma = -5^\circ$ because the latter structure is closer to the relaxed equilibrium geometry. This example shows that for strongly bound complexes the rigid monomer approximation may lead to potential minima with different symmetry to the global minima on the relaxed PES.

3.2. *IR spectra*

Inspection of table 4 reveals that the ν_3 mode is the only strongly IR-active vibration of the CH_3^+–Rg dimers expected in the range of the C–H stretch fundamentals. The $\nu_3(e')$ mode of isolated CH_3^+ corresponds to the doubly degenerate asymmetric C–H stretch with a wavenumber of 3108.4 cm^{-1} [52]. According to the calculations, the $\nu_3(e)$ frequencies of the p-bound CH_3^+–Rg dimers feature only small blue shifts by Rg complexation. Figure 12 compares the experimental IRPD spectra of the CH_3^+–Rg dimers in the vicinity of the ν_3 fundamental of CH_3^+ (indicated by the arrow below the wavenumber scale) [54–56]. Both the CH_3^+–He and the CH_3^+–Ne spectra display a single vibrational transition, and the analysis of its rovibrational structure is consistent with an assignment to the ν_3 fundamental of a p-bound complex. In contrast to the intense rotationally resolved ν_3 bands of CH_3^+–He/Ne, the CH_3^+–Ar spectrum features a weak, unresolved and broad band centred at around 3145 cm^{-1} (full width at half-maximum $\sim 130\,cm^{-1}$). As the dissociation energy of CH_3^+–Ar ($D_0 \sim 4000\,cm^{-1}$ [102]) is larger than the ν_3 frequency, the ν_3 fundamental cannot occur in a one-photon IRPD spectrum (multiphoton transitions are unlikely using the available laser intensity of $< 1\,MW\,cm^{-2}$ [186, 187]). Consequently, the broad band has to be attributed to overlapping sequence transitions of the type $\nu_3 + \nu_x \leftarrow \nu_x$, where ν_x represents a vibration with a wavenumber in excess of $\sim 1000\,cm^{-1}$. Neglecting cross-anharmonicities, the ν_3 wavenumber of CH_3^+–Ar can be estimated as $3145 \pm 30\,cm^{-1}$.

The rotational structure of the $\nu_3(e)$ fundamentals of CH_3^+–He and CH_3^+–Ne is characteristic of a perpendicular transition of a prolate symmetric top. Adjacent Q branches of $\Delta K = K' - K'' = \pm 1$ subbands (denoted by ${}^{\Delta K}Q_K$) are spaced by roughly $2[A'(1-\xi_3) - B'] \approx 7.6$ (Ne) and 6.5 (He) cm^{-1}. These values are close to $2C'(1-\xi_3) \approx 8.1\,cm^{-1}$ of CH_3^+ [64], indicating that the Rg atoms are located on the C_3 symmetry axis. The unambiguous assignment of the rotational K and J quantum numbers is based on missing P and R branch lines with $J < K$ and the relative intensities of the unresolved Q branches: the ${}^rQ_0$ branch is most intense and the Q branches originating from $K = 3n$ are enhanced compared with those from $K = 3n \pm 1$ owing to their double nuclear spin statistical weights in a C_{3v} symmetric

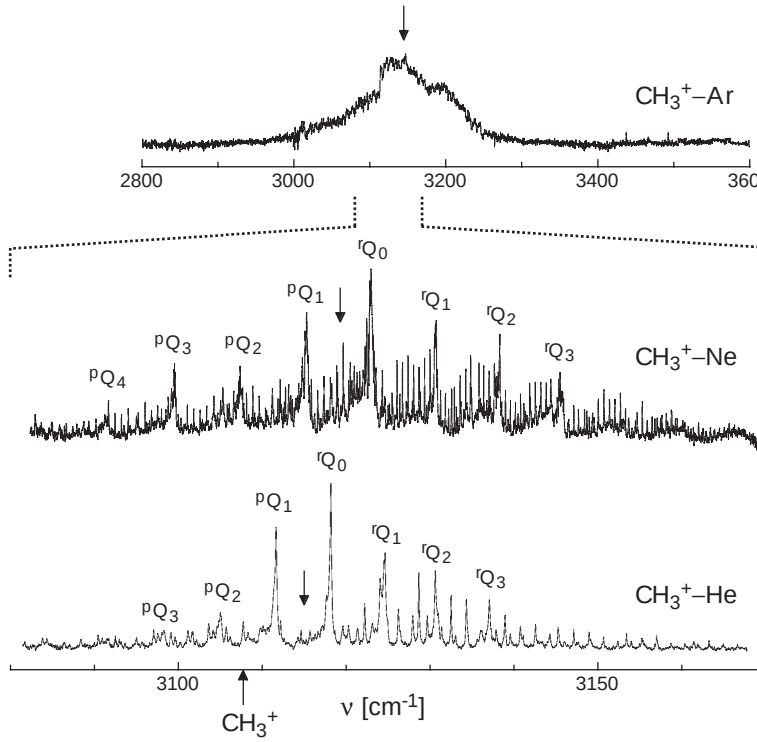

Figure 12. IRPD spectra of CH_3^+–Rg (Rg = He, Ne, Ar) in the range of the ν_3 vibration recorded in the CH_3^+ fragment channel [54–56]. The spectra of CH_3^+–He and CH_3^+–Ne correspond to the ν_3 fundamentals and have the rotational structure appropriate for a prolate symmetric top. The Q branches of the $\Delta K = K' - K'' = \pm 1$ subbands are given in the notation ${}^{\Delta K}Q_K$. The broad and unresolved band in the CH_3^+–Ar spectrum (recorded over a much larger spectral range) corresponds to overlapping sequence transitions of the form $\nu_3 + \nu_x \leftarrow \nu_x$. The arrows indicate the positions of the ν_3 band origins, approximated by $\nu_3 - \xi_3 A'$, derived from the rovibrational fits (He, Ne) or the weighted band centre (Ar).

complex with three equivalent protons. In total, 68 (He) and 105 (Ne) rotational line positions are least-squares fitted to a semirigid symmetric top Hamiltonian, including a vibrational band origin, rotational and centrifugal distortion terms, and first-order Coriolis coupling for the degenerate upper vibrational state ($\ell = 0$ for $v_3 = 0$ and $\ell = \pm 1$ for $v_3 = 1$) [188]:

$$E(J,K) = \nu_0 + BJ(J+1) + (A-B)K^2 - D_J J^2(J+1)^2 - D_{JK}J(J+1)K^2 - D_K K^4 - 2\ell\xi_3 AK. \quad (3)$$

Table 5 summarizes the molecular constants for both vibrational states derived from the fits. The standard deviation of the fits is typically of the order of the laser bandwidth ($\approx 0.02\,\mathrm{cm}^{-1}$) and less than the widths of single rotational lines (0.12 and $0.04\,\mathrm{cm}^{-1}$ for He and Ne). To demonstrate the quality of the fits, figure 13 compares a selected part of the CH_3^+–Ne spectrum with a simulation using a rotational temperature of 30 K.

As the dissociation energy of CH_3^+–Ar ($D_0 \sim 4000\,\mathrm{cm}^{-1}$) is below the frequencies of the first C–H stretch overtones ($> 5800\,\mathrm{cm}^{-1}$), the latter vibrations can be

Table 5. Molecular constants (cm^{-1}) of rotationally resolved transitions of CH_3^+–Rg_n determined from fitting rotational line positions to the Hamiltonian (3) [54–56].[a]

Vibrational state	Parameter	CH_3^+–He	CH_3^+–Ne	CH_3^+–Ne_2	CH_3^+–Ar	CH_3^+–Ar_2[b]
Ground state (a_1)	B''	1.0053(19)	0.357 20(92)	0.076 150(90)	0.352 75(32)	0.0358(3)
	$D''_J \times 10^6$	282(18)	10.0(2.6)	0.225(86)	2.14(65)	2.0(8)
	$D''_{JK} \times 10^6$	−450(160)	56(27)	0[d]	100(37)	
	$D''_K \times 10^6$	540(320)	560(359)	0[d]	260(760)	
ν_3 (e)	$\nu_3 - \xi_3 A'$ [c]	3115.047(18)	3119.371(20)	3129.2986(37)	3145 ± 30	3151.6(5)
	$A'(1-\xi_3)$	4.2356(52)	4.2000(20)	4.168 30(82)		
	$A' - A''$	−0.0391(34)	−0.0564(64)	−0.0274(32)		
	B'	0.9954(19)	0.354 70(86)	0.075 739(92)		0.0350(3)
	$D'_J \times 10^6$	297(19)	11.0(2.0)	0.200(90)		1.3(8)
	$D'_{JK} \times 10^6$	−440(110)	0[d]	0[d]		
	$D'_K \times 10^6$	420(170)	0[d]	0[d]		

[a] Numbers in parentheses represent 2σ limits.
[b] Obtained from a fit of P and R branch transitions of the $K = 1 \leftarrow 0$ subband.
[c] Absolute uncertainty of calibration is $\pm 0.01\,cm^{-1}$. The values for the Ar complexes assume $\xi_3 = 0$.
[d] Constrained to this value in the fit.

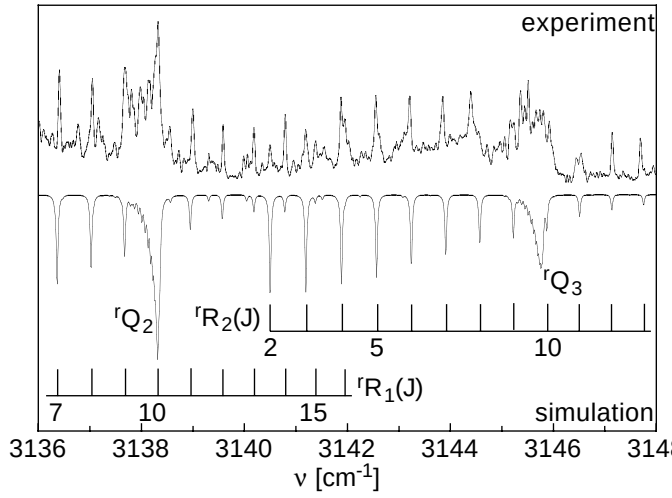

Figure 13. Expanded view of the IRPD spectrum of CH_3^+–Ne compared with a simulation using the molecular constants in table 5, a convolution width of $0.04\,cm^{-1}$ and a rotational temperature of $T_{rot} = 30\,K$ [56]. The notation corresponds to ${}^{\Delta K}\Delta J_K(J)$.

observed in an IRPD spectrum by single-photon absorption from the ground vibrational state. Indeed, the IRPD spectrum in figure 14 shows the fully rotationally resolved spectra of all four possible C–H stretch overtone (and combination) transitions of CH_3^+–Ar, namely $2\nu_1(a_1)$ at $5912\,cm^{-1}$, $\nu_1 + \nu_3(e)$ at $6028\,cm^{-1}$ and both components of $2\nu_3$ at 6243 (e, $\ell = 2$) and 6191 (a_1, $\ell = 0$) cm^{-1} [54]. Expanded views of the $2\nu_3(e)$ and $2\nu_1(a_1)$ bands with detailed rotational assignments may

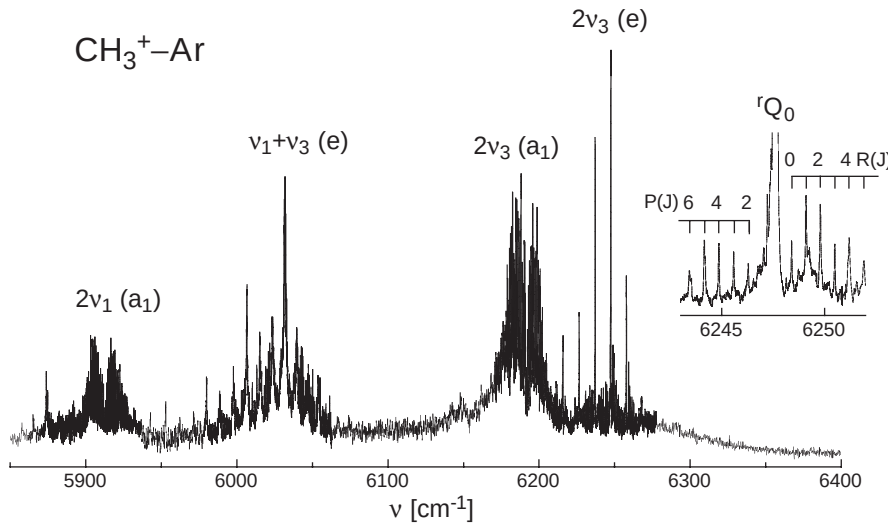

Figure 14. Overview of the IRPD spectrum of CH_3^+–Ar in the range of the first C–H stretch overtones recorded in the CH_3^+ fragment channel [54]. All observed transitions have the rotational structure appropriate for parallel or perpendicular transitions of a prolate symmetric top. The inset shows part of the $K=1 \leftarrow 0$ subband of $2\nu_3$(e) in more detail.

Table 6. Molecular constants (cm^{-1}) of rotationally resolved overtone transitions of CH_3^+–Ar determined from fitting rotational line positions to the Hamiltonian (3) [54].[a]

Parameter	$2\nu_3$ (a_1)	$2\nu_3$ (e)	$2\nu_1$ (a_1)	$\nu_3+\nu_1$ (e)
$\nu_0-\ell\xi_3A'$ [b]	6191.058(11)	6242.566(15)	5911.936(11)	6027.70(17)
$A'(1-2\xi_3)$		5.539(11)		
$A'(1-\xi_3)-B'$				3.966(22)
$A'-A''$	−0.0777(26)	−0.065(13)	−0.0853(48)	
$A'-A''-(B'-B'')$				−0.115(13)
B'	0.353 02(34)	0.352 02(52)	0.351 57(31)	
$D'_J\times10^6$	2.62(70)	6.0(3.1)	2.36(54)	
$D'_{JK}\times10^4$	1.39(41)	1.81(87)	0.92(38)	
$D'_K\times10^4$	2.5(7.7)	31(14)	13.4(8.6)	

[a] Numbers in parentheses represent 2σ limits.
[b] Absolute uncertainty of calibration is $\pm0.01\,cm^{-1}$. ℓ corresponds to the number of ν_3 quanta.

be found in [54]. The transitions exhibit a rotational structure expected for either a parallel (a_1) or a perpendicular (e) transition of a prolate symmetric top. The molecular constants obtained from least-squares fits of several hundred line positions to Hamiltonian (3) are listed in tables 5 and 6.

3.3. *Structural, energetic and dynamical properties*

The rovibrational analysis of the CH_3^+–Rg spectra (including vibrational frequencies and splittings, rotational constants, nuclear spin statistical weights) is

fully consistent with p-bound equilibrium structures featuring three equivalent protons (C_{3v}, figure 1(*b*)), in agreement with the *ab initio* calculations. All other geometries, such as the H-bound structures, can safely be excluded on the basis of the spectroscopic observations. The molecular constants obtained for CH_3^+–Rg can be used to derive several properties of the intermolecular bonds and their influence on the intramolecular parameters in both the ground and vibrationally excited states (table 7).

3.3.1. *Vibrational frequencies*

First, the vibrational frequency shifts of the ν_3 band origins are considered (indicated by arrows in figure 12). Neglecting Coriolis coupling, the ν_3 band origins of CH_3^+–He and CH_3^+–Ne are obtained from the fits of the rotational structure as 3115.1 and 3119.4 cm^{-1} respectively. Because of the lack of rotational structure, the ν_3 wavenumber of CH_3^+–Ar is less certain and estimated as $3145 \pm 30\,cm^{-1}$. The experimental ν_3 blue shifts from the value in bare CH_3^+ (3107.9 cm^{-1} [52]) are thus 7.2 (He), 11.5 (Ne) and $\approx 37 \pm 30$ (Ar) cm^{-1} and increase with the interaction strength. This trend is in line with the corresponding calculated shifts of 13, 17 and 18 cm^{-1} and reflects directly the complexation-induced contraction of the C–H bonds. The ν_3 frequencies of CH_3^+–He and CH_3^+–Ne are closer to ν_3 of CH_3^+ than to ν_3 of CH_3, indicating that charge transfer is small in both dimers. Moreover, the ν_3 shifts scale almost linearly with the polarizability of He and Ne, confirming that the attraction is based on induction. In contrast, ν_3 of CH_3^+–Ar is nearer to ν_3 of CH_3, implying that charge transfer is substantial in this complex. In the limit of adiabatic separation between inter- and intramolecular degrees of freedom, the observed ν_3 blue shifts correspond directly to the decrease of the intermolecular interaction strength on vibrational excitation. Assuming dissociation energies of $D_0 = 193$ (He), 474 (Ne) and ~ 4000 (Ar) cm^{-1} for the ground vibrational states of CH_3^+–Rg [102, 118], the ν_3 shifts correspond to a reduction of 3.7%, 2.4% and $\sim 1\%$ in binding energy for the excited states. The relatively small changes on ν_3 excitation are consistent with the weak coupling between the C–H coordinate (r) and the intermolecular degrees of freedom.

Experimental frequencies for the first C–H stretch overtones (and combination bands) of bare CH_3^+ are not available, demonstrating the challenges involved in the spectroscopic characterization of even simple ions. Theoretical values derived from variational calculations on a sophisticated *ab initio* PES are listed in table 1 [73]. Corresponding frequencies obtained from a non-rigid inverter model are presented elsewhere [54, 189]. The experimental band origins for $2\nu_1$, $\nu_3 + \nu_1$ and both $2\nu_3$ components of CH_3^+–Ar (table 1) provide the first experimental information on the corresponding values in bare CH_3^+, demonstrating that cluster ion spectroscopy can provide valuable information on the properties of the monomer ion (messenger technique [136, 181, 190, 191]). The dimer frequencies are expected to be similar to the monomer values, as the Ar complexation shifts of the C–H stretch modes are small. In general, the $2\nu_1$, $\nu_3 + \nu_1$ and $2\nu_3$ frequencies of CH_3^+–Ar are slightly higher than those calculated for CH_3^+ but lower than those of CH_3 (table 1), consistent with the partial electron transfer from Ar to CH_3^+. Moreover, the experimental CH_3^+–Ar frequencies are well reproduced by a local mode-coupled Morse oscillator model (table 1) [54, 79].

Table 7. Properties of CH_3^+–Rg_n ($n = 1, 2$) derived from *ab initio* calculations (MP2/aug-cc-pVTZ$^{\#}$ level) and IRPD spectroscopy [54–56].

	CH_3^+–He_n		CH_3^+–Ne_n		CH_3^+–Ar_n		
	$n=1$ (C_{3v})	$n=2$ (D_{3h})	$n=1$ (C_{3v})	$n=2$ (D_{3h})	$n=1$ (C_{3v})	$n=2$ (C_{3v})[a, b]	$n=2$ (D_{3h})[b, c]
Ab initio							
D_e (cm^{-1})	707.1	503.1	958.5	745.4	6411.1	767.6	221.9
R_e (Å)	1.8337	2.0000	2.1347	2.2322	1.9543	$R_{1e}=2.0424$ $R_{2e}=2.8776$	2.3692
θ_e	91.4°	90°	91.4°	90°	99.6°	97.5°	90°
ΔQ (e)	0.03	0.016	0.008	0.004	0.3	$\Delta Q_1=0.18$ $\Delta Q_2=0.002$	0.03
E_2 (cm^{-1})	54.5	57.9	57.7	54.1	2501.2	141 66.9	1943.2
Δr_e (Å)	−0.0015	−0.0020	−0.0019	−0.0034	−0.0049	−0.0067	−0.0074
ω_s (cm^{-1})	205	180[d]	171	140 [d]	410 (393)[b]	192 [d]	
ω_b (cm^{-1})	604		496		1010(1003)[b]		
$\Delta\nu_3^{calc}$ (cm^{-1})	13.4	20.4	16.6	30.6	17.7 (28)[b]	41	60
Experiment ($v_3=0$)							
R_{cm} (Å)	2.176(3)		2.300(3)	2.344(2)	2.053(3)	$R_1+R_2=4.84(2)$	
$R_{cm}-R_e$ (Å)	0.34		0.17	0.11	0.10		
k_s (N m^{-1})	2.4(2)		8.9(3.0)		51(17)		
ω_s (cm^{-1})	113(4)		132(22)		281(46)		
Experiment ($v_3=1$)							
$\nu_3-\xi_3A'$ (cm^{-1})	3115.05(2)		3119.37(2)	3129.30(4)	3145(30)	3151.6(5)	
$\Delta(\nu_3-\xi_3A')$ (cm^{-1})	7.19(2)		11.52(2)	21.45(4)	37(30)	43.8(5)	
R_{cm} (Å)	2.187(2)		2.308(3)	2.350(2)			
ΔR_{cm} (Å)	0.011(4)		0.008(4)	0.006(3)			
k_s (N m^{-1})	2.2(2)		7.9(1.5)				
ω_s (cm^{-1})	109(4)		125(12)				

[a] Global minimum.
[b] In these calculations the d functions on H and f functions on C and Ar have been removed from the aug-cc-pVTZ$^{\#}$ basis.
[c] Transition state.
[d] Average frequency of symmetric and asymmetric stretch.

3.3.2. *Interpretation of rotational constants*

By treating the CH_3^+–Rg dimers as pseudodiatomic molecules, the rotational B constants can be used to estimate the vibrationally averaged intermolecular C–Rg bond length, R_{cm} (centre-of-mass separation), assuming that CH_3^+ is not distorted on complexation [192]. The obtained values are $R_{cm}/\text{Å} = 2.176$ (He), 2.300 (Ne) and 2.053 (Ar) for the ground vibrational state. The C–Rg bond length estimated from the rotational B constant is relatively insensitive to the effect of CH_3^+ deformation ($R_{cm} - R_{C-Rg} < 0.008$, 0.005, 0.04 Å), because of the small mass of the protons. Unfortunately, the spectroscopic data do not offer experimental information on the H–C–Rg bond angle (θ). The harmonic force constant and stretching frequency for the intermolecular C–Rg bond can be estimated from the rotational and centrifugal distortion constants [192] as $k_s = 2.4$, 8.9 and 51 N m^{-1} and $\omega_s = 113$, 132 and 281 cm^{-1} for He, Ne and Ar respectively. As expected, both quantities increase with the size of the Rg atom because of the stronger interaction. As the interaction is slightly weaker in the ν_3 excited state, R_{cm} are slightly longer, whereas k_s and ω_s are smaller (table 7). The A rotational constants of all three CH_3^+–Rg dimers are of the order of 5 cm^{-1}, confirming that the Rg atom is located on the C_3 symmetry axis. The small decrease in the A constant on C–H stretch excitation is a further signature of the longer vibrationally averaged C–H bonds in the excited states. In the case of CH_3^+–Ar, rotational constants are not available for the ν_3 state but are for the ground state and all states with two C–H stretch quanta (table 6). In general, they show the same trend as derived for ν_3 of CH_3^+–He and CH_3^+–Ne. Excitation of two C–H stretch quanta leads usually to a slight reduction in A and B, reflecting increases in r and R_{cm} and a reduction in the intermolecular bond strength. Although the C–H stretch overtones are not known for bare CH_3^+, the rotational constants of the corresponding CH_3^+–Ar transitions suggest that the CH_3^+ levels should be lower in frequency than the CH_3^+–Ar levels.

3.3.3. *Predissociation dynamics*

First, the dissociation energies of CH_3^+–Rg are considered. The observation of the ν_3 fundmentals in the single-photon IRPD spectra of CH_3^+–Rg (Rg = He, Ne) provides an upper limit to their binding energies in the ground vibrational state of $D_0 < 3120$ cm^{-1}. This result is consistent with the most accurate theoretical values of $D_e = 707$ and 959 cm^{-1} and $D_0 = 193$ and 474 cm^{-1} for Rg = He and Ne respectively [55, 56, 118]. On the basis of the IRPD spectrum of CH_3^+–Ar, the dissociation energy of this complex may be bracketed as $\nu_3 < D_0 < 2\nu_1$, yielding $D_0 = 4525 \pm 1375$ cm^{-1} [54]. This value is in line with the best theoretical ($D_0 = 5127$ cm^{-1} at the QCISD(T)/6-311++G(2df,2pd) level [120]) and thermochemical ($-\Delta H^0 = 3950 \pm 700$ cm^{-1} [102]) data.

The linewidths of single rotational lines may be limited by instrumental factors (here, the laser bandwidth of 0.02 cm^{-1}), inhomogeneous broadening (such as spectral congestion) or homogeneous broadening arising from fast relaxation processes. The latter may include IVR and/or VP. The large width of the ν_3 band of CH_3^+–Ar (~ 130 cm^{-1}) is certainly due to unresolved overlapping sequence transitions [54]. On the other hand, the width of single rotational lines of the ν_3 fundamental of CH_3^+–He (0.12 cm^{-1}) is limited by fast decay of the optically prepared vibrational state, $\tau_3 \sim 50$ ps [55]. Similar short lifetimes have been observed for ν_1 of N_2H^+–He (38 ps [129]), whereas the ν_1 lifetimes of OCH^+–He [124] and OH^+–He [137] exceed 200 ps. The rather different lifetimes in these weakly bound

ion–He complexes reflect the different coupling strengths of the proton stretch vibrations with other intramolecular modes and the dissociation continuum. Interestingly, the decay process for ν_3 of CH_3^+–Ne ($\tau_3 > 120$ ps [56]) is slower than that for CH_3^+–He. This is possibly due to the fact that CH_3^+–He has more open final state channels for predissociation from the ν_3 state. For example, the ν_1 state of the CH_3^+ fragment is nearby the ν_3 state of CH_3^+–He (because $D_0 \sim 190\,cm^{-1} \sim \nu_3 - \nu_1$), and this (near) resonance may be responsible for the fast decay. On the other hand, this fragmentation channel is certainly closed for CH_3^+–Ne ($D_0 \sim 500\,cm^{-1}$), which could explain the slower dissociation. Significantly, the rotational linewidths of all observed overtone transitions of CH_3^+–Ar are limited by the laser bandwidth ($0.02\,cm^{-1}$), providing a lower limit for the lifetime of all investigated upper states of $\tau > 250$ ps. This observation implies weak coupling between the C–H stretch overtones/combinations and the intermolecular degrees of freedom and is compatible with the small frequency shifts of these transitions on Ar complexation [54].

3.4. *CH_3^+–Rg as prototype disk-and-ball dimers*

In this section, the CH_3^+–Rg dimers will be considered as prototypes for p-bound disk-and-ball dimers [118]. The PESs of such complexes feature special characteristics, including (i) deep global p-bound minima with relatively large barriers for internal rotation (associated with large harmonic bending frequencies), (ii) a nearly isotropic potential in the azimuthal coordinate and (iii) strong angular–radial coupling effects. The zero-point effects associated with this type of PES cause large deviations between the properties of the equilibrium and ground state structures and have profound effects on the interpretation of the spectroscopic observables [55, 56, 118].

Initially, the large discrepancies observed between the calculated equilibrium separation of the intermolecular C–Rg bond (R_e) and the vibrationally averaged value in the ground vibrational state derived from the rotational constants (R_{cm}) have been the first signs of significant non-rigidity, large zero-point effects and strong angular–radial couplings in the PESs of the CH_3^+–Rg dimers [54–56]. The discrepancies decrease with increasing interaction energy ($R_{cm} - R_e = 0.34$, 0.17 and 0.10 Å for He, Ne and Ar), implying that the effects are more pronounced for the more floppy complexes. The following reasons have been considered to rationalize the large difference between R_e and R_{cm}: (1) neglect of monomer relaxation in the determination of R_{cm}; (2) insufficient level of theory employed for the calculation of the PES (and R_e); (3) large zero-point effects arising from anharmonicity along the intermolecular stretching and bending coordinate; (4) large angular–radial coupling. All four possibilities have systematically been tested to investigate their contribution to $R_{cm} - R_e$.

First, the influence of monomer relaxation on R_{cm} is considered. As outlined before, the neglect of CH_3^+ deformation (estimated from the *ab initio* calculations) leads to errors in R_{cm} of the order of $R_{cm} - R_{C-Rg} < 0.008$, 0.005 and 0.04 Å for He, Ne and Ar respectively [54–56]. These effects are much smaller than the observed differences and increase with the interaction strength, in disagreement with the experimental trend. Hence, neglect of monomer deformation is not a crucial factor for the determination of the geometry of the intermolecular bond. This conclusion is also supported by the rovibrational calculations discussed below [118].

Second, the quality of the PESs calculated at the MP2/aug-cc-pVTZ$^{\#}$ level is tested by calculations using both higher theoretical levels (MP4) and larger basis

Table 8. Energetic and structural properties of the p-bound equilibrium structure of CH_3^+–He (C_{3v}) calculated at different levels of theory [55].

Level	D_e (cm^{-1})	E_2 (cm^{-1})	R_e (Å)	θ_e	r_e (Å)
MP2/aug-cc-pVTZ$^{\#}$ (relaxed)	707	55	1.8337	91.4°	1.0829
MP2/aug-cc-pVTZ$^{\#}$ (rigid)	675		1.9049	90°	1.0844
MP4/aug-cc-pVTZ$^{\#}$ (rigid)	727		1.8897	90°	1.0877
MP2/aug-cc-pVQZ (rigid)	712		1.8939	90°	1.0827

sets (aug-cc-pVQZ). As an example, table 8 compares the data obtained for the equilibrium structure of CH_3^+–He [55]. All levels agree in R_e to within 0.07 Å, which is much smaller than the observed difference, $R_{cm}-R_e = 0.34$ Å. Additional calculations for CH_3^+–Ne show that the MP2/aug-cc-pVTZ$^{\#}$ level recovers 88% of the MP2 interaction at the basis set limit, $D_e = 1150\,cm^{-1}$ [118]. Consequently, the MP2/aug-cc-pVTZ$^{\#}$ level is concluded to provide a satisfactory approximation to the true interaction energy for both CH_3^+–He and CH_3^+–Ne.

In a third step, selected cuts through the 3D PES are considered to estimate the zero-point effects of anharmonicity along both the intermolecular stretching and the bending coordinates. For the radial motion, eigenvalues and eigenfunctions have been determined by solving the 1D Schrödinger equation using the radial potential cuts of the relaxed PES (figure 9(*d*)) and treating CH_3^+–Rg as a diatomic. In the case of CH_3^+–He [55], anharmonicity reduces the harmonic wavenumber, $\omega_s = 205\,cm^{-1}$ (unscaled), to $\nu_s = 175\,cm^{-1}$ and causes the R_{cm} value in the ground state to be 0.05 Å longer than at the equilibrium (i.e. $R_{cm}-R_e = 0.05$ Å). In the case of CH_3^+–Ne [56], the corresponding data are $\omega_s = 171\,cm^{-1}$, $\nu_s = 161\,cm^{-1}$ and $R_{cm}-R_e \approx 0.02$ Å. Thus, the radial motion provides only a small contribution to the values observed for $R_{cm} - R_e$. To investigate the influence of the bending vibration, the rigid monomer PES in figure 10 is considered. In the two-dimensional (2D) harmonic oscillator approximation, the (unscaled) *ab initio* harmonic bending frequencies of $\omega_b/cm^{-1} = 604$ (He) and 496 (Ne) correspond to an averaged value of $\langle\gamma^2\rangle^{1/2} = 11°$ for both dimers. According to the PESs in figure 10, the minimum separations for $\gamma = 10°$ occur at R_{min} values (2.07 and 2.29 Å) which are much closer to the observed R_{cm} values (2.18 and 2.30 Å) than the corresponding R_e values (1.83 and 2.13 Å). These results imply that it is mainly the zero-point motion of the bending vibration which, via strong angular–radial coupling, gives rise to the large differences between R_e and R_{cm}. Even small angular excursions away from the p-bound equilibrium lead to large changes in R_{min}. This behaviour is typical for p-bound disk-and-ball systems, such as the CH_3^+–Rg dimers.

In order to evaluate quantitatively the effects of strong angular–radial coupling in disk-and-ball systems, the spectroscopic constants of the 3D PESs of CH_3^+–He and CH_3^+–Ne have been evaluated in their intramolecular ground vibrational states [118]. Eigenvalues and eigenfunctions of both dimers have been calculated by accurately solving the 1D, 2D and 3D rotation–intermolecular vibration Schrödinger equation for the 3D rigid monomer PES. For this purpose, analytical representations of both PESs with D_{3h} symmetry have been constructed from 307 (He) and 184 (Ne) symmetry-unique *ab initio* points with an accuracy of $< 1\,cm^{-1}$ (fit 1 in [118]). The determined spectroscopic constants include the dissociation energy (D_0), potential barriers (V_b), the lowest intermolecular vibrational levels and their wavefunctions

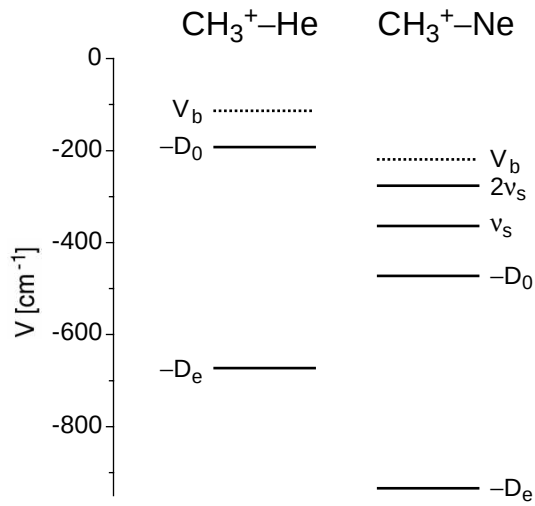

Figure 15. Vibrational energy level scheme for CH_3^+–He and CH_3^+–Ne derived from 3D rovibrational calculations on the rigid monomer PESs calculated at the MP2/aug-cc-pVTZ# level [118]. The well depth (D_e), the zero-point level (D_0), the barrier for inversion (V_b) and all vibrational levels below the barrier are included.

Table 9. Spectroscopic properties of CH_3^+–He and CH_3^+–Ne obtained by IRPD spectroscopy compared with equilibrium data and rovibrational calculations (1D and 3D) [55, 56, 118].

	CH_3^+–He				CH_3^+–Ne			
	Ab initio[a]	1D	3D	Experiment	*Ab initio*[a]	1D	3D	Experiment
D_e (cm^{-1})	707	672	672		959	935	935	
D_0 (cm^{-1})		570	193			853	474	
ω_s (cm^{-1})	205	214	124	113(4)	171	169	124	132(22)
ν_s (cm^{-1})	193	180	84[b]		162	152	106[b]	
ω_b (cm^{-1})	604				496			
ν_b (cm^{-1})	570		138[b]		468		272[b]	
A (cm^{-1})	4.7579	4.7414	4.9793	4.2747(62)[c]	4.7611	4.7414	4.9039	4.2564(68)[c]
B (cm^{-1})	1.3526	1.1847	0.8940	1.0053(19)	0.4106	0.3760	0.3325	0.35 720(92)
D_J ($10^{-4}\,cm^{-1}$)		1.565	2.621	2.82(18)		0.0822	0.1104	0.100(26)
D_{JK} ($10^{-4}\,cm^{-1}$)		−3.132	−3.959	−4.5(1.6)		−0.1643	−0.0540	0.56(27)
D_K ($10^{-4}\,cm^{-1}$)		1.5672	6.416	5.4(3.2)		0.0820	0.4447	5.6(3.6)

[a] Equilibrium data obtained by gradient optimization (tables 3 and 4).
[b] Average over both tunneling components.
[c] $A'' - \xi_3 A'$.

(including inversion tunneling) and the rotational and centrifugal distortion constants in the intermolecular ground state (figure 15, table 9). The D_0 values of CH_3^+–He are significantly lower than $D_e = 672\,cm^{-1}$ and decrease from 570 (1D) to 193 (3D) cm^{-1}. As expected for the large anisotropy of the disk-and-ball PES, the zero-point energy is dominated by the contributions of the bending mode (377 cm^{-1}), whereas the stretching component is less important (102 cm^{-1}). A

similar but less pronounced situation is observed for CH_3^+–Ne with $D_e = 935\,cm^{-1}$, and $D_0 = 853$ (1D) and 474 (3D) cm^{-1} respectively. In both complexes, the zero-point energy is large with respect to the well depth (71% and 49% for He and Ne, figure 15), which is perhaps surprising when compared with other complexes with similar interaction strengths (e.g. $D_e = 927\,cm^{-1}$ and $D_0 = 774\,cm^{-1}$ for NH_4^+–Ar [23, 149, 150]). The harmonic stretching frequencies calculated on the 3D PESs, $\omega_s/cm^{-1} = 124$ (He) and 124 (Ne), are in excellent agreement with those extracted from the experimental spectroscopic data (113 ± 4 and $132 \pm 22\,cm^{-1}$). The large decrease in ω_s on inclusion of the bending coordinates ($214 \rightarrow 124$ and $169 \rightarrow 124\,cm^{-1}$ for He and Ne) reflects the strong angular–radial coupling. The analogous effect on the bending vibration is even more pronounced: the anharmonic 3D wavenumbers, $\nu_b/cm^{-1} = 138$ (He) and 272 (Ne), are to be compared with the harmonic equilibrium values, $\omega_b/cm^{-1} = 604$ (He) and 496 (Ne). Contour plots of the vibrational wavefunctions confirm the strong stretch–bend coupling already for low excitation. In fact, the lowest bending levels of both complexes are already above the barrier for inversion (internal CH_3^+ rotation), $V_b/cm^{-1} = 555$ (He) and 715 (Ne), and feature significant free internal rotation character. The ground states are well below the inversion barriers (figure 15), resulting in tunnelling splittings ($< 0.007\,cm^{-1}$) which are well below the experimental resolution ($0.02\,cm^{-1}$). On the other hand, for the first bending level of CH_3^+–He (described by nearly free internal rotation), the tunnelling splitting amounts to $21\,cm^{-1}$. Again, the calculations demonstrate that the full 3D treatment is required for a correct description of the tunnelling dynamics in these weakly bound disk-and-ball dimers. Similarly, the comparison of the rotational and centrifugal distortion constants shows that inclusion of the bending motion is essential to obtain semiquantitative agreement with the spectroscopic parameters (table 9). This effect is particularly striking for the significant reduction of the B rotational constant of CH_3^+–He on inclusion of more dimensions; $B_e = 1.3526\,cm^{-1}$ and $B_0 = 1.1847$ (1D) and 0.8940 (3D) cm^{-1}. In general, the 3D calculations on the rigid monomer PESs yield spectroscopic constants and vibrationally averaged structures in semiquantitative agreement with experiment. The minor discrepancies are due to remaining deficiencies in the calculated PESs (the MP2/aug-cc-pVTZ$^{\#}$ level slightly underestimates the interaction) and the neglect of monomer deformation. As the relaxation of the intramolecular CH_3^+ coordinates in CH_3^+–He gives rise to a significant additional contribution to the binding energy (of up to 7% at the equilibrium, figure 11), future efforts to describe the interaction in this dimer with spectroscopic accuracy will require the determination of a nine-dimensional (9D) PES including all vibrational degrees of freedom. In particular, CH_3^+–He is an attractive system for such calculations because of its high symmetry, few degrees of freedom and small number of heavy atoms and electrons. For CH_3^+–Ar, the relaxation is even more important than for the He and Ne dimers and the rigid monomer approach is a rather poor approximation to the relaxed PES (figure 10, section 3.1.3). Hence, even for an approximate treatment of CH_3^+–Ar, at least the inversion coordinate has to be included explicitly.

The shape of the PESs of disk-and-ball dimers, such as p-bound CH_3^+–Rg, differs qualitatively from those of the well-characterized rod-and-ball and ball-and-ball dimers. For ball-and-ball dimers (e.g. NH_4^+–Rg [23] or HF–Ar [193]), the optimal intermolecular separation (R_{min}) does not strongly depend on the angular orientation (although the interaction energy D_{min} may do so). This is in contrast to linear rod-and-ball (e.g. N_2H^+–He [55] or NCH–Ar [194]) or p-bound disk-and-ball

dimers (e.g. CH_3^+–Rg, SO_3–Rg [195], C_6H_6–Rg [196–198]), for which R_{min} features a strong angular dependence resulting in strong angular–radial coupling. In linear rod-and-ball dimers, R_{min} decreases as the ligand is tilted away from the equilibrium separation, whereas the opposite behaviour is true for p-bound disk-and-ball dimers. Figure 16 compares the PESs of p-bound CH_3^+–He, linear N_2H^+–He and vertex-

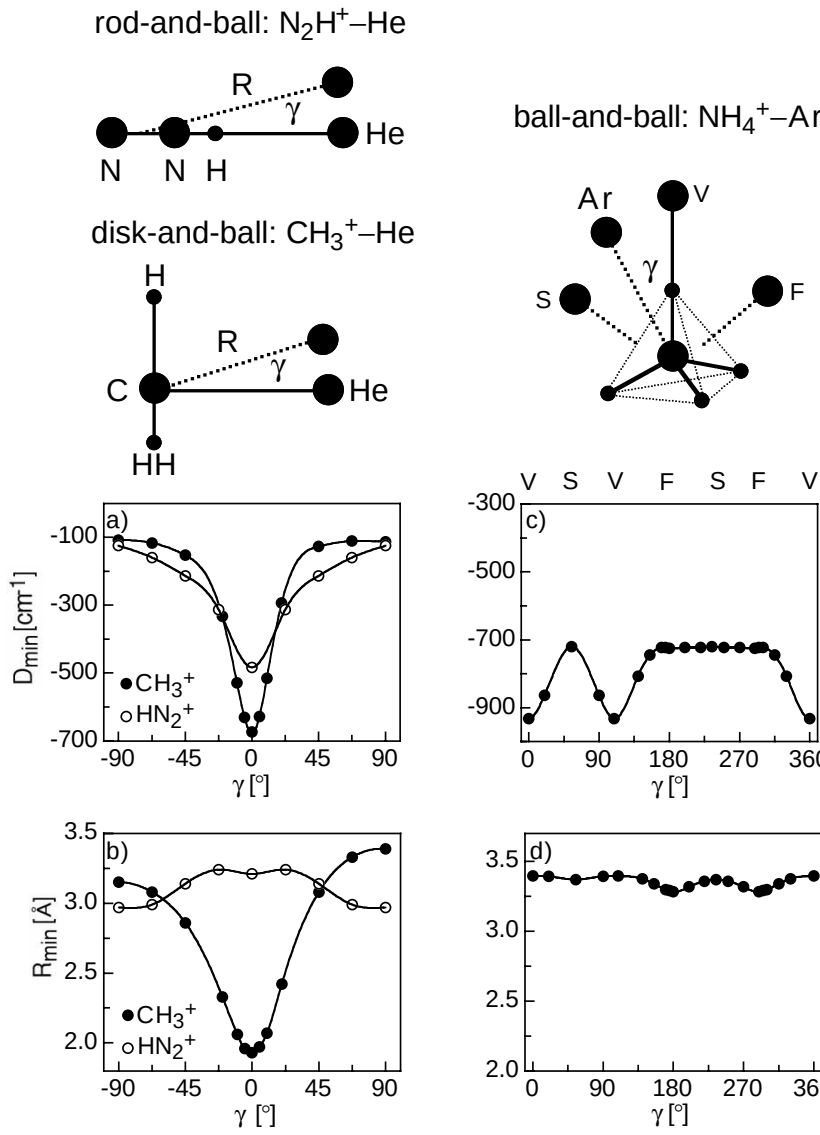

Figure 16. Selected properties of the intermolecular rigid monomer PESs of CH_3^+–He (representing a disk-and-ball dimer), N_2H^+–He (representing a rod-and-ball dimer) and NH_4^+–Ar (representing a ball-and-ball dimer) calculated at the MP2/aug-cc-pVTZ$^{\#}$ level [55, 150]. The potential energy depths (D_{min}) and minimal separations (R_{min}) of 1D radial cuts through the 3D PES are plotted as a function of the bending angle (γ). The positions V, S and F in the graphs (*c*) and (*d*) indicate vertex-, side- and face-bound orientations of NH_4^+–Ar. The ordinates in (*a*) and (*c*) as well as in (*b*) and (*d*) are drawn to the same scale.

bound NH_4^+–Ar calculated at the same level of theory to illustrate the differences for the three described classes of complexes for cation dimers with roughly the same interaction energy.

3.5. *Bonding mechanism in CH_3^+–Rg and reactivity of CH_3^+*

This section describes the mechanism for the formation of the intermolecular C–Rg bond in the CH_3^+–Rg dimers as a function of the interaction strength. In addition, comparison with the related NH_3^+–Rg and OH_3^+–Rg dimers will demonstrate that the Rg atom can be used as a sensitive probe of the reactivity of the $2p_z$ orbital of the central XH_3^+ cation as a function of its population.

Clearly, the long-range attraction of the intermolecular PES of all three CH_3^+–Rg dimers is dominated by induction forces, i.e. the interaction between the positive charge distributed over CH_3^+ and the polarizability of the Rg atom (mainly charge–induced dipole interaction). Dispersion forces play usually only a minor role in charged complexes involving Rg atoms [139]. As the Rg atom approaches the CH_3^+ ion along the C_3 symmetry axis, the formation of the intermolecular p bond is accompanied by partial electron transfer from the Rg atom into the vacant and electrophilic $2p_z$ orbital of C (figure 9(*c*)). Hence, it accepts electron density from the p-bound Rg atom which is acting as an electron donor. The charge transferred is small at the equilibrium geometries of CH_3^+–He and CH_3^+–Ne ($<0.04e$) but substantial for CH_3^+–Ar ($\sim 0.3e$). This observation suggests that charge transfer contributions to the interaction become more appreciable as the size of the Rg atom increases. Moreover, there appears to be a qualitative difference between He and Ne on the one hand and Ar on the other hand. In the case of the weakly bound He and Ne ligands ($D_0 = 193$ and $474\,cm^{-1}$), charge transfer is small and induction is dominant. For the strongly bound Ar ligand ($D_0 \sim 4000\,cm^{-1}$), electron transfer becomes important and the C–Ar bond features some covalent character. This qualitative difference is also mirrored in the complexation-induced CH_3^+ deformation in CH_3^+–Rg discussed in section 3.1.1 (figure 9). The magnitude of the deformation is strongly correlated to the amount of charge transfer. The planar CH_3^+ ion with sp^2 hybridization becomes pyramidal in CH_3^+–Rg, indicating the transformation toward sp^3 hybridization in the dimer. However, while the pyramidal angle θ_e is close to 90° for He and Ne (i.e. $\approx sp^2$), in CH_3^+–Ar it is $\sim 100°$ and halfway between sp^2 (90°) and sp^3 (109°) hybridization. The charge transfer is also reflected in the ν_3 frequencies of the larger CH_3^+–Ar_n clusters discussed in section 5.3. As efficient charge transfer requires significant overlap of the Rg ligand with the $2p_z$ orbital of C, the planar H-bound and side-bound CH_3^+–Rg structures are mainly stabilized by induction, implying that the bonding mechanism depends largely on the orientation

Thermochemical studies established that for many stable species the proton affinity (PA) is linearly correlated to the methyl cation affinity (MCA) [99]. This relation holds also for Kr and Xe, which form strong chemical bonds to both H^+ and CH_3^+ (table 10). However, for the smaller Rg atoms, the MCA drops faster than the PA (figure 17(*a*)). A similar trend is observed when the PA and MCA of the Rg atoms are plotted versus their ionisation energy, IE (figure 17(*b*), table 10). Apparently, the bonding mechanism in H^+–Rg and CH_3^+–Rg depends strongly on the size of the Rg atom. All Rg atoms form covalent bonds to a proton, with binding energies ranging from 178 (He) to 500 (Xe) kJ mol^{-1}. However, only Kr and Xe form strong and fully developed covalent bonds to CH_3^+ (200 and 231 kJ mol^{-1}). The

Table 10. Selected properties of Rg atoms.

	He	Ne	Ar	Kr	Xe
MCA (kJ mol^{-1})[a]	2.3	5.7	47.3	200	231
PA (kJ mol^{-1})[b]	177.8	198.8	369.2	426.6	499.6
α_{Rg} ($4\pi\varepsilon_0$Å^3)[c]	0.20	0.39	1.63	2.48	4.0
IE (eV)[d]	24.48	21.56	15.76	14.00	12.13

[a] References [99, 102]. The values for He and Ne are approximated by the D_0 values of their complexes with CH_3^+ (table 9).
[b] Reference [106].
[c] References [199, 200].
[d] Reference [201].

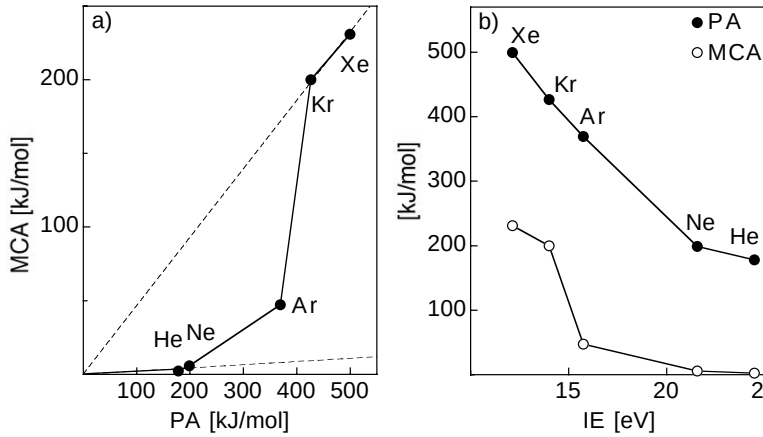

Figure 17. (*a*) MCA of Rg atoms versus their PA. The broken lines correspond to linear extrapolations from the He/Ne and Kr/Xe data alone. (*b*) MCA and PA of Rg atoms versus their ionization energy (IE). The data are taken from table 10.

intermolecular bonds from CH_3^+ to He and Ne are very weak and predominantly based on induction (2.3 and 5.7 kJ mol^{-1}), mainly because the high IE of He and Ne prevent efficient charge transfer to CH_3^+. The CH_3^+–Ar dimer (47.3 kJ mol^{-1}) is an intermediate case, where partial charge transfer indicates the onset of covalent bonding.

It is illustrative to compare the properties of the intermolecular CH_3^+–Rg bonds (Rg = He, Ne, Ar, Kr, Xe) with those of the fully developed covalent bonds in neutral isoelectronic CH_3–X molecules with sp^3 hybridization (X = H, F, Cl, Br, I). Figure 18 shows the following properties of the C–Rg and C–X bonds (table 11) as a function of the size of Rg/X: (a) interatomic C–Rg/X separation R_e, (b) H–C–Rg/X bond angle θ_e and (c) C–Rg/X bond energy D_0. Clearly, for increasing Rg size, all properties of the CH_3^+–Rg bonds converge toward those of the corresponding CH_3–X bonds, confirming the conclusion that covalent contributions to the C–Rg bonds become important for the larger Rg atoms.

The comparison between the related XH_3^+–Ar dimers with X = C [54], N [121, 122] and O [121, 123] reveals the effect of the number of electrons in the $2p_z$ orbital of X in the (quasi-)planar XH_3^+ ions on the interaction potential. All three dimers have been studied by rotationally resolved IRPD spectroscopy and quantum chemical

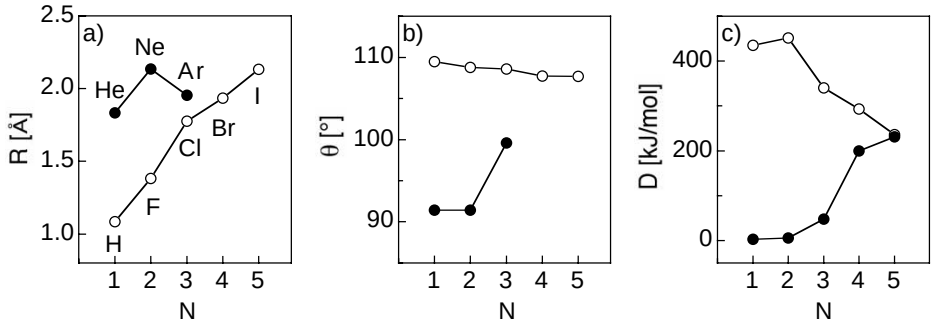

Figure 18. Comparison of the properties of the C–Rg intermolecular bonds in ionic CH_3^+–Rg complexes with those of the chemical C–X bonds in the isoelectronic neutral CH_3–X molecules: (*a*) C–Rg/X separation (R_e); (*b*) H–C–Rg/X bond angle (θ_e); (*c*) C–Rg/X bond energy (D_0). $N = 1$–5 correspond to Rg/X = He/H, Ne/F, Ar/Cl, Kr/Br and Xe/I respectively. The data are taken from tables 3, 10 and 11.

Table 11. Geometric parameters and dissociation energies of the C–X bonds in neutral CH_3X molecules.

	CH_4	CH_3F	CH_3Cl	CH_3Br	CH_3I
θ_e [a]	109.47°	108.80°	108.58°	107.73°	107.68°
R_e(C–X) (Å)[a]	1.086	1.383	1.776	1.934	2.132
D(C–X) (kJ mol^{-1})[b]	435	452	340	293	236

[a] References [202, 203].
[b] References [188, 201].

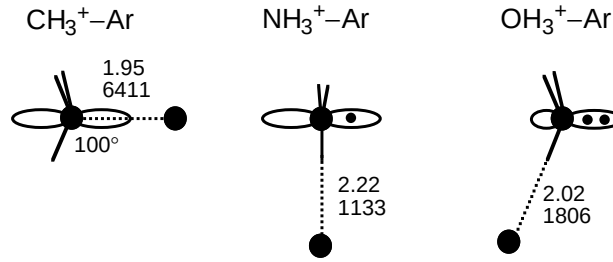

Figure 19. Structures of the most stable XH_3^+–Ar dimers with X = C, N and O, calculated at the MP2/aug-cc-pVTZ$^{\#}$ level. Electrons in the $2p_z$ orbital of the central X atom are indicated by full circles. Intermolecular bond lengths and dissociation energies are given in Å and cm^{-1} respectively (table 12).

calculations at the same theoretical level. The properties of their equilibrium structures are shown in figure 19 (table 12). In CH_3^+–Ar, significant charge transfer from Ar to the vacant electrophilic $2p_z$ orbital of C results in a strongly p-bound equilibrium structure. This partial electron transfer greatly reduces the electrophilic character of the $2p_z$ orbital. The $2p_z$ orbital of planar NH_3^+ is occupied by one electron and has little electrophilic character. Consequently, it does not accept electron density from Ar and NH_3^+–Ar adopts an H-bound equilibrium structure [121, 122]. The $2p_z$ orbital of OH_3^+ is filled and thus even less electrophilic than in NH_3^+. Hence, the p-bound OH_3^+–Ar structure is far less stable than the H-bound

Table 12. Properties of the intermolecular bonds in XH_3^+–Ar dimers (X = C, N, O) calculated at the MP2/aug-cc-pVTZ$^{\#}$ level [121].

	Isomer	Nature [a]	D_e (cm^{-1})	R_e (Å)
CH_3^+–Ar	H-bound	LM	678	2.43
	p-bound	GM	6411	1.95
NH_3^+–Ar	H-bound	GM	1133	2.22
	p-bound	LM	866	2.95
OH_3^+–Ar	H-bound	GM	1806	2.02
	p-bound	TS	785	3.22

[a] Nature of stationary point: LM, local minimum; GM, global minimum; TS, transition state.

global minimum [121, 123]. In general, increasing the population of the $2p_z$ orbital in XH_3^+ from zero to two electrons leads to a destabilization of the p-bound H_3X^+–Ar structures ($D_e = 6411$, 866, 785 cm^{-1} for X = C, N, O) because of the reduction of charge transfer and the increase in Pauli exchange repulsion. On the other hand, the H-bound H_2XH^+–Ar minima are stabilized ($D_e = 678$, 1133, 1806 cm^{-1} for X = C, N, O). The latter trend is compatible with the decrease in the PA within the series $H_2C > H_2N > H_2O$ (837 > 773 > 691 kJ mol^{-1}). The comparison of the XH_3^+–Ar dimer series nicely demonstrates that an Ar ligand can be used as an extremely sensitive probe of both the reactivity of distinct orbitals in molecular ions and the acidities of protons.

3.6. *Comparison with related systems*

The synthesis of Rg-containing neutral molecules continues to fascinate the chemist [204–207]. The p-bound CH_3^+–Ar dimer is an example for a complex with a rather strong bond between Ar and a closed-shell polyatomic ion (~ 0.5 eV), and its spectrum is presumably the first unambiguous experimental evidence for such a chemical C–Ar bond [54]. Similar but somewhat weaker p bonds between an ion and an Rg atom have recently been calculated for the related SiF_3^+–Rg dimers (Rg = Ar, Kr, Xe) [208]. Spectroscopic data for CH_3^+–L dimers with closed-shell molecules are rather scarce [1, 209, 210]. However, theoretical and mass spectrometric studies suggest that these complexes have fully developed covalent C–L bonds with sp^3 hybridization on C (e.g. L = CO, N_2, etc.) [16, 51, 81, 91, 93, 104, 105]. An interesting exception is the extremely floppy CH_3^+–H_2 ($= CH_5^+$) molecular ion, whose T-shaped equilibrium structure is characterized by a non-classical three-centre two-electron bond [1, 209, 211–213]. However, all protons are equivalent in the ground vibrational state of CH_5^+, because of rapid proton scrambling via very low barriers for several internal motions.

Nearly all of the AH^+–Rg dimers previously characterized by high-resolution spectroscopy have H-bound equilibrium structures [1]. In these proton-bound dimers, the strength of the intermolecular bond is inversely related to the difference in the PAs of the two bases, A and Rg [1, 133, 214]. As the PA of CH_2 is much higher than those of the Rg atoms [106], the CH_3^+ cation is an extremely weak proton donor [89, 104] and the H-bonded H_2CH^+–Rg structures have low dissociation energies (table 3). Both experiment and theory demonstrate that these structures are only shallow local minima on the PES, whereas the p-bound H_3C^+–Rg structures are much more stable and deep global minima [54–56, 89]. Theoretical studies demon-

strated that even strong H bonds in AH^+–Rg dimers are dominated by induction attraction [139]. This is in contrast to the significant contributions of charge transfer in the strongly p-bound H_3C^+–Rg dimers. Similar charge transfer contributions have also been reported for the p-bound H_2O^+–Ar structure (which is, however, only a local minimum on the PES) [139].

The magnitude of the angular anisotropy in AH_k^+–Rg dimers can vary drastically from complex to complex. For example, the intermolecular interaction in linear H-bound AH^+–Rg dimers (rod-and-ball) is quite directional with large barriers for internal rotation and relatively small zero-point angular excursions. Examples include AH^+–Rg dimers with $AH^+ = HCO^+$ [124–126, 128, 215–218], HN_2^+ [128–131, 218, 219], $SiOH^+$ [128, 132, 133], OH^+ [137, 138], O_2H^+ [136] and $OCOH^+$ [135]. H-bound AH_k^+–Rg complexes with $k \geq 2$ feature k equivalent minima with non-vanishing probability for exchange tunnelling [1]. In general, the (nearly) linear H bonds are less directional and the tunnelling probability increases with decreasing interaction strength and increasing k [1]. Illustrative examples for AH_2^+–Rg include Rg dimers of ClH_2^+ [134], H_2O^+ [139–142] and NH_2^+ [143–145]. Planar H-bound AH_3^+–Rg dimers are disk-and-ball dimers, similar to the p-bound CH_3^+–Rg dimers (section 3.4). However, the shapes of the potentials of both classes of disk-and-ball dimers are rather different, giving rise to different angular–radial coupling effects. Examples of H-bound AH_3^+–Rg dimers include complexes with NH_3^+ [121, 122], H_3O^+ [121, 123] and H_3^+ [174, 220–224]. AH_4^+–Rg (e.g. NH_4^+–Rg [23, 146–150]) and AH_5^+–Rg (e.g. CH_5^+–Rg [225]) complexes are model systems for ball-and-ball dimers and have rather isotropic potentials with low internal rotation barriers.

It is illustrative to compare the CH_3^+–Rg properties with those of the corresponding neutral dimers to demonstrate the rather dramatic effect of ionization on the PES. However, experimental data for CH_3–Rg radical dimers are not available and theoretical information is rather sparse [120]. The binding energy of CH_3–Ar is calculated as $0.17\,kcal\,mol^{-1}$ and is about 2 orders of magnitude lower than that of the cation [120]. Although intermolecular bonds in both closed-shell and open-shell dimers may show the onset of incipient chemical bonding [226–229], the dominant attraction in CH_3–Ar appears to arise from dispersion forces. This is in contrast to CH_3^+–Rg, which are stabilized by induction and partial electron transfer. The rather different PESs of CH_3^+–Rg and CH_3–Rg will lead to interesting photoionization dynamics. Finally, it is noted that the CH_3 radical was found to form a linear H bond to halide anions, such as I^- [230].

4. CH_3^+–Rg_2 trimers

4.1. *Potential energy surface*

4.1.1. *Stationary points*

The PESs of CH_3^+–Rg_2 with Rg = He and Ne are considered first (tables 3 and 4) [55, 56]. The global minimum of both PESs corresponds to a symmetric geometry with two equivalent Rg atoms attached to opposite sides of the $2p_z$ orbital of C (figure 1(*f*), D_{3h}). The individual intermolecular p bonds in the trimers are slightly weaker than in the dimers, leading to somewhat longer C–Rg separations. For example, the data for CH_3^+–Ne and Ne–CH_3^+–Ne are $R_e = 2.135$ and 2.232 Å, $D_e = 959$ and $745\,cm^{-1}$ and $\nu_s = 162$ and $132\,cm^{-1}$ respectively. As the dissociation energies of both Rg ligands are similar, they cause nearly additive effects of

subsequent complexation on the C–H bond properties with respect to both bond shortening and the increase in the C–H stretch frequencies. For example, the data for CH_3^+–Ne and Ne–CH_3^+–Ne are $\Delta r_e = -0.0019$ and -0.0034 Å, $\Delta\nu_1 = 16.1$ and $28.4\,cm^{-1}$ and $\Delta\nu_3 = 16.6$ and $30.6\,cm^{-1}$. The influence of the second ligand on CH_3^+ is somewhat weaker than that of the first ligand, because non-cooperative three-body effects lower the average binding energy. This effect arises mainly from the fact that the CH_3^+–Rg dimers can lower their energy by a slight pyramidal deformation of CH_3^+ ($\theta_e = 91.4°$) This effect is not operative in the symmetric Rg–CH_3^+–Rg trimers with a planar central CH_3^+ ion ($\theta_e = 90°$). Because of the longer separations, the charge transfer in the trimers with He and Ne is even smaller than that in the corresponding dimers (table 7). In general, the trends observed for complexation with the second Rg ligand are similar for Ne and He, with the main difference that the effects are larger in the former system because of the stronger interaction. On the basis of the dimer potentials, several local minima are expected on the CH_3^+–Rg_2 PESs, such as one with one p bond and one H bond or one with two H bonds. However, as these have much lower binding energies than the global minimum (with two p bonds), they are not observed experimentally and will not be considered further here.

The topology of the CH_3^+–Ar_2 PES differs qualitatively from those involving the smaller Rg atoms (tables 3 and 4) [54]. The global minimum of the CH_3^+–Ar_2 PES has an asymmetric Ar–CH_3^+–Ar geometry with two non-equivalent Ar atoms attached to either side of the $2p_z$ orbital of C (figure 1(*e*), C_{3v}). One C–Ar bond is short and strong ($R_{1e} = 2.04$ Å, $\nu_s = 288\,cm^{-1}$), whereas the second one is long and weak ($R_{2e} = 2.88$ Å, $\nu_s = 75\,cm^{-1}$). The dissociation energy for the second Ar ligand is only $768\,cm^{-1}$, which is roughly one order of magnitude smaller than the bond strength to the first ligand ($6411\,cm^{-1}$). Hence, this trimer structure is best described by a strongly bound pyramidal CH_3^+–Ar core, which is weakly perturbed by the second ligand. In fact, complexation with the second Ar causes the first C–Ar bond to become somewhat weaker ($R_{(1)e} = 2.04$ versus 1.95 Å, $\nu_s = 288$ versus $387\,cm^{-1}$) and, as a result of the decreased charge transfer (0.18*e* versus 0.3*e*) the large CH_3^+ deformation induced by the first ligand is slightly reduced (e.g. $\theta_e = 97.5°$ versus 99.6°). The second Ar donates only little charge to the $2p_z$ orbital, implying that this weak bond is mainly based on induction. The symmetric Ar–CH_3^+–Ar structure with two equivalent Ar atoms (figure 1(*f*), D_{3h}) is a transition state with a barrier of $V_b \approx 550\,cm^{-1}$ for interconversion between the two equivalent C_{3v} structures. Both intermolecular bonds are weak ($R_e = 2.37$ Å, $D_e = 222\,cm^{-1}$, $\nu_s = 138\,cm^{-1}$) and predominantly based on induction ($\Delta Q = 0.03e$). The low barrier for the umbrella inversion tunnelling motion is associated with an imaginary frequency of $159i\,cm^{-1}$ for the antisymmetric intermolecular C–Ar stretch. Similarly to CH_3^+–Rg_2 with Rg = He and Ne, several less stable local minima are predicted on the CH_3^+–Ar_2 PES [120] but not considered further because they are not identified experimentally [54].

Apparently, the strength of the CH_3^+–Rg dimer interaction determines the symmetry of the Rg–CH_3^+–Rg trimer equilibrium structures. For weak dimer interactions (Rg = He, Ne), the pyramidal CH_3^+ deformation is small and the trimer structures have D_{3h} symmetry [55, 56]. As the dimer interaction becomes stronger (Rg = Ar), the pyramidal deformation increases and the trimer geometries are asymmetric (C_{3v}) [54, 120]. It would be interesting to see whether this trend in the change of the topology of the PES as a function of the interaction strength is

confirmed for the Rg atoms Kr and Xe (neither experimental nor theoretical data are available for these trimers). As a consequence of the preceding discussion, the symmetry of the global minimum structure predicted for Ar–CH_3^+–Ar (C_{3v} or D_{3h}) depends sensitively on the quality of the employed calculations [54]. At low theoretical levels (e.g. at the HF level [54] or the MP2 level using the 6-311G basis [102]), the interaction of CH_3^+ with the first Ar ligand and the resulting pyramidal deformation is largely underestimated. Consequently, these levels erroneously predict the D_{3h} structure of Ar–CH_3^+–Ar to be the most stable trimer structure. On the other hand, the C_{3v} structure of Ar–CH_3^+–Ar is correctly obtained as a global minimum at higher theoretical levels [54, 120]. The example of Ar–CH_3^+–Ar emphasizes again the importance of monomer deformation on the properties of cluster cations and the deficiencies of rigid monomer treatments (section 3.1.3).

4.1.2. *Non-additivity*

An interesting aspect of the interaction in charged complexes is the contribution of three-body potential terms [1, 24, 231], which are often stronger than those observed in neutral clusters [197, 232]. In the absence of (additive) electrostatic interactions, the main contribution to non-additive terms in the attractive part of the p-bound Rg–CH_3^+–Rg PES with Rg = He and Ne arises from the strongly non-additive induction forces (mainly charge–induced dipole) [24]. These are mainly non-cooperative because of the repulsive interaction between the two dipoles induced in the two Rg atoms. Similar weak but noticeable non-cooperative three-body effects have previously been reported for related cation and anion complexes involving Rg atoms [121, 122, 126, 128, 132, 139, 140, 147, 179, 231, 233].

In the case of p-bound Ar–CH_3^+–Ar, the non-additivity is particularly striking because of the significance of charge transfer and the resulting monomer deformation involved in the formation of the first p bond. Complexation with the second ligand has a strong effect on the properties of the bond to the first ligand, reducing the charge transfer, the degree of monomer deformation and the bond strength [54]. Although both Ar ligands bind to the $2p_z$ orbital of C, their interaction energies differ by about 1 order of magnitude because the origin of both bonds is rather different (charge transfer versus induction) [54, 102, 120].

4.2. *IR spectra*

Figure 20 compares the IRPD spectra of CH_3^+–Ar_2 and CH_3^+–Ne_2 recorded in the vicinity of the ν_3 fundamental of CH_3^+ [54, 56]. Both spectra display a single vibrational transition, and the analysis of its rovibrational structure is consistent with an assignment to the ν_3 fundamental of a Rg–CH_3^+–Rg complex in which both Rg atoms form intermolecular p bonds to CH_3^+. The spectrum of the ν_3 fundamental of CH_3^+–Ar_2 could be recorded in the CH_3^+–Ar channel because of the low binding energy of the second ligand ($\sim 800\,cm^{-1}$ [54, 102, 120]). The corresponding CH_3^+–Ne_2 spectrum is obtained in the CH_3^+ channel, as the ν_3 frequency is sufficient to cleave both p bonds of this trimer ($\sim 1000\,cm^{-1}$). Significantly, both spectra are fully rotationally resolved, providing the first high-resolution spectroscopic data for the structure of cation trimers. Unfortunately, the achieved ion currents of CH_3^+–He_2 were too low to record its IRPD spectrum.

The CH_3^+–Ne_2 spectrum is considered first [56]. The ν_3 spectrum has the rotational structure appropriate for a perpendicular transition of a prolate symmetric top. The large spacing of neighbouring $\Delta K = \pm 1$ Q branches of $\sim 8\,cm^{-1}$

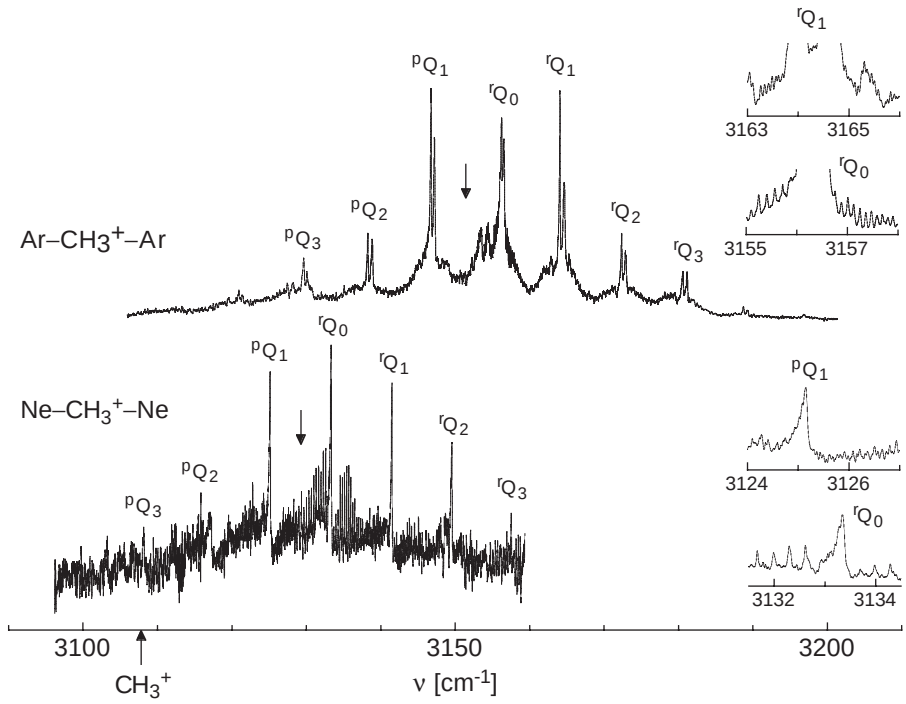

Figure 20. IRPD spectra of Rg–CH_3^+–Rg (Rg = Ne and Ar) in the range of the ν_3 fundamental recorded in the CH_3^+–Ar and CH_3^+ fragment channels respectively [54, 56]. The transitions have the rotational structure appropriate for a prolate symmetric top. The Q branches of the $\Delta K = K' - K'' = \pm 1$ subbands are given in the notation ${}^{\Delta K}Q_K$. The arrows indicate the positions of the ν_3 band origins. The insets show that the spacing between adjacent P and R branch lines of the $K = 1 \leftarrow 0$ subbands is twice that of other subbands. The inversion tunnelling splitting in the CH_3^+–Ar_2 spectrum shows that the complex has an equilibrium structure with C_{3v} symmetry (figure 1(*e*)). The absence of such a splitting in the CH_3^+–Ne_2 spectrum is consistent with a geometry with D_{3h} symmetry (figure 1(*f*)).

confirms that both Ne atoms are located on the C_3 axis of CH_3^+. The Q branches originating from $K = 3n$ levels are enhanced owing to the nuclear spin statistical weights for a complex with three equivalent protons. Moreover, the P and R branches of the $K = 1 \leftarrow 0$ subband lack every second line, indicating that even J levels in the $K = 0$ state have a nuclear spin statistical weight of zero. The complex has therefore a vibrationally averaged structure with inversion symmetry. This result is in line with the calculated equilibrium structure with D_{3h} symmetry, featuring two equivalent Ne atoms. The molecular constants derived from fitting 109 rotational lines to the Hamiltonian (3) are listed in table 5. Figure 21 compares a selected part of the CH_3^+–Ne_2 spectrum with a simulation using a rotational temperature of 30 K.

Similarly to CH_3^+–Ne_2, the CH_3^+–Ar_2 spectrum has the rotational structure of a prolate symmetric top with threefold rotational symmetry [54]. However, all Q branches appear as doublets split by $0.50 \pm 0.08\,\mathrm{cm}^{-1}$. Such a splitting is not observed for CH_3^+–Ne_2 or any of the CH_3^+–Rg dimers. It is attributed to an inversion tunnelling motion between the two equivalent C_{3v} structures of Ar–CH_3^+–Ar via the

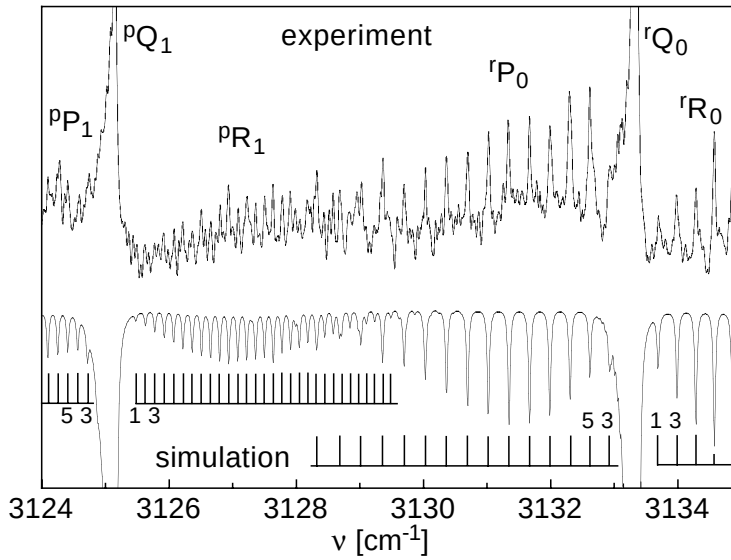

Figure 21. Expanded view of the IRPD spectrum of CH_3^+–Ne_2 compared with a simulation using the molecular constants in table 5, a convolution width of $0.04\,cm^{-1}$ and a rotational temperature of $T_{rot} = 30$ K [56]. The spacing between adjacent $^rP_0$ and $^rR_0$ lines is twice that of the other subbands.

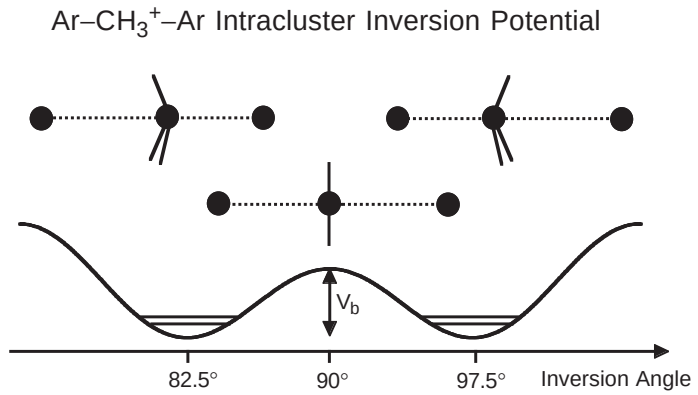

Figure 22. Double minimum potential for the intracluster inversion motion in Ar–CH_3^+–Ar. The two equivalent minima correspond to structures with non-equivalent Ar atoms (C_{3v}, figure 1(*e*)), whereas the transition state (barrier V_b) has a symmetric structure (D_{3h}, figure 1(*f*)). The calculated barrier amounts to V_b $550\,cm^{-1}$ [54].

D_{3h} symmetric transition state (figure 22). This tunnelling motion is analogous to the NH_3 umbrella inversion discussed in many textbooks [234, 235] and splits all levels into two sublevels (inversion doublets), where the vibrational wavefunction is either symmetric (*s*) or antisymmetric (*a*) with respect to reflection at the origin. The selection rules for a perpendicular transition (such as the ν_3 fundamental) are $s \leftrightarrow s$ and $a \leftrightarrow a$. Hence, the observed tunnelling splitting of $0.5\,cm^{-1}$ corresponds to the difference in the tunnelling splittings in both vibrational states ($\Delta_3 - \Delta_0$). The relative positions and intensities of the *a* and *s* *Q* branches imply that the

splitting increases on ν_3 excitation (i.e. $\Delta_3 > \Delta_0$). Further information about the absolute magnitude of the splittings is provided by the ν_1 spectrum. The selection rules for the parallel ν_1 band are $s \leftrightarrow a$, i.e. the observed splitting amounts to $\Delta_1+\Delta_0$. The observed spectrum was rather poor, as for an inverting C_{3v} molecule the ν_1 transition becomes only weakly allowed through the inversion motion. Nonetheless, from the somewhat larger width of the unresolved ν_1 spectrum (overlapping $s \leftrightarrow a$ and $a \leftrightarrow s$ components), $\Delta_1+\Delta_0$ could be estimated as $< 14\,\mathrm{cm}^{-1}$. Under the reasonable assumption that the tunnelling splitting is nearly independent of ν_1 excitation [234], an upper limit of $\Delta_0 < 7\,\mathrm{cm}^{-1}$ could be derived. The tunnelling splitting Δ_0 can also be estimated from the relative intensities of the ν_3 $s \leftrightarrow s$ and $a \leftrightarrow a$ subbands (1.2 ± 0.1). Assuming that the population of the tunnelling components can be described by the same effective temperature derived from the population of the rotational levels (20–30 K), $\Delta_0 = 3.5 \pm 2\,\mathrm{cm}^{-1}$ is obtained. The inset in figure 20 shows that, similarly to CH_3^+–Ne_2, the spacing between adjacent P and R branch lines in the $K=1 \leftarrow 0$ subband is twice that of other subbands, confirming the inversion symmetry of this inverting C_{3v} symmetric complex. Although the accidental overlap of the lines with s and a inversion symmetry causes some line broadening, accurate rotational constants could be extracted from 28 lines of the $K=1 \leftarrow 0$ subband using a pseudodiatomic Hamiltonian (table 5). Finally, it is noted that three weak and unresolved C–H stretch overtone and combination transitions of CH_3^+–Ar_2 have been observed and assigned (table 1) [54].

4.3. *Structural, energetic and dynamical properties*

Similarly to CH_3^+–Rg, the rovibrational analysis of the CH_3^+–Rg_2 spectra (including vibrational frequencies and splittings, rotational constants, nuclear spin statistical weights) is fully consistent with p-bound Rg–CH_3^+–Rg equilibrium structures featuring two p bonds and three equivalent protons [54, 56]. In agreement with the high-level *ab initio* calculations [54, 56, 120], both Rg ligands are equivalent in Ne–CH_3^+–Ne (D_{3h}, figure 1(*f*)) but non-equivalent in Ar–CH_3^+–Ar (C_{3v}, figure 1(*e*)). All other isomeric structures can safely be excluded as a carrier of the observed spectra. Similarly to the dimers, the spectroscopic constants extracted from the trimer spectra can be used to derive important properties of the intermolecular p bonds in the ground and ν_3 vibrational states.

4.3.1. *Vibrational frequencies*

The sequential ν_3 frequency shifts provide the first quantitative experimental impression of the degree of non-additivity in Rg–CH_3^+–Rg. As predicted by the calculations, three-body interactions in Ne–CH_3^+–Ne are only slightly non-cooperative, resulting in nearly additive sequential ν_3 blue shifts of 11.5 and $10.5\,\mathrm{cm}^{-1}$ (table 7). Both Ne ligands are equivalent and interact only weakly through the separating CH_3^+ plane. Similar shielding is also observed for complexes of neutral aromatic molecules with two Rg atoms (e.g. Rg–C_6H_6–Rg [236–238]), which interact mainly via dispersion. The ν_3 blue shifts in Ne–CH_3^+–Ne demonstrate that complexation contracts the C–H bonds and vibrational excitation reduces the strengths of the p bonds (section 3.1.1).

Although the ν_3 wavenumber of CH_3^+–Ar is not known accurately, the value estimated from the sequence hot bands ($3145 \pm 30\,\mathrm{cm}^{-1}$) is close to those derived from a local mode analysis ($3132\,\mathrm{cm}^{-1}$) and the *ab initio* calculations ($3136\,\mathrm{cm}^{-1}$) [54]. The measured ν_3 wavenumber of Ar–CH_3^+–Ar ($3152\,\mathrm{cm}^{-1}$) is close to the dimer

value ($+7\,cm^{-1}$), indicating that the second Ar ligand is only weakly attached to the strongly bound dimer (featuring a ν_3 shift of $\sim 37\,cm^{-1}$). This strongly non-additive behaviour is in line with the rather different interaction of CH_3^+ with both Ar ligands. Both the experimental and the theoretical C–H stretch overtone and combination transitions of Ar–CH_3^+–Ar are all slightly larger than those of CH_3^+–Ar and confirm that the second Ar ligand stabilizes the C–H bonds further (table 1).

4.3.2. *Interpretation of rotational constants*

Assuming a D_{3h} structure for Ne–CH_3^+–Ne and undistorted CH_3^+, the vibrationally averaged intermolecular C–Ne bond length is derived as $R_{cm} = 2.344$ Å [56]. This value is significantly larger than the calculated equilibrium distance, $R_e = 2.232$ Å, mainly because of large angular–radial coupling (section 3.4). In general, both intermolecular p bonds in the trimer (and their effects on sequential complexation) are somewhat weaker than in the dimer, because the three-body interactions are slightly non-cooperative (table 7): $D_e/cm^{-1} = 959$ and 745, $R_{cm}/Å = 2.30$ and 2.34, $\Delta R_{cm}/Å = 0.008$ and 0.006, $R_e/Å = 2.13$ and 2.23, $(R_{cm} - R_e)/Å = 0.17$ and 0.11, $\Delta r_e/Å = -0.0019$ and -0.0015, $\Delta\nu_3^{calc}/cm^{-1} = 16.6$ and 14.0, $\Delta\nu_3^{exp}/cm^{-1} = 11.5$ and 9.9 for $n = 1$ and 2 respectively. In line with the blue shifts in ν_3, the interaction decreases on vibrational excitation, leading to weaker and longer intermolecular bonds (table 7).

The ground state B constant of Ar–CH_3^+–Ar corresponds to an Ar–Ar separation of $R_1 + R_2 = 4.84 \pm 0.02$ Å, nearly independent of the position of the pyramidal CH_3^+ unit on the C_3 axis and in close agreement with the calculated value (4.92 Å) [54]. The reasonable assumption that R_1 is not affected much on complexation with the weakly bound second ligand leads to $R_1 \sim 2.0$ Å and $R_2 \sim 2.8$ Å. The large disparity between R_1 and R_2 is consistent with the large difference in the dissociation energies ($D_0 \sim 4000$ and $800\,cm^{-1}$) and reflects the drastic non-cooperative three-body effect in this trimer.

4.3.3. *Predissociation dynamics*

Significantly, the ν_3 spectra of CH_3^+–Rg_2 in figure 20 exhibit rotational structure. In contrast, IRPD spectra of proton stretch vibrations of related AH^+–Rg_2 trimer cations do not show rotational substructure, because of homogeneous or inhomogeneous broadening [122, 125, 126, 128, 129, 131, 132, 140, 147, 225]. Homogeneous broadening may rise either from fast IVR and/or VP. Inhomogeneous broadening may originate from overlapping sequence transitions involving the soft, low-frequency intermolecular bending, stretching and torsional motions or contributions from less stable isomers. The CH_3^+–Rg_2 dimers feature relatively large rotational constants, low population of less stable isomers, relatively large intermolecular vibrational frequencies, high symmetry and weak coupling between the C–H stretch and intermolecular degrees of freedom, leading to little spectral congestion (inhomogeneous broadening) and slow relaxation processes (homogeneous broadening). The observed linewidths for CH_3^+–Rg_2 of 0.04 and $0.05\,cm^{-1}$ correspond to lower limits for the ν_3 lifetimes of $\tau_3 > 120$ and 100 ps for Rg = Ne and Ar respectively [54, 56].

4.4. *Rg–CH_3^+–Rg: model systems for S_N2 reactions*

As described by equation (1), complexes of the type L–CH_3^+–L may be considered as stabilized intermediates of cationic degenerate nucleophilic substitu-

tion (S_N2) reactions in the gas phase [81, 101]. In this bimolecular mechanism, a nucleophile attacks the electrophilic substrate from the backside and the reaction proceeds by a Walden inversion of the pyramidal CH_3 group and the departure of the leaving group [10, 239]. The details of the potential of this reaction depend strongly on the strength of the CH_3^+–L interaction and the degree of solvation. As an example, figure 22 shows the double minimum potential determined for the gas-phase reaction of Ar with CH_3^+–Ar:

$$\begin{aligned} \mathrm{Ar} + \mathrm{CH_3^+}\text{–}\mathrm{Ar} \leftrightarrow \mathrm{Ar}\cdots\mathrm{CH_3^+}\text{–}\mathrm{Ar} \leftrightarrow [\mathrm{Ar}\cdots\mathrm{CH_3}\cdots\mathrm{Ar}]^+ \leftrightarrow \mathrm{Ar}\cdots\mathrm{CH_3^+}\text{–}\mathrm{Ar} \\ \leftrightarrow \mathrm{Ar}\text{–}\mathrm{CH_3^+} + \mathrm{Ar}. \end{aligned} \tag{4a}$$

According to the calculations [54, 120] and the thermochemical data [102], the $Ar\cdots CH_3^+$–Ar complex (C_{3v}) is stabilized by $D_e \sim 800\,cm^{-1}$ with respect to the dissociation limit [54, 102, 120], and the barrier for intracluster inversion via the symmetric transition state (D_{3h}) amounts to $V_b \sim 550\,cm^{-1}$. These results are fully consistent with the tunnelling splitting of $\Delta_0 = 3.5 \pm 2\,cm^{-1}$ in the ground vibrational state, derived from the IR spectroscopic data (section 4.2) [54]. The tunnelling splittings estimated from the calculated double minimum potential solving a 1D Schrödinger equation are of the order of 0.1–5 cm^{-1} (depending on the details of the repulsive part of the potential), assuming a barrier of $V_b = 300$–$600\,cm^{-1}$ and an effective reduced mass of 12 u [54]. Closer inspection of the stationary points of C_{3v} and D_{3h} symmetry in the centre-of-mass system suggests that it is mainly the C atom that is moving during the tunnelling process (by 0.7 Å), whereas both the H and Ar atoms perform only small-amplitude motions. The large-amplitude motion of the heavy C atom through the barrier explains the small tunnelling splittings (despite the relatively small barrier). Significantly, the tunnelling motion observed for Ar–CH_3^+–Ar provides the first spectroscopic evidence that such S_N2 reactions proceed via a double minimum potential in the gas phase.

According to the calculations and the IR spectroscopic data, the most stable structures of Rg–CH_3^+–Rg with Rg = He and Ne have D_{3h} symmetry [55, 56]. Hence, the strength of the dimer interaction determines the symmetry of the trimer equilibrium structures. For weak dimer interactions (Rg = He, Ne), the angular CH_3^+ deformation is small, leading to a D_{3h} symmetric trimer structure. As the dimer interaction becomes stronger (Rg = Ar), the pyramidal deformation becomes larger, and the trimers feature asymmetric C_{3v} geometries. The change in the topology of the PES of Rg–CH_3^+–Rg as a function of the interaction strength is expected to continue with the heavier Rg atoms Kr and Xe because charge transfer becomes even more pronounced.

The partial electron transfer from the first Ar ligand to CH_3^+ greatly reduces the electrophilic character of the $2p_z$ orbital in the CH_3^+–Ar dimer. Consequently, the p bond to the second Ar ligand in the Ar–CH_3^+–Ar trimer is much weaker and longer than the p bond in the dimer and mainly based on induction interaction. Interestingly, calculations suggest that the most stable structure of CH_3^+–L_2 trimers with molecular ligands (e.g. L = CO) have both ligands on the same side of CH_3^+ [91]. Large electron transfer from the first ligand to CH_3^+ implies that most of the positive charge in CH_3^+–L is mainly localized on the first ligand and not on the CH_3 moiety. Hence, the electrostatic attraction of the second ligand by the first ligand is stronger than by the CH_3 moiety.

It is interesting to compare the properties of the cationic S_N2 reaction (4*a*) with those of the corresponding isoelectronic anionic variant which is also calculated to proceed via a double minimum potential [9, 10, 107–117]:

$$Cl^- + CH_3Cl \leftrightarrow Cl^- \cdots CH_3Cl \leftrightarrow [Cl \cdots CH_3 \cdots Cl]^- \leftrightarrow CH_3Cl \cdots Cl^- \leftrightarrow ClCH_3 + Cl^-. \quad (4b)$$

In general, both the attraction and the barrier of reaction (4*b*) are larger than for reaction (4*a*) because the electrostatic anion–dipole interaction is stronger than the cation–induced dipole attraction. For example, the dissociation energy of $Cl^- \cdots CH_3Cl$ is of the order of $10\,kcal\,mol^{-1}$ ($\sim 3600\,cm^{-1}$) and the barrier for inversion is about $3.5\,kcal\,mol^{-1}$ larger (i.e. $V_b \sim 4800\,cm^{-1}$) [116]. Finally, it is noted that the PES for reaction (4*b*) in aqueous solution is drastically different from that in the gas phase because of the strong anion–solvent (charge–dipole) interaction. The solution potential features a larger barrier and (nearly) no local minima for the ion–dipole complexes, because the relative energies of both the separated educts and products are lowered compared with those of the ion–dipole complexes by more efficient solvation [117].

5. Larger $CH_3^+ - Ar_n$ clusters ($n \leq 8$)

Theoretical [54, 102, 120], spectroscopic [54] and thermodynamic [102] data for $CH_3^+ - Rg_n$ clusters with $n \geq 3$ exist only for Rg = Ar. Moreover, the quality of available experimental and theoretical information on the geometric and energetic properties of $CH_3^+ - Ar_n$ ($n \leq 8$) decreases rapidly with increasing n because of the restrictions imposed by the limited spectral resolution and the feasible levels applied in quantum chemical calculations.

5.1. *Calculations*

5.1.1. *Structure of the first solvation shell*

The PES of the CH_3^+–Ar dimer shows that the optimal interaction between Ar and CH_3^+ is larger than $500\,cm^{-1}$ for any angular orientation (figure 10). On the other hand, the Ar–Ar interaction is only $\sim 100\,cm^{-1}$ [240]. Consequently, larger CH_3^+–Ar_n clusters are expected to have structures in which the CH_3^+ ion is solvated inside an Ar solvation shell (interior solvation), because the ion–ligand interaction exceeds by far the ligand–ligand attraction. This general view is supported by recent *ab initio* calculations conducted at various levels of theory, ranging from MP2/6-31+G(d,p) to QCISD(T)/6-311++G(2df,2pd) depending on the cluster size n [120]. These calculations suggest a cluster growth scenario for CH_3^+–Ar_n, in which the first eight Ar ligands occupy four distinct subshells within the first solvation shell. The first ligand forms a strong p bond to CH_3^+ (first subshell, $n = 1$), leading to a pyramidal CH_3^+–Ar charge transfer complex (section 3, figure 1(*b*)). The second Ar atom forms a weak p bond (second subshell, $n = 2$), resulting in an asymmetric CH_3^+–Ar_2 trimer (section 4, figure 1(*e*)). The barrier for inversion via the symmetric CH_3^+–Ar_2 transition state is of the order of 1–2 kcal mol^{-1} (figure 1(*f*)). Less stable trimer minima (such as the structure with one p bond and one H bond) are at least $1\,kcal\,mol^{-1}$ less stable than the global minimum with two p bonds. CH_3^+–Ar_n clusters in the size range $3 \leq n \leq 7$ have optimal structures in which a five-membered, (nearly) planar equatorial Ar solvation ring around an asymmetric Ar–CH_3^+–Ar trimer core is successively filled (third subshell). The ring is closer to the first

Ar atom, because of its larger positive charge (see figure 24 for $n=3$). The Ar positions within the ring are not well defined and are controlled by the subtle balance between the weak Ar–Ar dispersion attraction ($\sim 100\,cm^{-1}$), the small anisotropy of the CH_3^+–Ar dimer PES in this region ($\sim 80\,cm^{-1}$) and the repulsion between the dipoles induced in neighbouring Ar ligands (which provides a non-cooperative three-body contribution of $\sim 50\,cm^{-1}$ [126]). Apparently, the Ar–Ar attraction is the dominant factor [120] and favours asymmetric ring filling with a small increase in the average ligand binding energy as n increases. On the other hand, the Ar ligands are very fluxional for $n < 7$. For example, the barrier calculated for internal rotation of the third Ar atom around the trimer core is only 0.05 kcal mol^{-1} in the $n=3$ complex. In general, the number of less stable isomers grows rapidly as n increases. Clusters with $n > 7$ have structures in which the additional Ar ligands occupy a second equatorial ring (fourth subshell) around the Ar–CH_3^+–Ar nucleation centre. The second ring is staggered with respect to the first ring and closer to the second than the first Ar ligand. At present, it is not clear how many Ar ligands are required to complete the first solvation shell around the central CH_3^+ ion. By comparison with related A^+–Ar_n clusters with linear Ar–A^+–Ar nucleation centres and small closed-shell A^+ cations [126, 128], it may be speculated that the first solvation shell in CH_3^+–Ar_n is closed for $n=12$ by the formation of a slightly distorted, closed-packed icosahedral structure [241]. Although the calculations suggest that the Ar–CH_3^+–Ar nucleation centre in larger CH_3^+–Ar_n clusters has a pyramidal ion core [120], it is unclear at present how the inversion barrier ($\sim$1–2 kcal mol^{-1} for $n=2$) is affected by further solvation.

5.1.2. *Bonding mechanism*

The solvation shell structure is also reflected in the dissociation energies calculated for the most weakly bound ligands [120]: $D_0=15$ ($n=1$), 2.3 ($n=2$), 1.3–1.8 ($n=3$–7) and 1.4 ($n=8$) kcal mol^{-1} at the MP2/6–311++G(2df,2pd) level (table 13). The Mulliken population analysis at this level [120] shows that electron transfer from the first ligand to CH_3^+ is large and nearly independent of n (0.37e). In contrast, charge transfer is small for the $n=2$ ligand ($\sim 0.05e$) and decreases further for the higher subshells ($\sim 0.025e$ and $0.017e$ for $n=3$–7 and 8 respectively). The total positive charge on the CH_3^+ moiety decreases drastically from 1.0e to 0.63e

Table 13. Experimental and theoretical binding energies (in kcal mol^{-1}) of the most weakly bound ligand in CH_3^+–Ar_n.

n	D_0(calc)[a]	D_0(expt)[b]	$-\Delta H^0$(calc)[a]	$-\Delta H^0$(expt)[c]
1	15.09	12.94 ± 3.93	16.32	11.3 ± 2.0
2	2.28	< 3.0	2.27	2.26 ± 0.20
3	1.44	~ 2	1.32	1.97 ± 0.20
4	1.62	~ 2	1.47	1.96 ± 0.20
5	1.43	~ 2	1.21	1.94 ± 0.20
6	1.29	~ 2	1.13	1.94 ± 0.30
7	1.82	~ 2	1.63	1.94 ± 0.40
8	1.39	~ 2	1.32	~ 1.93

[a] MP2/6311++G(2df,2pd) level [120].
[b] From photofragmentation data [54].
[c] High-pressure mass spectrometry [102].

on complexation with the first ligand and then smoothly and monotonically down to 0.44*e* at $n=8$. A detailed decomposition of the interaction energy also reveals the change in the type of interaction as a function of the degree of solvation [120]. Large exchange repulsion in the dimer implies significant overlap of the electron densities of CH_3^+ and the first Ar ligand. This repulsion is compensated by significant attraction arising from electrostatic forces and delocalization, so that at the equilibrium geometry the self-consistent field (SCF) energy is of the order of 40% of the total interaction. In contrast, the bonds to further Ar ligands are dominated by correlation energies and the SCF contributions are minor.

5.2. *IR spectra*

Figure 23 reproduces the IRPD spectra of the ν_3 band of CH_3^+–Ar_n ($n=2$–8) recorded in the CH_3^+–Ar_m fragment channel (indicated as $n\rightarrow m$) [54]. The spectra of the $n\geq 3$ clusters show two principal changes. First, these clusters can shed more than one ligand on photoexcitation because the dissociation energies of the second and further ligands are much lower than that of the first ligand and the ν_3 frequency. Second, the rotational constants of the larger clusters are too small to yield fully rotationally resolved spectra at the laser resolution employed (0.02 cm^{-1}). Indeed, the ν_3 spectra are nearly structureless for $n\geq 4$. Despite the inferior quality of the larger-cluster spectra, the analysis of the size-dependent frequency shifts (figure 24) and the photofragmentation data provides useful information on the microsolvation process.

5.3. *Structures and dissociation energies*

In contrast to larger clusters, the ν_3 spectrum of the CH_3^+–Ar_3 tetramer exhibits several reproducible maxima, which are correlated with the *K* substructure of the corresponding CH_3^+–Ar_2 spectrum [54]. Two CH_3^+–Ar_3 structures may explain such a spectrum: a rigid structure with the third Ar atom lying also on the C_3 axis and a highly non-rigid structure in which the third Ar atom is occupying a position in a first solvation ring around the trimer core (figure 24). The first (chain-like) structure can be excluded by considering the induction energies of both structures

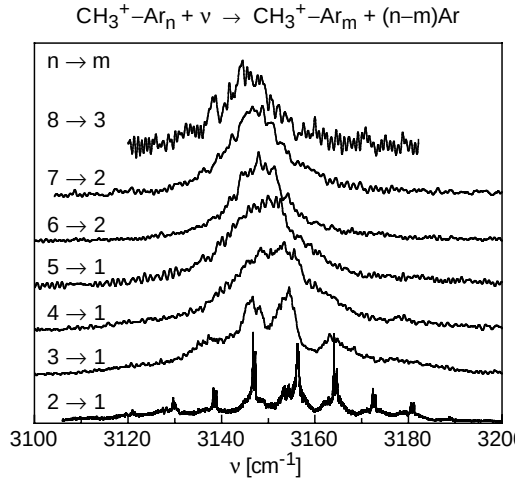

Figure 23. IRPD spectra of CH_3^+–Ar_n ($n=2$–8) in the range of the ν_3 fundamental recorded in the dominant CH_3^+–Ar_m fragment channel (indicated as $n\rightarrow m$) [54].

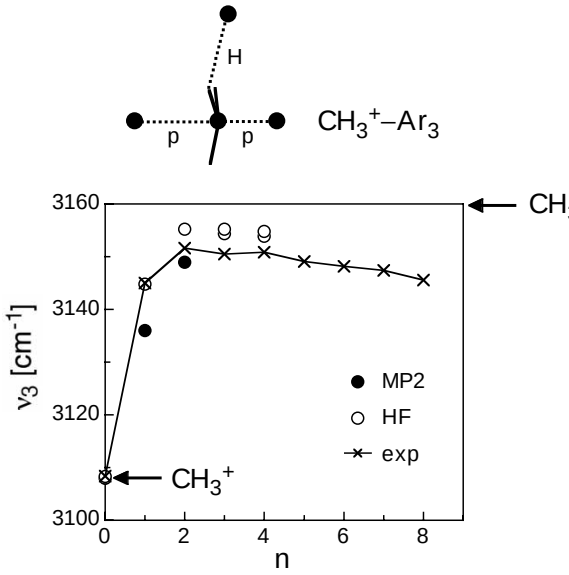

Figure 24. Experimental and calculated ν_3 frequencies (HF and MP2) of CH_3^+–Ar_n plotted as a function of the cluster size n [54]. For comparison, the corresponding frequencies of isolated CH_3^+ and CH_3 are indicated by arrows. Whereas p-bound ligands ($n=1, 2$) cause significant blue shifts, further ligands (probably H bonded for $n>2$) induce only minor red shifts. A possible structure of CH_3^+–Ar_3 is shown as well [120].

and comparison with the *ab initio* calculations. On the other hand, the second geometry is supported by the low barrier calculated for internal rotation of the Ar along the solvation ring ($\sim 17\,cm^{-1}$) [120]. As this barrier is of the order of the A rotational constant of CH_3^+–Ar_2 (~ 4–$5\,cm^{-1}$), the rotation may be nearly free. In this case, the maxima in the CH_3^+–Ar_3 spectrum would arise from $\Delta k_{int} = \pm 1$ transitions between different internal rotor states. Apparently, this internal motion is more and more quenched as further Ar atoms are added to the solvation shell because the $n \geq 4$ spectra lack such an internal rotation structure. Moreover, it is not clear whether the inversion tunnelling present in the trimer is quenched by further solvation. Intermolecular bonds to off-axial Ar ligands probably increase both the effective reduced mass and the inversion barrier leading to significantly smaller and thus unresolved tunnelling splittings. In general, knowledge of the $n \geq 4$ geometries is mainly based on the calculations described in section 5.1.1.

Two experimental sources provide access to incremental binding energies or enthalpies for the Ar ligands in CH_3^+–Ar_n. The first measurement determines bond enthalpies ($-\Delta H^0(n)$) derived from the Van't Hoff analysis of the following cluster aggregation equilibria observed in a high-pressure mass spectrometer [102]:

$$CH_3^+ - Ar_{n-1} + Ar \leftrightarrow CH_3^+ - Ar_n. \tag{5}$$

The second approach estimates $D_0(n)$ on the basis of the photofragmentation branching ratios, assuming a simple statistical model for ligand evaporation and similar binding energies for ligands in the same solvation subshell [54]. Photoexcitation of CH_3^+–Ar_n can cleave several intermolecular bonds (equation (2)), the number of which depends sensitively on the balance between the absorbed photon energy and the energy required for evaporation of the most weakly bound

ligands. The range of observed fragment channels (m) for a given cluster size (n) is rather small (see figure 8 for $n=5$), allowing the reliable estimation of the binding energies of the $n-m$ evaporated ligands. As can be seen from table 13, the values derived from both experimental methods agree well with one another and also with the recently calculated numbers [120]. They strongly support the cluster growth scenario discussed in section 5.1.1.

The measured ν_3 band origins of CH_3^+–Ar_n vary in a very systematic fashion (figure 24) and corroborate both the predicted structure of the first solvation shell and the size-dependent changes in the bonding mechanism [54]. Complexation of CH_3^+ with the first p-bound Ar atom increases ν_3 by a substantial amount from 3108 to $3145 \pm 30\,cm^{-1}$ as a result of large charge transfer and strong monomer deformation. The second Ar ligand causes only a small blue shift due to the much weaker p bond. Further ligands cause minor and constant incremental red shifts in the ν_3 frequency. Small red shifts are expected for Ar ligands in a solvation ring around the Ar–CH_3^+–Ar core because of weak hydrogen bonding to the CH_3^+ protons. This view is supported by the frequency calculations for side- and H-bound CH_3^+–Ar (table 4). Moreover, the rather similar incremental shifts for $n=3$–8 indicate that these ligands occupy roughly equivalent positions in the solvation shell, as predicted by the similar dissociation energies of ligands in the solvation ring(s). In general, the ν_3 (and also all other available C–H stretch) frequencies of all CH_3^+–Ar_n clusters investigated are much closer to that of neutral CH_3 than to that of CH_3^+, confirming the substantial electron transfer from the Ar_n solvation shell to the $2p_z$ orbital of CH_3^+ (mainly from the first ligand, figure 24). Unfortunately, Ar matrix isolation data are not available for CH_3^+ [210, 242], making it impossible at the present stage to compare the properties of the CH_3^+–Ar_n clusters with those of the bulk limit ($n \rightarrow \infty$).

5.4. *Microsolvation of small ions in an inert environment*

The characterization of $A^{\pm q}$–L_n clusters as a function of cluster size allows one to monitor the microsolvation process of an $A^{\pm q}$ ion by neutral solvent molecules in a stepwise fashion, with the final goal of relating microscopic molecular properties ($n=0$) to macroscopic attributes of the bulk limit ($n \rightarrow \infty$). Hence, A^+–Ar_n clusters are ideal model systems to investigate the microsolvation process of an A^+ monocation in a non-polar hydrophobic environment [243]. As the dispersion interaction between the spherical and structureless Rg atoms is isotropic, neutral Rg_n clusters prefer the formation of icosahedral structures in order to allow for closed packing [241, 244]. Fundamental properties of the solvation of a small cation (A^+) in argon (such as the structure of the primary solvation shell and the sequence of shell filling) depend sensitively on the size, shape and charge distribution of the central A^+ ion, which determine to a large degree the A^+–Ar interaction potential. In nearly all cases, the A^+–Ar interaction is much stronger than the Ar–Ar attraction ($\sim 100\,cm^{-1}$ [240]). Consequently, the most stable A^+–Ar_n clusters have structures with interior ion solvation, that is the central A^+ ion is localized inside the Ar_n cluster rather than on its surface. For small atomic and molecular A^+ cations with a nearly isotropic A^+–Ar interaction potential, the solvation shell is closed for $n=12$. Magic numbers observed in a variety of mass spectra of A^+–Ar_n clusters [245, 246] as well as photoelectron spectra of O^-–Ar_n [247] confirm this view. In addition, systematic frequency shifts observed in the IR spectra of AH^+–Ar_n complexes with linear AH^+ ions ($A = N_2$ and CO) suggest that the first solvation shell is also filled at

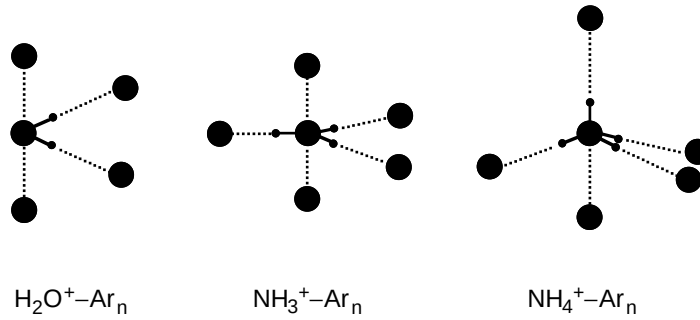

Figure 25. Structures calculated for H_2O^+–Ar_n ($n \leq 4$) [139], NH_3^+–Ar_n ($n \leq 5$) [121] and NH_4^+–Ar_n ($n \leq 5$) [147]. In these AH_k^+–Ar_n clusters, the first k Ar ligands form equivalent proton bonds, whereas further ligands ($n > k$) are attached to less favourable binding sites.

$n = 12$ and composed of two staggered equatorial five-membered rings around a linear Ar–AH^+–Ar trimer core [126, 128, 248]. In the latter examples, the closed-shell core ions have a size similar to that of Ar, so that the $n = 12$ clusters are only slightly distorted icosahedrons with a nearly 'spherical' impurity in the centre. The sequence of shell filling is slightly different in $SiOH^+$–Ar_n owing to subtle differences in the charge distributions and molecular shapes of these isovalent AH^+ ions [128, 132].

The cluster growth in AH_k^+–Ar_n systems, where the central AH_k^+ ion has several equivalent protons ($k \geq 2$), differs qualitatively from that in AH^+–Ar_n and Ar_n^+. The AH_k^+ ions possess usually several distinct attractive centres for ligands created by the k protons and/or electrophilic p orbitals. For example, CH_3^+ offers two p-bound and three H-bound sites. Consequently, the PESs of AH_k^+–Ar are of lower symmetry and usually more anisotropic than the PESs of AH^+–Ar dimers with linear AH^+. The intermolecular bonds in AH_k^+–Ar_n are often more directional and the AH_k^+ ions are far from being a spherical impurity within the icosahedral Ar_n solvent cluster. In general, in AH_k^+–Ar_n clusters whose dimer potentials have pronounced H-bound global minima, the first k Ar ligands form equivalent H bonds, whereas further ligands ($n > k$) are attached to less favourable binding sites (figure 25). Examples include H_2O^+–Ar_n [139, 140], H_3^+–Ar_n [249, 250], NH_3^+–Ar_n [121, 122] and NH_4^+–Ar_n [147]. For example, in the NH_3^+–Ar_n clusters the first three ligands are H bonded and the next two ligands form weaker p bonds. The CH_3^+–Ar_n clusters do not belong to this class, because the dimer PES features pronounced p-bound global minima and only shallow H-bound local minima [54], which changes the sequence of shell filling drastically compared with the related H_3^+–Ar_n or NH_3^+–Ar_n clusters. A common trend in all AH_k^+–Ar_n clusters is the decrease in the average binding energy of equivalent Ar ligands as the size of the cluster increases (except for some minor stabilizing effects observed for shell closing) [121, 122, 126, 128, 132, 139, 140, 147]. While p bonding usually increases the strengths of the intramolecular A–H bonds, H bonding causes the opposite effect. In general, the effects on sequential complexation at equivalent binding sites are non-cooperative and appear to become weaker as the cluster size increases. The latter effects are not only observed for Ar solvation of small polyatomic molecules but also for Ar and N_2 complexes of aromatic ions, such as the phenol [179], aniline [233, 251] or cyclopropenyl [154] cations. No Ar matrix isolation data exist for the AH^+ ions investigated by Ar microcluster

spectroscopy (discussed in this review) [210, 242], preventing a comparison of the properties of AH_k^+–Ar_n clusters with those of the bulk limit ($n \rightarrow \infty$).

6. Outlook

This review summarizes the results obtained by the recent application of high-resolution IR spectroscopy, mass spectrometry and sophisticated quantum chemical tools to CH_3^+–Rg_n clusters (Rg = He, Ne, Ar). This concerted effort provides very detailed information on a broad range of physical and chemical properties of these carbocation–ligand complexes. Several logical extensions of these investigations are apparent. For example, the characterization of CH_3^+–Rg_n clusters with larger Rg atoms (Rg = Kr and Xe) will reveal the larger intermolecular interaction and electron transfer from the Rg_n solvent cluster to the $2p_z$ orbital of CH_3^+. In addition, the inversion tunnelling motion of the Rg–CH_3^+–Rg trimers, describing the cationic S_N2 mechanism, could be probed more precisely by MW studies, because these yield direct information on the tunnelling splitting and inversion barrier in the ground vibrational state. Such MW studies appear to be feasible for these strongly bound ionic complexes, as has been shown recently by Endo and co-workers for related cation dimers [215, 216, 219]. The large interaction energy enables the production of high number densities required for the MW studies and the search for MW transitions may be guided by the rotational constants obtained from the IR data (as has been demonstrated for HCO^+–Ar [126, 216]). Further interesting targets for improving our knowledge on symmetric and asymmetric S_N2 reactions are complexes of the form L_a–CH_3^+–L_b involving molecular ligands ($L_a = L_b$ or $L_a \neq L_b$) or L–$CH_{3-x}Y_x^+$–L complexes where the protons of the methyl cation are (partly) substituted by deuterons or other functional groups. In addition, the CH_3^+–Rg_n studies can be extended to complexes of related carbocations, such as CH_2^+ or CH_4^+. Preliminary IR spectra for complexes of $C_2H_2^+$ [252] and $C_6H_5^+$ [187] have already been recorded. On the theoretical side, the CH_3^+–Rg disk-and-ball dimers are interesting targets for full 9D rovibrational calculations, because the inclusion of the internal monomer coordinates is crucial for the determination of PESs of spectroscopic accuracy. Similar full-dimensional calculations have recently been carried out for neutral dimers as large as $(H_2O)_2$ (twelve-dimensional) [253].

Significantly, the described studies of the CH_3^+–Rg and CH_3^+–Rg_2 trimers offer spectroscopic details of the potential involved in the cationic S_N2 reaction mechanism. In similar studies, protonated aromatic molecules (such as protonated benzene, phenol or fluorobenzene) have recently been characterized for the first time by spectroscopic tools under controlled solvation conditions [180, 187, 191, 254, 255]. These species are intermediates of electrophilic aromatic substitution reactions, the probably most common reaction mechanism of aromatic molecules. Corresponding studies on fundamental anion solvation complexes have recently been reviewed by Wild *et al.* [165, 256]. In addition, (transition) metal cation complexes relevant for catalytic processes have become a new and exciting target for IR spectroscopic studies by Duncan and co-workers [257–260]. The final goal of all these studies is to improve our understanding of chemical reaction mechanisms and their dependence on stepwise solvation with spectroscopic accuracy. Finally, the spectroscopic investigation of larger systems with biological relevance appears to be a promising tool to understand fundamental biophysical processes, such as molecular recognition, at the molecular level [261].

Acknowledgements

This work is part of the project DO 729/2-1 funded by the Deutsche Forschungsgemeinschaft (DFG). The author is at present supported by the DFG via a Heisenberg Fellowship (DO 729/1-1). The studies in Basel were part of projects No. 20-491104.96, 20-055285.98 and 20-63459.00 of the Swiss National Science Foundation. Some calculations were carried out at Centro Svizzero di Calcolo Scientifico in Manno, Switzerland. The author would like to thank the former PhD students R. V. Olkhov and S. A. Nizkorodov for their invaluable contributions to the spectroscopic part of this work and J. P. Maier for his generous support and ongoing interest in these studies. The rovibrational calculations of CH_3^+–Rg were analysed in a fruitful collaboration with D. Luckhaus.

References

[1] Bieske, E. J., and Dopfer, O., 2000, *Chem. Rev.*, **100**, 3963, and references therein.
[2] Stryer, L., 1996, *Biochemistry* (New York: Freeman).
[3] Jeffrey, G. A., and Saenger, W., 1991, *Hydrogen Bonding in Biological Systems* (Heidelberg: Springer).
[4] Hobza, P., and Zahradnik, R., 1988, *Intermolecular Complexes*: *The Role of van der Waals Systems in Physical Chemistry and in the Biodisciplines* (Amsterdam: Elsevier).
[5] Ohtaki, H., and Radnai, T., 1993, *Chem. Rev.*, **93**, 1157.
[6] Dedonder-Lardeux, C., Gregoire, G., Jouvet, C., Martrenchard, S., and Solgadi, D., 2000, *Chem. Rev.*, **100**, 4023.
[7] Hurley, S. M., Dermota, T. E., Hydutsky, D. P., and Castleman, A. W., Jr, 2002, *Science*, **298**, 202.
[8] Marcus, Y., 1985, *Ion Solvation* (New York: Wiley).
[9] March, J., 1992, *Advanced Organic Chemistry*: *Reactions*, *Mechanisms*, *and Structure* (New York: Wiley).
[10] Carey, F. A., and Sundberg, R. J., 1995, *Advanced Organic Chemistry* (New York: Plenum).
[11] Beauchamp, J. L., 1975, *Interactions Between Ions and Molecules*, edited by P. Ausloos (New York: Plenum).
[12] Brutschy, B., 1992, *Chem. Rev.*, **92**, 1567.
[13] Castleman, A. W., Jr, 1998, *Advances in Gas-Phase Ion Chemistry*, Vol. 3, edited by N. G. Adams and L. M. Babcock (Greenwich: JAI), p. 185.
[14] Ferguson, E. E., and Arnold, F., 1981, *Acc. Chem. Res.*, **14**, 327.
[15] Castleman, A. W., and Keesee, R. G., 1986, *Chem. Rev.*, **86**, 589.
[16] Keesee, R. G., and Castleman, A. W., Jr, 1986, *J. Phys. Chem. Ref. Data*, **15**, 1011.
[17] Kebarle, P., 2000, *Int. J. Mass Spectrom.*, **200**, 313.
[18] Ervin, K. M., 2001, *Chem. Rev.*, **101**, 391.
[19] Armentrout, P. B., and Baer, T., 1996, *J. Phys. Chem.*, **100**, 12866.
[20] Lifshitz, C., 1993, *Cluster Ions*, edited by C.-Y. Ng, T. Baer and I. Powis (New York: Wiley), p. 121.
[21] Three recent issues of *Chemical Reviews* are devoted to clusters and complexes: 1988, *Chem. Rev.*, **88**; 1994, *Chem. Rev.*, **94**; 2000, *Chem. Rev.*, **100**.
[22] Olkhov, R. V., Nizkorodov, S. A., and Dopfer, O., 1997, *J. Chem. Phys.*, **107**, 8229.
[23] Lakin, N. M., Olkhov, R. V., and Dopfer, O., 2001. *Faraday Discussion*, **118**, 455.
[24] Stone, A. J., 1996, *The Theory of Intermolecular Forces* (Oxford: Clarendon Press).
[25] Olah, G. A., and Schleyer, P. R., 1968. *Carbonium Ions*, Vol. I (New York: Wiley).
[26] Olah, G. A., and Schleyer, P. R., 1970, *Carbonium Ions*, Vol. II (New York: Wiley).
[27] Olah, G. A., and Schleyer, P. R., 1972, *Carbonium Ions*, Vol. III (New York: Wiley).
[28] Olah, G. A., and Schleyer, P. R., 1973, *Carbonium Ions*, Vol. IV (New York: Wiley).
[29] Olah, G. A., and Schleyer, P. R., 1976, *Carbonium Ions*, Vol. V (New York: Wiley).
[30] Olah, G. A., 1973, *Angew Chem., Int. Edn. Engl.*, **12**, 173.
[31] Richard, J. P., Amyes, T. L., and Toteva, M. M., 2001, *Acc. Chem. Res.*, **34**, 981.
[32] Fokin, A. A., and Schreiner, P. R., 2002, *Chem. Rev.*, **102**, 1551.

[33] Laube, T., 1998, *Chem. Rev.*, **98**, 1277.
[34] Hognes, T. R., and Kvalnes, H. M., 1928, *Phys. Rev.*, **32**, 942.
[35] Linstrom, P. J., and Mallard, W. G., 2001, *NIST Chemistry WebBook* (Gaithersburg MD: NIST Standards and Technology) (http://Webbook.nist.gov).
[36] Olah, G. A., 1995, *Angew. Chem., Int. Ed.*, **34**, 1393.
[37] Ford, G. P., and Scribner, J. D., 1983, *J. Am. Chem. Soc.*, **105**, 349.
[38] Bohme, D. K., 1979, *Kinetics of Ion-Molecule Reactions*, edited by P. Ausloos (New York: Plenum), p. 323.
[39] Goodings, J. M., Bohme, D. K., and Ng, C.-W., 1979, *Combust. Flame*, **36**, 27.
[40] Barker, J. R., 1995, *Progress and Problems in Atmospheric Chemistry* (London: World Scientific).
[41] Baulch, D. L., Cox, R. A., Crutzen, P. J., Hampson, R. F., Jr, Kerr, J. A., Troe, J., and Watson, R. T., 1982, *J. Phys. Chem. Ref. Data*, **11**, 327.
[42] Narcasi, R. S., 1975, *Interactions between Ions and Molecules*, edited by P. Ausloos (New York: Plenum), p. 635.
[43] Keller, C. N., Anicich, V. G., and Cravens, T. E., 1998, *Planet. Space Sci.*, **46**, 1157.
[44] Herbst, E., and Klemperer, W., 1973, *Astrophys. J.*, **185**, 505.
[45] Huntress, W. T., 1977, *Astrophys. J. Suppl.*, **33**, 495.
[46] Smith, D., 1992, *Chem. Rev.*, **92**, 1473.
[47] Smith, I. W. M., and Rowe, B. R., 2000, *Acc. Chem. Res.*, **33**, 261.
[48] Herbst, E., 2001, *Chem. Soc. Rev.*, **30**, 168.
[49] Hasegawa, T., Volk, K., and Kwok, S., 2000, *Astrophys. J.*, **532**, 994.
[50] Kaiser, R. I., 2002, *Chem. Rev.*, **102**, 1309.
[51] Anicich, V. G., 1993, *J. Chem. Phys. Ref. Data*, **22**, 1469.
[52] Crofton, M. W., Jagod, M.-F., Rehfuss, B. D., Kreiner, W. A., and Oka, T., 1988, *J. Chem. Phys.*, **88**, 666.
[53] Straub, H. C., Lin, D., Lindsay, B. G., Smith, A., and Stebbings, R. F., 1997, *J. Chem. Phys.*, **106**, 4430.
[54] Olkhov, R. V., Nizkorodov, S. A., and Dopfer, O., 1998, *J. Chem. Phys.*, **108**, 10046.
[55] Olkhov, R. V., Nizkorodov, S. A., and Dopfer, O., 1999, *J. Chem. Phys.*, **110**, 9527.
[56] Dopfer, O., Olkhov, R. V., and Maier, J. P., 2000, *J. Chem. Phys.*, **112**, 2176.
[57] Koenig, T., Balle, T., and Snell, W., 1975, *J. Am. Chem. Soc.*, **97**, 662.
[58] Dyke, J., Jonathan, N., Lee, E., and Morris, A., 1976, *J. Chem. Soc., Faraday Trans.* 2, **72**, 1385.
[59] Blush, J. A., Chen, P., Wiedman, R. T., and White, M. G., 1993, *J. Chem. Phys.*, **98**, 3557.
[60] Dickinson, H., Chelmick, T., and Softley, T. P., 2001, *Chem. Phys. Lett.*, **338**, 37.
[61] Crofton, M. W., Kreiner, W. A., Jagod, M.-F. Rehfuss, B. D., and Oka, T., 1985, *J. Chem. Phys.*, **83**, 3702.
[62] Rösslein, M., Jagod, M. F., Gabrys, C. M., and Oka, T., 1991, *Astrophys. J.*, **382**, L51.
[63] Jagod, M. F., Rosslein, M., Gabrys, C. M., and Oka, T., 1992, *J. Mol. Spectrosc.*, **1153**, 666.
[64] Jagod, M. F., Gabrys, C. M., Rosslein, M., Uy, D., and Oka, T., 1994, *Can. J. Phys.*, **72**, 1192.
[65] Liu, X., Gross, R. L., and Suits, A. G., 2001, *Science*, **294**, 2527.
[66] Ahmed, M., Peterka, D. S., Regan, P., Liu, X., and Suits, A. G., 2001, *Chem. Phys. Lett.*, **339**, 203.
[67] DeFrees, D. J., and McLean, A. D., 1985, *J. Chem. Phys.*, **82**, 333.
[68] Botschwina, P., Flesch, J., and Meyer, W., 1983, *Chem. Phys. Lett.*, **74**, 321.
[69] Botschwina, P., 1989, *Ion and Cluster Ion Spectroscopy and Structure*, edited by J. P. Maier (Amsterdam: Elsevier), p. 59.
[70] Kraemer, W. P., and Spirko, V., 1991, *J. Mol. Spectrosc.*, **149**, 235.
[71] Spirko, V., and Kraemer, W. P., 1992, *J. Mol. Spectrosc.*, **153**, 285.
[72] Pracna, P., Spirko, V., and Kraemer, W. P., 1993, *J. Mol. Spectrosc.*, **158**, 433.
[73] Yu, H. G., and Sears, T. J., 2002, *J. Chem. Phys.*, **117**, 666.

[74] Kelly, P. B., and Westre, S. G., 1988, *Chem. Phys. Lett.*, **151**, 253.
[75] Zahedi, M., Harrison, J. A., and Nibler, J. W., 1994, *J. Chem. Phys.*, **100**, 4043.
[76] Yamada, C., Hirota, E., and Kawaguchi, K., 1981, *J. Chem. Phys.*, **75**, 5256.
[77] Davis, S., Anderson, D. T., Duxbury, G., and Nesbitt, D. J., 1997, *J. Chem. Phys.*, **107**, 5661.
[78] Snelson, A., 1970, *J. Phys. Chem.*, **74**, 537.
[79] Westre, S. G., Liu, X., Getty, J. D., and Kelly, P. B., 1991, *J. Chem. Phys.*, **95**, 8793.
[80] Triggs, N. E., Zahedi, M., Nibler, J. W., DeBarber, P., and Valentini, J. J., 1992, *J. Chem. Phys.*, **96**, 1822.
[81] Holtz, D., Beauchamp, J. L., and Woodgate, S. D., 1970, *J. Am. Chem. Soc.*, **92**, 7484.
[82] Smith, D., and Adams, N. G., 1978, *Chem. Phys. Lett.*, **54**, 535.
[83] Adams, N. G., and Smith, D., 1981, *Chem. Phys. Lett.*, **79**, 563.
[84] Kemper, P. R., Bass, L. M., and Bowers, M. T., 1985, *J. Phys. Chem.*, **89**, 1105.
[85] Sonnenfroh, D. M., and Farrar, J. M., 1986, *J. Chem. Phys.*, **85**, 7167.
[86] Jarrold, M. F., Kirchner, N. J., Liu, S., and Bowers, M. T., 1986, *J. Phys. Chem.*, **90**, 78.
[87] Phillips, L. F., 1990, *J. Phys. Chem.*, **94**, 5265.
[88] Bucci, R., Grandinetti, F., Filippi, A., Laguzzi, G., Occhiucci, G., and Speranza, M., 1991, *J. Am. Chem. Soc.*, **113**, 4550.
[89] Uggerud, E., 1994, *J. Am. Chem. Soc.*, **116**, 6873.
[90] Mark, S., Schellhammer, C., Niedner-Schatteburg, G., and Gerlich, D., 1995, *J. Phys. Chem.*, **99**, 15587.
[91] Hiraoka, K., Katsuragawa, J., Sugiyama, T., Minamitsu, A., Yamabe, S., and Kouno, H., 1997, *Chem. Phys. Lett.*, **271**, 302.
[92] Diaz, N., Suarez, D., and Sordo, T. L., 1998, *J. Phys. Chem. A*, **102**, 9918.
[93] Miklis, P. C., Ditschfield, R., and Spencer, T. A., 1998, *J. Am. Chem. Soc.*, **120**, 10482.
[94] Scott, G., B. I., Fairley, D. A., Freeman, C. G., McEvan, M. J., and Anicich, V. G., 1999, *J. Phys. Chem.* A, **103**, 1073.
[95] Scott, G. B. I., Milligan, D. B., Fairley, D. A., Freeman, C. G., and McEvan, M. J., 2000, *J. Chem. Phys.*, **112**, 4959.
[96] Field, F. H., Head, H. N., and Franklin, J. L., 1962, *J. Am. Chem. Soc.*, **84**, 1118.
[97] Field, F. H., and Franklin, J. L., 1961, *J. Am. Chem. Soc.*, **83**, 4509.
[98] Carlson, T. A., and White, R. M., 1963, *J. Chem. Phys.*, **39**, 1748.
[99] Hovey, J. K., and McMahon, T. B., 1987, *J. Phys. Chem.*, **91**, 4560.
[100] Hovey, J. K., and McMahon, T. B., 1986, *J. Am. Chem. Soc.*, **108**, 528.
[101] McMahon, T. B., Heinis, T., Nicol, G., Hovey, J. K., and Kebarle, P., 1988, *J. Am. Chem. Soc.*, **110**, 7591.
[102] Hiraoka, K., Kudaka, I., and Yamabe, S., 1991, *Chem. Phys. Lett.*, **178**, 103.
[103] Heck, A. J. R., Koning, L. J. D., and Nibbering, N. M. M., 1992, *J. Phys. Chem.*, **96**, 8870.
[104] Cunje, A., Rodriquez, C. F., Bohme, D. K., and Hopkinson, A. C., 1998, *J. Phys. Chem. A*, **102**, 478.
[105] Cunje, A., Rodriquez, C. F., Bohme, D. K., and Hopkinson, A. C., 1998, *Can. J. Chem.*, **76**, 1138.
[106] Hunter, E. P. L., and Lias, S. G., 1998, *J. Phys. Chem. Ref. Data*, **27**, 413.
[107] Olmstead, W. N., and Brauman, J. I., 1977, *J. Am. Chem. Soc.*, **99**, 4219.
[108] DePuy, C. H., 2002, *J. Org. Chem.*, **67**, 2393.
[109] Shaik, S. S., Schlegel, H. B., and Wolfe, S., 1992, *Theoretical Aspects of Physical Organic Chemistry*: *The S_N2 Mechanism* (New York: Wiley).
[110] Hase, W. L., 1994, *Science*, **266**, 998.
[111] Hase, W. L., Wang, H., and Peslherbe, G. H., 1998, *Advances in Gas-Phase Ion Chemistry*, Vol. 3, edited by N. G. Adams and L. M. Babcock (Greenwich: JAI), p. 125.
[112] Angel, L. A., Garcia, S. P., and Ervin, K. M., 2002, *J. Am. Chem. Soc.*, **124**, 336.
[113] Tachikawa, H., 2000, *J. Phys. Chem.* A, **104**, 497.

[114] Schmatz, S., Botschwina, P., Hausschildt, J., and Schinke, R., 2001, *J. Chem. Phys.*, **114**, 5233.
[115] Ayotte, P., Kim, J., Kelley, J. A., Nielsen, S. B., and Johnson, M. A., 1999, *J. Am. Chem. Soc.*, **121**, 6950.
[116] Mann, D. J., and Hase, W. L., 1998, *J. Phys. Chem.* A, **1102**, 6208.
[117] Chandrasekhar, J., Smith, S. F., and Jorgensen, W. L., 1985, *J. Am. Chem. Soc.*, **107**, 154.
[118] Dopfer, O., and Luckhaus, D., 2002, *J. Chem. Phys.*, **116**, 1012.
[119] Dopfer, O., 2001, *Faraday Discuss.*, **118**, 171.
[120] Gora, R. W., Roszak, S., and Leszczynski, J., 2001, *J. Chem. Phys.*, **115**, 771.
[121] Dopfer, O., 2002, *Chem. Phys.*, **283**, 63.
[122] Dopfer, O., Solca, N., Olkhov, R. V., and Maier, J. P., 2002, *Chem. Phys.*, **283**, 85.
[123] Dopfer, O., *et al.*, unpublished results.
[124] Nizkorodov, S. A., Maier, J. P., and Bieske, E. J., 1995, *J. Chem. Phys.*, **103**, 1297.
[125] Nizkorodov, S. A., Dopfer, O., Meuwly, M., Maier, J. P., and Bieske, E. J., 1996, *J. Chem. Phys.*, **105**, 1770.
[126] Nizkorodov, S. A., Dopfer, O., Ruchti, T., Meuwly, M., Maier, J. P., and Bieske, E. J., 1995, *J. Phys., Chem.*, **99**, 17118.
[127] Bieske, E. J., Nizkorodov, S. A., Bennett, F. R., and Maier, J. P., 1995, *J. Chem. Phys.*, **102**, 5152.
[128] Dopfer, O., Olkhov, R. V., and Maier, J. P., 1999, *J. Phys. Chem. A*, **103**, 2982.
[129] Meuwly, M., Nizkorodov, S. A., Maier, J. P., and Bieske, E. J., 1996, *J. Chem. Phys.*, **104**, 3876.
[130] Nizkorodov, S. A., Spinelli, Y., Bieske, E. J., Maier, J. P., and Dopfer, O., 1997, *Chem. Phys. Lett.*, **265**, 303.
[131] Nizkorodov, S. A., Meuwly, M., Maier, J. P., Dopfer, O., and Bieske, E. J., 1998, *J. Chem. Phys.*, **108**, 8964.
[132] Olkhov, R. V., Nizkorodov, S. A., and Dopfer, O., 1998, *Chem. Phys.*, **239**, 393.
[133] Olkhov, R. V., and Dopfer, O., 1999, *Chem. Phys. Lett.*, **314**, 215.
[134] Dopfer, O., Roth, D., and Maier, J. P., 2000, *J. Chem. Phys.*, **113**, 120.
[135] Dopfer, O., Olkhov, R. V., Roth, D., and Maier, J. P., 1998, *Chem. Phys. Lett.*, **296**, 585.
[136] Nizkorodov, S. A., Roth, D., Olkhov, R. V., Maier, J. P., and Dopfer, O., 1997, *Chem. Phys. Lett.*, **278**, 26.
[137] Roth, D., Nizkorodov, S. A., Maier, J. P., and Dopfer, O., 1998, *J. Chem. Phys.*, **109**, 3841.
[138] Meuwly, M., Maier, J. P., and Rosmus, P., 1998, *J. Chem. Phys.*, **109**, 3850.
[139] Dopfer, O., 2000, *J. Phys. Chem.* A, **104**, 11693.
[140] Dopfer, O., Roth, D., and Maier, J. P., 2000, *J. Phys. Chem. A*, **104**, 11 702.
[141] Dopfer, O., Roth, D., and Maier, J. P., 2001, *J. Chem. Phys.*, **114**, 7081.
[142] Roth, D., Dopfer, O., and Maier, J. P., 2001, *Phys. Chem. Chem. Phys.*, **3**, 2400.
[143] Dopfer, O., Nizkorodov, S. A., Olkhov, R. V., Maier, J. P., and Harada, K., 1998, *J. Phys. Chem. A*, **102**, 10017.
[144] Dopfer, O., Roth, D., and Maier, J. P., 1999, *Chem. Phys. Lett.*, **310**, 201.
[145] Roth, D., Dopfer, O., and Maier, J. P., 2000, *Phys. Chem. Chem. Phys.*, **2**, 5013.
[146] Dopfer, O., Nizkorodov, S. A., Meuwly, M., Bieske, E. J., and Maier, J. P., 1996, *Chem. Phys. Lett.*, **260**, 545.
[147] Dopfer, O., Nizkorodov, S. A., Meuwly, M., Bieske, E. J., and Maier, J. P., 1997, *Int. J. Mass Spectrom. Ion Processes*, **167–168**, 637.
[148] Bieske, E. J., Nizkorodov, S. A., Dopfer, O., Maier, J. P., Stickland, R. J., Cotterell, B. J., and Howard, B. J., 1996, *Chem. Phys. Lett.*, **250**, 266.
[149] Lakin, N. M., Dopfer, O., Howard, B. J., and Maier, J. P., 2000, *Mol. Phys.*, **98**, 81.
[150] Lakin, N. M., Dopfer, O., Meuwly, M., Howard, B. J., and Maier, J. P., 2000, *Mol. Phys.*, **98**, 63.
[151] Dopfer, O., Roth, D., Olkhov, R. V., and Maier, J. P., 1999, *J. Chem. Phys.*, **110**, 11911.
[152] Roth, D., and Dopfer, O., 2002, *Phys. Chem. Chem. Phys.*, **4**, 4855.

[153] Dopfer, O., Roth, D., and Maier, J. P., 2002, *J. Am. Chem. Soc.*, **124**, 494.
[154] Dopfer, O., Roth, D., and Maier, J. P., 2002, *Int. J. Mass. Spectrom.*, **218**, 281.
[155] Crofton, M. W., Price, J. M., and Lee, Y. T., 1994, *Clusters of Atoms and Molecules II*, Vol. 56, edited by H. Haberland (Berlin: Springer), p. 44.
[156] Lisy, J. M., 1997, *Int. Rev. Phys. Chem.*, **16**, 267.
[157] Kleiber, P. D., and Chen, J., 1998, *Int. Rev. Phys. Chem.*, **17**, 1.
[158] Yeh, C. S., Pilgrim, J. S., Willey, K. F., Robbins, D. L., and Duncan, M. A., 1994, *Int. Rev. Phys. Chem.*, **13**, 231.
[159] Duncan, M. A., 1997, *Annu. Rev. Phys. Chem.*, **48**, 69.
[160] Duncan, M. A., 2000, *Int. J. Mass Spectrom.*, **200**, 545.
[161] Farrar, J. M., 1993, *Cluster Ions*, edited by C.-Y. Ng, T. Baer and I. Powis (New York: Wiley), p. 243.
[162] Ebata, T., Fujii, A., and Mikami, N., 1998, *Int. Rev. Phys. Chem.*, **17**, 331.
[163] Weber, J. M., Kelley, J. A., Nielsen, S. B., Ayotte, P., and Johnson, M. A., 2000, *Science*, **287**, 2461.
[164] Carrington, A., Shaw, A. M., and Taylor, S. M., 1995, *J. Chem. Soc., Faraday. Trans.*, **91**, 3725.
[165] Wild, D. A., and Bieske, E. J., 2003, *Int. Rev. Phys. Chem.*, **22**, 129.
[166] Inokuchi, Y., Ohashi, K., Honkawa, Y., Sekiya, H., and Nishi, N., 2002, *Chem. Phys. Lett.*, **359**, 283.
[167] Piest, H., von Helden, G., and Meijer, G., 1999, *J. Chem. Phys.*, **110**, 2010.
[168] Scoles, G., 1988, *Atomic and Molecular Beam Methods* (Oxford: Oxford University Press).
[169] Schinke, R., 1993, *Photodissociation Dynamics* (Cambridge: Cambridge University Press).
[170] Baer, T., and Hase, W. L., 1996, *Unimolecular Reaction Dynamics* (Oxford: Oxford University Press).
[171] Miller, R. E., 1990, *Acc. Chem. Res.*, **23**, 10.
[172] Berden, G., Peeters, R., and Meijer, G., 2000, *Int. Rev. Phys. Chem.*, **19**, 465.
[173] Okumura, M., Yeh, L. I., and Lee, Y. T., 1985, *J. Chem. Phys.*, **83**, 3705.
[174] Bogey, M., Bolvin, H., Demuynck, C., and Destombes, J. L., 1987, *Phys. Rev. Lett.*, **58**, 988.
[175] Bieske, E. J., 1995, *J. Chem. Soc., Faraday Trans.*, **91**, 1.
[176] Bieske, E. J., Soliva, A. S., Friedmann, A., and Maier, J. P., 1992, *J. Chem. Phys.*, **96**, 4035.
[177] Daly, N. R., 1960, *Rev. Sci. Instrum.*, **31**, 264.
[178] Guelachvili, G., and Rao, K. N., 1993, *Handbook of Infrared Standards* (London: Academic).
[179] Solcà, N., and Dopfer, O., 2001, *J. Phys. Chem. A*, **105**, 5637.
[180] Solcà, N., and Dopfer, O., 2003, *Chem. Eur. J.* (in press).
[181] Dopfer, O., Olkhov, R. V., and Maier, J. P., 1999, *J. Chem. Phys.*, **111**, 10754.
[182] Solcà, N., and Dopfer, O., 2002, *J. Phys. Chem.* A., **106**, 7261.
[183] Boys, S. F., and Bernardi, F., 1970, *Mol. Phys.*, **19**, 553.
[184] Duijneveldt, V., 1997, *Molecular Interactions*, edited by S. Scheiner (New York: Wiley), p. 81.
[185] Chalasinski, G., and Szczesniak, M. M., 1994, *Chem. Rev.*, **94**, 1.
[186] Solcà, N., and Dopfer, O., 2001, *Chem. Phys. Lett.*, **347**, 59.
[187] Solcà, N., and Dopfer, O., 2003, *J. Am. Chem. Soc.*, **125**, 1421.
[188] Herzberg, G., *Molecular Spectra and Molecular Structure. III. Electronic Spectra and Electronic Structure of Polyatomic Molecules* (Malabar, FL: Krieger).
[189] Spirko, V., 1997, private communication.
[190] Okumura, M., Yeh, L. I., Myers, J. D., and Lee, Y. T., 1990, *J. Phys. Chem.*, **94**, 3416.
[191] Solcà, N., and Dopfer, O., 2002, *Angew. Chem., Int. Ed.*, **41**, 3628.
[192] Millen, D. J., 1985, *Can. J. Chem.*, **63**, 1477.
[193] Hutson, J. M., 1992, *J. Chem. Phys.*, **96**, 6752.
[194] Drucker, S., Cooksy, A. L., and Klemperer, W., 1993, *J. Chem. Phys.*, **98**, 5158.

[195] Fiacco, D. L., Kirchner, B., Burns, W. A., and Leopold, K. R., 1998, *J. Mol. Spectrosc.*, **191**, 389.
[196] van der Avoird, A., Wormer, P. E. S., and Moszynski, R., 1994, *Chem. Rev.*, **94**, 1931.
[197] Wormer, P. E. S., and van der Avoird, A., 2000, *Chem. Rev.*, **100**, 4109.
[198] Brupbacher, T., Makarewicz, J., and Bauder, A., 1994, *J. Chem. Phys.*, **101**, 9736.
[199] Israelachvili, J., 1992, *Intermolecular and Surface Forces* (London: Academic).
[200] Gray, C. G., and Gubbins, K. E., 1984, *Theory of Molecular Fluids* (Oxford: Clarendon).
[201] Weast, R. C., 1976, *Handbook of Chemistry and Physics*, 57th edn (Cleveland OH: CRC Press).
[202] Gray, D. L., and Robiette, A. G., 1979, *Mol. Phys.*, **37**, 1901.
[203] Vaara, J., and Hiltunen, Y., 1997, *J. Chem. Phys.*, **107**, 1744.
[204] Hawkins, D. T., Falconer, W. E., and Bartlett, N., 1978, *Noble Gas Compounds* (London: Plenum).
[205] Reynard, L. M., Evans, C. J., and Gerry, M. C. L., 2001, *J. Mol. Spectrosc.*, **206**, 33.
[206] Khriachtchev, L., Pettersson, M., Runeberg, N., Lundell, J., and M. Räsänen, 2000, *Nature*, **406**, 875.
[207] Kötting, C., Sander, W., Breidung, J., Thiel, W., Senzlober, M., and Bürger, H., 1998, *J. Am. Chem. Soc.*, **120**, 219.
[208] Cunje, A., Baranov, V. I., Ling, Y., Hopkinson, A. C., and Bohme, D. K., 2001, *J. Phys. Chem.* A, **105**, 11073.
[209] White, E. T., Tang, J., and Oka, T., 1999, *Science*, **284**, 135.
[210] Jacox, M. E., 1998, *J. Phys. Chem. Ref. Data*, **27**, 115.
[211] Scuseria, G. E., 1993, *Nature*, **366**, 512.
[212] Marx, D., and Parrinello, M., 1999, *Science*, **284**, 59.
[213] Marx, D., and Parrinello, M., 1995, *Nature*, **375**, 216.
[214] Jacox, M. E., 2002, *Chem. Soc. Rev.*, **31**, 108.
[215] Seki, K., Sumiyoshi, Y., and Endo, Y., 2000, *Chem. Phys. Lett.*, **331**, 184.
[216] Ohshima, Y., Sumiyoshi, Y., and Endo, Y., 1997, *J. Chem. Phys.*, **106**, 2977.
[217] Linnartz, H., Speck, T., and Maier, J. P., 1998, *Chem. Phys. Lett.*, **288**, 504.
[218] Botschwina, P., Dutoi, T., Mladenovic, M., Oswald, R., Schmatz, S., and Stoll, H., 2001, *Faraday Discuss.*, **118**, 433.
[219] Seki, K., Sumiyoshi, Y., and Endo, Y., 2002, *J. Chem. Phys.*, **117**, 9750.
[220] Bailleux, S., Bogey, M., Bolvin, H., Civis, S., Cordonnier, M., Krupnov, A. F., Tretyakov, M. Y., Walters, A., and Coudert, L. H., 1998, *J. Mol. Spectrosc.*, **190**, 130.
[221] Oshima, Y., and Endo, Y., 1996, *Chem. Phys. Lett.*, **256**, 635.
[222] Simandiras, E. D., Gaw, J. F., and Handy, N. C., 1987, *Chem. Phys. Lett.*, **141**, 166.
[223] Hobza, P., Zahradnik, R., and Smith, D., 1993, *Chem. Phys. Lett.*, **208**, 497.
[224] Escribano, R., and Bunker, P. R., 1988, *Chem. Phys. Lett.*, **143**, 439.
[225] Boo, D. W., and Lee, Y. T., 1996, *Int. J. Mass. Spectrom. Ion Proc.*, **159**, 209.
[226] Leopold, K. R., 1996, *Advances in Molecular Structure Research*, Vol. 2, edited by M. Hargittai, and I. Hargittai (Greenwich: JAI Press), p. 103.
[227] Leopold, K. R., Canagaratna, M., and Phillips, J. A., 1998, *Acc. Chem. Res.*, **30**, 57.
[228] Heaven, M. C., 1992, *Annu. Rev. Phys. Chem.*, **42**, 283.
[229] Chalasinski, G., Klos, J., Cybulski, M., and Szczesniak, M., 1998, *Collect. Czech. Chem. Commun.*, **63**, 1473.
[230] Nielsen, S. B., Ayotte, P., Kelley, J. A., Weddle, G. H., and Johnson, M. A., 1999, *J. Chem. Phys.*, **111**, 10464.
[231] Yourshaw, I., Zhao, Y., and Neumark, D. M., 1996, *J. Chem. Phys.*, **105**, 351.
[232] Elrod, M. J., and Saykally, R. J., 1994, *Chem. Rev.*, **94**, 1975.
[233] Solcà, N., and Dopfer, O., 2002, *Eur. Phys. J. D*, **20**, 469.
[234] Herzberg, G., 1991, *Molecular Spectra and Molecular Structure. II. Infrared and Raman Spectra of Polyatomic Molecules* (Malabar, FL: Krieger).

[235] Bunker, P. R., and Jensen, P., 1998, *Molecular Symmetry and Spectroscopy* (Ottawa: NRC Research Press).
[236] Neusser, H. J., and Krause, H., 1994, *Chem. Rev.*, **94**, 1829.
[237] Hobza, P., Bludsky, O., Selzle, H. L., and Schlag, E. W., 1996, *Chem. Phys. Lett.*, **250**, 402.
[238] Bakker, J. M., Satink, R. G., von Helden, G., and Meijer, G., 2002, *Phys. Chem. Chem. Phys.*, **4**, 24.
[239] March, J., 1985, *Advanced Organic Chemistry*: *Reactions*, *Mechanisms*, *and Structure* (New York: Wiley).
[240] Hutson, J. M., 1990, *Annu. Rev. Phys. Chem.*, **41**, 123.
[241] Mackay, A. L., 1962, *Acta Crystallogr.*, **15**, 916.
[242] Jacox, M. E., 1994, *Vibrational and Electronic Energy Levels of Polyatomic Transient Molecules* (AIP, ACS and NIST).
[243] Bellert, D., and Breckenridge, W. H., 2002, *Chem. Rev.*, **102**, 1595.
[244] Hoare, M. R., 1979, *Adv. Chem. Phys.*, **40**, 49.
[245] Harris, I. A., Kidwell, R. S., and Northby, J. A., 1984, *Phys. Rev. Lett.*, **53**, 2390.
[246] Stace, A. J., 1985, *Chem. Phys. Lett.*, **113**, 355.
[247] Arnold, S. T., Hendricks, J. H., and Bowen, K. H., 1995, *J. Chem. Phys.*, **102**, 39.
[248] Sheng, Y., Gora, R. W., Roszak, S., Kaczorowska, M., and Leszczynski, J., 2002, *J. Phys. Chem. A*, **106**, 11162.
[249] Kaczorowska, M., Roszak, S., and Leszczynski, J., 2000, *J. Chem. Phys.*, **113**, 3615.
[250] Beyer, M., Savchenko, E. V., Niedner-Schatteburg, G., and Bondybey, V. E., 1999, *J. Chem. Phys.*, **110**, 11950.
[251] Nakanaga, T., and Ito, F., 2002, *Chem. Phys. Lett.*, **109**, 109.
[252] Dopfer, O., *et al.*, unpublished results.
[253] Leforestier, C., Gatti, F., Fellers, R. S., and Saykally, R. J., 2002, *J. Chem. Phys.*, **117**, 8710.
[254] Solcà, N., and Dopfer, O., 2001, *Chem. Phys. Lett.*, **342**, 191.
[255] Solcà, N., and Dopfer, O., 2003, *Angew. Chem. Int. Ed.*, **42**, 1537.
[256] Wild, D. A., Weiser, P. S., Bieske, E. J., and Zehnacker, A., 2001, *J. Chem. Phys.*, **115**, 824.
[257] Walters, R. S., Jaeger, T. D., and Duncan, M. A., 2002, *J. Phys. Chem. A*, **106**, 10482.
[258] Gregoire, G., Velasquez, J., and Duncan, M. A., 2001, *Chem. Phys. Lett.*, **349**, 451.
[259] Gregoire, G., and Duncan, M. A., 2002, *J. Chem. Phys.*, **117**, 2120.
[260] van Heijnsbergen, D., Jaeger, T. D., von Helden, G., Meijer, G., and Duncan, M. A., 2002, *Chem. Phys. Lett.*, **364**, 345.
[261] Weinkauf, R., Schermann, J. P., de Vries, M. S., and Kleinermanns, K., 2002, *Eur. Phys. J. D*, **20**, 309.